THE ROLE OF ATOMIC INTERFACES ON ELECTRONIC, MAGNETIC AND SWITCHING PROPERTIES OF OXIDE HETEROSTRUCTURES

CHANGJIAN LI

B. SCI. (Hons.) and B. ENG.(Hons.), NUS

A THESIS SUBMITTED

FOR THE DEGREE OF DOCTOR OF PHILOSOPHY IN SCIENCE

NUS GRADUATE SCHOOL OF INTEGRATIVE SCIENCE AND ENGINEERING

NATIONAL UNIVERSITY OF SINGAPORE

2015

DECLARATION

I hereby declare that the thesis is my original work and it has been written by me entirely.

I have duly acknowledged all the sources of information which have been used in this thesis.

This thesis has not been submitted for any degree in any university previously.

Changjian Li

25 November 2015

ACKNOWLEGEMENTS

PhD study has been one fulfilling and exciting journey for me. Starting with curiosity driven exploration, frustration after initial try-outs, anxiety of passing the qualifying exams, timely encouragement from supervisors and seniors, unmitigated excitement over first published paper, bravely taking up a new problem and finally a re-learning the entire process through thesis writing. I am so fortunate that there were so many helpful and interesting people accompanying me during my PhD study. Here I take this chance to express my greatest thanks to them.

Prof. T. Venkatesan, my supervisor, is on the top of the list. He is so knowledgeable in materials science and physics, enthusiastic in scientific research and an out of the box thinker. Each time we had a discussion, I learned some new approaches to a problem. He not only taught me on research subjects, but also advised me a lot on future career plans. I remembered that he helped me correct my manuscripts time after time, put his effort to polish each sentence and each word. He has really set a role model for a scientist and a teacher for me. Many thanks to him!

I would also thank Prof. Ding Jun and Prof Loh Kian Ping serving as my thesis advisory committee. Every semester I reported to them, they gave me prompt feedback which greatly improved my research work. I also would like to thank Prof. Ariando for his help on suggestions on research projects, experimental details and improvements on my manuscripts.

Prof. Michael Coey is another professor that I would like to express my special thanks. He was visiting professor in NUSNNI-Nanocore for the past two years. I worked closely with Michael for a couple of projects. He was so patient to help me propose new experimental designs, propose simple physical models and correct my manuscripts. I can see the pure curiosity and enthusiasm to physics from Prof Coey; just like a child curious to new toys. I learnt this attitude from him and will keep for following research work. I sincerely hope him being healthy and mentally sharp.

Then I would like to express my special thanks to my senior colleague: Dr. Lü, Weiming. We had numerous discussions on experimental details and experimental results. He was extremely patient to teach me every single detail that I did not understand. He was and will always be really like a "big brother" to me. He has joined Harbin Institute of Technology, China as a professor. I am sure more students will benefit from him and he will do a great job. I would also like to thank Drs. Renshaw Wang Xiao and Liu Zhiqi. We had a number of collaborations and published papers together. Collaboration with them greatly accelerated my research progress and I really learned a lot from them.

I also want to thank Prof. Chen, Jingsheng, Drs Huang Lisen, Li Tao, Qiu Xuepeng and Jian Linke for their assistance for some experiments. I also thank Drs. Huang Zhen, Zeng Shengwei, Zhao Yongliang, Surajit Saha, Tarapada Sarkar, Guo Rui, Anil Annadi, Mallikarjunarao Motapothula, Lily Mondal, Mr. Michal Marcin Dykas, Abhijeet Patra, Han Kun, Zhou Wenxiong, Wan Dongyang, Zhang Lingchao, Bao Nina and Sun Lin for their help in research and life I will always remember the gathering, lunch time chatting, which brought me so much fun and I really enjoyed such a pleasant working environment with all the people in NUSNNI-Nanocore.

I also would like to thank NGS for financial support for my Ph D. With NGS scholarship, I had so much freedom to study what I am interested most into. I also had so many chances to attending so many international conferences to share my research findings and to learn from research peers. I would certainly publicize NGS to my juniors which would like to pursue Ph D. studies. I hope more junior scientists would benefit from such an energetic and vibrant integrative graduate school.

Last but not least, I want to express my sincere thanks to my beloved my parents, sisters and my girlfriend, Yin Xuejiao, for their consistent support. My life is becoming so beautiful and promising thanks to so many beloved ones.

TABLE OF CONTENTS

ABSTRACT

Functional oxides with wide spectra of properties hold promising applications in future multifunctional devices. Thin film form of functional oxides is one of the most important building blocks for device fabrication. Interfaces between complex oxides give rise to a lot of interesting properties and hold promises for future applications. Hence, it is worthwhile to devote studies on novel oxide interfaces.

In this thesis, three materials systems: $LaAlO_3/SrTiO_3$, $LaMnO_3/SrTiO_3$ and $Pt/(La_{0.67}Sr_{0.33}MnO_3/La_{1-x}Sr_xMnO_3/)BaTiO_3//Nb:SrTiO_3$ were studied for electronic, magnetic and switching properties. In $LaAlO_3/SrTiO_3$, we firstly clarified the origin of conductive interface between two band insulators, then revealed the relative dominance of electron scattering mechanisms near the metal-insulator-transition regime and finally we determined a critical crystallinity (70% at temperature 515 ℃) for the formation of two dimensional electron gas at the interface. In $LaMnO_3/SrTiO_3$, we found polar discontinuity, unlike $LaAlO_3/SrTiO_3$, does not lead to a conductive interface but a magnetic phase transition. We conclusively demonstrated 6 uc of the critical thickness for the transition both in bulk and microscopic measurements and a theoretical model of the electronic reconstruction was also proposed. In the ferroelectric tunnel junction (FTJ of $Pt/(La_{0.67}Sr_{0.33}MnO_3/La_{1-x}Sr_xMnO_3/)BaTiO_3//Nb:SrTiO_3$) study, we showed that additional interfaces increase tunnel electroresistance (TER) of an FTJ at the expense of the resistance area product ($R_{on}A$) originating from band offset effects at the interfaces within an FTJ. To reach a compromise between TER and $R_{on}A$, we were the first to demonstrate a TER of 400% at room temperature for FTJ of $Pt/BaTiO_3/Nb:SrTiO_3$ with the $BaTiO_3$ layer of only 0.8 nm (2 uc). Summarizing all experimental results, electrostatic boundary conditions and band offsets at oxide

interfaces are extremely important parameters to be considered and utilized for building multifunctional devices.

LIST OF PUBLICATIONS

1. X. Renshaw Wang†, C. J. Li†, W. M. Lü, T. R. Paudel, D. P. Leusink, M. Hoek, Nicola Poccia, Arturas Vailionis, T. Venkatesan, J. M. D. Coey, E. Y. Tsymbal, Ariando and H.Hilgenkamp "Imaging and control of ferromagnetism in $LaMnO_3/SrTiO_3$ heterostructures**" Science**, 349, 716 (2015)
† Equal contribution.

2. Z. Q. Liu†, C. J. Li†, W. M. Lu, X. H. Huang, Z. Huang, S.W. Zeng, X. P. Qiu, L. S. Huang, A. Annadi, J. S. Chen, J. M. D. Coey, T. Venkatesan, and Ariando, "Origin of the Two-Dimensional Electron Gas at $LaAlO_3/SrTiO_3$ Interfaces: The Role of Oxygen Vacancies and Electronic Reconstruction" **Physical Review X**, 3, 021010 (2013).
† Equal contribution.

3. C. J. Li, L.S. Huang, T. Li, W. M. Lü, X. P. Qiu, Z. Huang, Z.Q. Liu, Z.S.W. Zeng, R. Guo, Y.L. Zhao, K.Y. Zeng, JMD. Coey, J. S. Chen, Ariando and T. Venkatesan "Ultrathin of $BaTiO_3$ based Ferroelectric Tunnel Junctions" **Nano Letters**, *15* (4), 2568 (2015)

4. C. J. Li, W. M. Lü, X. R. Wang, X. P. Qiu, L. Sun , S. W. Zeng, Z. Q. Liu, Z. Huang, Y. L. Zhao, Ariando, T. Venkatesan "Nature of electron scattering in $LaAlO_3/SrTiO_3$ interfaces near the critical thickness" **Advanced Materials Interfaces,** 2, 1400437 (2015) **(Front Cover Featured)**

5. C. J. Li, Z.Q. Liu, W.M. Lü X.R Wang, A. Annadi, S.W. Zeng, Ariando and T Venkatesan. "Tailoring the Two Dimensional Electron Gas at polar $ABO_3/SrTiO_3$ Interfaces for Oxide Electronics" **Scientific Reports**, 5, 13314 (2015)

6. S. Azimi, J. Song, C. J. Li, S. Mathew, M. B. H. Breese, and T. Venkatesan "Nanoscale lithography of $LaAlO_3/SrTiO_3$ wires using silicon stencil masks" **Nanotechnology**, 25, 445301, (2014) **(Front Cover Featured)**

7. K. A. Stoerzinger, W. M. Lu, C. J. Li, Ariando, T. Venkatesan, Y. Shao-Horn*,* "Highly Active Epitaxial $La_{1-x}Sr_xMnO_3$ Surfaces for the Oxygen Reduction Reaction: Role of Charge Transfer" **Journal of Physical Chemistry Letters** 6, 1435 (2015)

8. Z. Q. Liu, L. Sun, Z. Huang, C. J. Li, S. W. Zeng, K. Han, W. M. Lü, T. Venkatesan and Ariando " Dominant role of oxygen vacancies in electrical properties of unannealed LaAlO3/SrTiO3 interfaces." **Journal of Applied Physics** 115, 054303 (2014)

9. Z. Q. Liu, W. Lu, S. W. Zeng, J. W. Deng, Z. Huang, C. J. Li, M. Motapothula, W. M. Lü, L. Sun, K. Han, J. Q. Zhong, P. Yang, N. N. Bao, W. Chen, J. S. Chen, Y. P. Feng, J. M. D. Coey, T. Venkatesan and Ariando "Bandgap control of oxygen-vacancy-induced two-dimensional electron gas in $SrTiO_3$" **Advanced Materials Interfaces,** 1, 1400155 (2014) **(Back Cover Featured)**

10. Z. Huang, Z.Q. Liu, M. Yang, S.W. Zeng, A. Annadi, W.M. Lu, X.L. Tan, P.F. Chen, L. Sun, X. Renshaw Wang, Y.L. Zhao, C.J. Li, J. Zhou, K. Han, W.B. Wu, Y.P. Feng, J.M.D. Coey, T. Venkatesan, Ariando**, "**Biaxial Strain Induced Transport Property Changes in Different Atomically Tailored SrTiO3-based Systems" **Physical Review B** 90, 125156 (2014)

11. Z. Q. Liu, M. Yang, W. M. Lü, Z. Huang, X. Wang, B. M. Zhang, C. J. Li, K. Gopinadhan, S. W. Zeng, A. Annadi, Y. P. Feng, T. Venkatesan and Ariando "Tailoring the electronic properties of SrRuO3 films in $SrRuO_3/LaAlO_3$ superlattices" **Applied Physics Letters** 101, 223105 (2012)

12. S. W. Zeng, Z. Huang, W. M. Lv, N. N. Bao, K. Gopinadhan, L. K. Jian, T. S. Herng, Z. Q. Liu, Y. L. Zhao, C. J. Li, H. J. Harsan Ma, P. Yang, J. Ding, T. Venkatesan, , Ariando. "Two-dimensional superconductor-insulator quantum phase transitions in an electron-doped cuprate" **Physical Review B** 92, 020503(R) (2015).

LIST OF TABLES

LIST OF FIGURES

LIST OF SYMBOLS

R	Resistance
ρ	Resistivity
R_s	Sheet resistance
σ	Conductivity
R_H	Hall resistance
T_C	Curie temperature
K	Kelvin
t	Thickness
V	Voltage
V_g	Gate voltage
e	Elementary charge
I	Current
M	Magnetization
H	Magnetic field
n	Carrier density without thickness normalization
μ	Carrier Hall mobility
uc	Unit cell
CB	Conduction band
VB	Valence band
SQUID	Superconducting quantum interference device
PPMS	Physical properties measurement system
RHEED	Reflection high energy electron diffraction
MR	Magnetoresistance
TMR	Tunnel Magnetoresistance
TER	Tunnel Electroresistance

Chapter 1 Introduction

1.1 Multifunctional oxide interfaces

Smart and multifunctional devices are proliferating in recent years. The ascent of smartphones is the perfect example; it combines the functions of mobile phone, music player, camera, web browser and play station. More intelligent and multifunctional devices are on the way. We can already foresee the smart houses and artificially intelligent robotics in the near future. All these smart devices would not be possible without smart and multifunctional materials. Driven by the trend of increasing demands on smaller and smarter devices, multifunctional materials research is fast growing in recent decades, and is spreading over very wide and integrated research areas ranging from biomaterials, energy conversion and storage, environmental sustainability and smart sensing and actuation. The new direction for future devices is to integrate materials with different functions into to a single device.

However, one obstacle is incompatibility of the traditional different types of materials (metals, ceramics and polymers), in terms of manufacturing and assembly. For example, the brittleness of bulk ceramic materials makes it difficult to be machined like metals. The high temperature treatment of metals and ceramics is not compatible with temperature tolerance range of common plastics. One shortcut is to integrate materials within a similar material system with different functional properties. The components built by materials within the same material group offers the building blocks for higher level of integration of device functions. For example, metal oxide sensors incorporated into porous polymeric matrix as compartment walls within a building can be used to monitor the air quality, provide mechanical support and promote air circulation at the same time. Metal oxide sensors built by a few layers of thin films are the primary step of integration while the sensor polymer incorporation represents a higher level of integration. Upon finishing the

primary materials integration, careful design of the device fabrication process can achieve the goal of multifunctional devices with multiple materials systems.

Within the class of inorganic materials, oxide materials are exciting with diverse electrical, optical and magnetic properties [1, 2]: insulating (e.g. Al_2O_3) semiconducting (e.g. ZnO,TiO_2), metallic (e.g. In_2O_3/Sn, $SrRuO_3$) and superconducting (e.g. $YBa_2Cu_3O_7$); ferroelectric (e.g. $BaTiO_3$), ferromagnetic (e.g. CrO_2), piezoelectric (e.g. Quartz), multiferroic (e.g. $BiFeO_3$) and electro-optic (e.g. $LiNbO_3$). The wide spectra of functional properties make oxides a natural ensemble of materials for primary integration for multifunctional devices.

In industry, many oxides has been used in various areas; for example, Indium Tin Oxide (ITO) is the industrial standard for transparent electrodes which is being widely used in display and solar panel production; Al doped ZnO (AZO) is also proposed as an alternative to ITO due to its low cost and environmental friendliness [3-5]; $Pb(Zr_xTi_{(1-x)})O_3$ (PZT) has been used in ultrasound transducers, sensitive actuators and ceramic capacitors; ultrathin Al_2O_3 and MgO films have been used as tunnel barriers in the devices like magnetic tunneling junctions [6]. In research labs, the wide spectra of the various properties of oxide not only attracted a lot of attention in the basic science study, but also in the applied technologies. For example, understanding and searching for room temperature superconductors in complex oxides remains an unsolved quest for decades; the attempt for creating p-type ZnO for efficient ZnO based blue-white light emit diodes [4, 5]; TiO_2 nanoparticles to be used in the dye sensitized solar cells; catalytic activities of metal oxides are another very hot area in water splitting and carbon dioxide reduction reactions [7, 8]; furthermore, the bio-activity of oxide materials is also increasingly studied in the recent years [9-11]. The oxides research field is promising not only for revealing the mysterious nature of physics laws of the strongly correlated electronic systems, high temperature superconductivity, the magnetic

interactions and coupling between different ferroic orders, but also with full potential to be the key for the future multifunctional device.

With the development of new techniques in oxide materials growth and preparation, along with increasing knowledge in nanoscience and nanoengineering, novel functionality of oxide materials can be engineered and designed by dimensionality and size control. Towards the application side, metal oxides nanoparticles are very common in composites with other materials. For example, metal oxide – carbon composites are investigated as electrodes of lithium batteries, fuel cells and electrochemical capacitors and batteries [12-14]. TiO_2 nanoparticles with dye decoration are the core components of dye-sensitized solar cells [15, 16]. On the fundamental science aspect, interfaces between structurally match oxides thin films are particularly interesting due to the interface- induced novel properties of the system [17]. Well-known examples are interfacial ferromagnetism presented in $LaMnO_3/SrMnO_3$ superlattice where neither $LaMnO_3$ nor $SrMnO_3$ are ferromagnetic [18]; high mobility two dimensional electron gas (2DEG) at the ZnO-Mg:ZnO interface [19] , which is rather similar with GaAs-Al:GaAs semiconductor heterostructures [20]. In these structures, the reservoir of electrons and the conducting channel are physically separated, for this reason, high mobility 2DEG has been demonstrated. Another heavily investigated heterostucture system includes the superconductor-ferromagnetism system, such as YBa_2CuO_3-$La_{0.33}Ca_{0.67}MnO_3$ superlattice [21], they show very interesting phenomena like proximity effect; within the high Tc superconductor system, the superlattice between underdoped (La_2CuO_4) superconductor and overdoped superconductor ($La_{1.55}Sr_{0.45}CuO_4$) can create superconductivity confined at the interface [22]. Functional oxides with ferroic orders are heavily studied in magnetic tunnel junctions, ferroelectric tunnel junctions and multiferroic tunnel junctions as electrodes and tunnel barriers [23], for multi-state memory devices that could respond to multiple environmental

stimuli [24, 25]. Prevailing studies show that ordered heterostructures is one of the important ways to engineering materials functionalities.

Nobel laureate Herbert Kroemer said "the interface is the device", originally referring to the rising electronic, optical and photonic applications in semiconductors heterojunctions. It was found out to be also true for oxide heterostructures, one recent notable example is the discovery of the high mobility 2DEG at the interface between $LaAlO_3$ (LAO) and $SrTiO_3$ (STO) in 2004 by A. Ohtomo and H.Y. Hwang [26]. Subsequent studies show a variety of interesting properties associated with the LAO/STO interface where none are presented in LAO or STO. Novel device concepts based on LAO/STO interface have been under investigation. Clearly the statement "the interface is the device" also applies for heterojunctions formed by oxide thin films [27].

Therefore, this thesis studies novel properties emerging at various oxides heterojunctions. The purpose of my projects include understanding the emerging interface properties, develop proof-of-concept devices which may be important for oxide electronics. With the common feature of the effects of interfaces in oxide heterojunctions, I focused on three interface systems on different functional roles of interfaces: i.e. 1) LAO/STO interfaces for electronic transport properties, 2) $LaMnO_3$ (LMO)/STO and related interfaces on magnetic transition properties and 3) Ultrathin $BaTiO_3$ (BTO) based ferroelectric tunnel junctions (FTJs) for tunneling properties.

In chapter 2, I will give a general introduction on basic physical background, concepts and principles necessary for understanding for my research findings for three distinct oxide interfaces. Chapter 3 describes experimental methods for sample fabrication and characterization. Starting from chapter 4 to 6, experimental findings on the origin of 2DEG (chapter 4), electron scattering mechanisms of 2DGE near the metal-insulator transition (chapter 5) and 2DEG characteristics of

diverse ABO_3/STO interface (chapter 6) are discussed. In chapter 7, atomically sharp magnetic transition in $LaMnO_3$/STO interfaces are discussed. Chapter 8 describes the experimental results of ultrathin BTO based FTJs and chapter 9 provides a brief summary of all research work and perspectives on future research directions.

Chapter 2 Oxide Interfaces

2.1 LAO/STO interfaces

2.1.1 Polar and nonpolar oxide

Polar and non-polar oxide subdivide oxide family in terms of charge distribution, based on the simple electrostatic ionic picture. It is specific to particular crystalline direction for a particular compound. For example, as shown in **figure 2.1**(a), MgO (111) direction consists of alternative layers of Mg^{2+} and O^{2-} with alternative +2e and -2e (per unit cell) charged sheets, so it is polar in (111) direction. While in (100) direction, MgO is non-polar because each atomic layer are a mixture of Mg^{2+} and O^{2-} with equal amount, hence each layer is electrostatically neutral which leads to a non-polar direction of MgO.

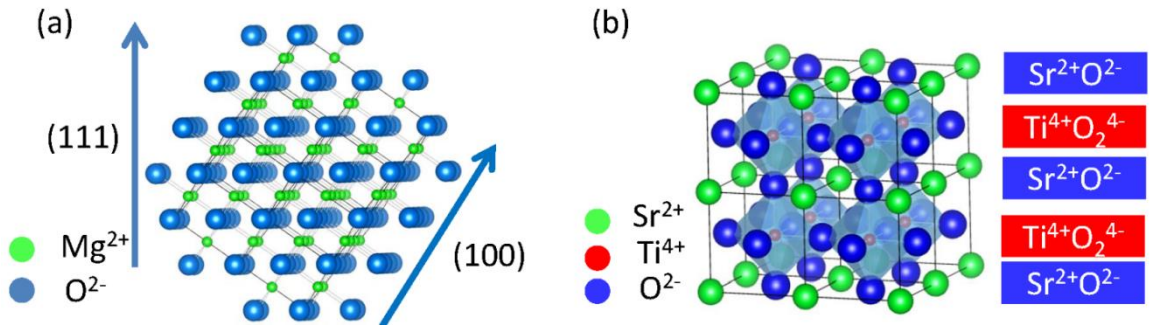

Figure 2.1 Polar and non-polar oxide. (a) (100) of MgO is nonpolar and (111) of MgO is polar. (b) Atomic packing of STO structure, showing corner sharing of TiO_6 octahedral; (100) direction of STO is non-polar.

Another common oxide system for studying the polar and non-polar properties is cubic perovskite structure. Cubic perovskite structure can be denoted as the common chemical formula of ABX_3, where A, B are cations with different cationic sizes and X is anion, the most common anion is O^{2-}. The perovskite structure consists of corner sharing of octahedral BO_6. STO is a common example of perovskite structure as shown in **figure 2.1**(b), showing the TiO_6 polyhedral with corner sharing.

In (100) direction, the perovskite structure consists of alternative SrO and TiO_2 layers. Since both SrO and TiO_2 layers are electrical neutral, STO is non-polar in the (100) direction. LAO has pseudocubic perovskite structure very similar to STO, but with different valence of cations. Trivalent Al and La make $(AlO_2)^{1-}$ and $(LaO)^{1+}$ alternating charge layers, which makes LAO as a polar oxide in (100) direction.

Between polar and non-polar semiconductors (e.g. GaAs grown on Si [28]), it has been always difficult to create high quality interfaces. Fundamental studies found that discontinuity of electrostatic boundary conditions results in roughening of the interface and changes in the stoichiometry of the interface region [29]. For this reason, integration of III-V semiconductors (polar) to silicon (non-polar) industry faces great challenges.

Studies on high quality polar and non-polar oxide interfaces only started in the last decade due to technique constraints. The starting point is to prepare atomically flat oxide surfaces. Kawasaki *et al.* [30] firstly demonstrated atomic terraces on TiO_2- terminated STO substrates by selective etching using buffered HF solution. This work quickly stimulated similar works on treating various substrates (e.g. A-site $NdGaO_3$ [31], $KTaO_3$ [32]) to achieve atomically flat surfaces. The other factor is the advances of the growth techniques on functional oxides. The most common growth techniques for growth of oxide thin films are pulsed laser deposition (PLD) and molecular beam epitaxy (MBE), increasingly, sputtering and chemical vapor deposition have been utilized for some oxide growth. Reflection high-energy electron diffraction (RHEED) is an important technique for *in-situ* monitoring the growth process; it provides information on the nucleation and growth modes of the thin films and offers an *in-situ* measurement of the film thickness. Furthermore, the advance of scanning transmission electron microscopy (STEM) enabled microscopic imaging and identifying the atoms near the interface. With the help of high resolution electron energy loss

spectroscopy (EELS), the electronic states of the interface ions can be clearly identified, which greatly helped us understand the origin of novel properties arising at oxide interfaces. With the accumulation of knowledge on substrate treatment, thin film growth and characterization, the promising future of multifunctional oxide devices for oxide electronics is progressing rapidly.

2.1.2 STO and LAO

STO is a band insulator with band gap of 3.2 eV and lattice constant of 3.905 Å. STO crystal is a very important material for oxide research and it has a lot of applications in other fields. For example, it has been utilized as a grain-boundary barrier layer capacitor [33], oxygen gas sensor [34] and substrate for epitaxial growth of high temperature superconducting thin films [35]. STO has a cubic to tetragonal phase transition at around 105 K, a tetragonal to orthorhombic phase transition at around 60 K and possibly another orthorhombic to rhombohedral phase transition at around 30 K [36-38]. Defect is an important issue for complex oxides. Oxygen vacancies are very easy to be induced in STO by thermal annealing in vacuum and ion milling [39-43]. STO with low concentration of oxygen vacancy shows gray color, and the color becomes dark blue or black when oxygen vacancy concentration increases. Photoluminescense (PL) can also be introduced by oxygen vacancy in STO [43, 44], so PL spectroscopy intensity offers a qualitative measurement on the oxygen vacancies present in STO. It has been one of the most important substrates for perovskite structured oxides. The easy treatment procedure to achieve TiO_2-terminated atomic flat surface in STO makes it advantageous to be used as a substrates for abrupt interfaces with a variety of oxides.

LAO is also a band insulator with a band gap of 5.6 eV and lattice constant of 3.791 Å. Similar to STO, LAO serves as an important substrate in a lot of oxide growth, such as YBCO and TiO_2 [45]. LAO maintains a rhombohedral phase at room temperature and transforms into a cubic phase at

temperatures above 875 K [46, 47]. Because of the rhombohederal phase at room temperature, LAO develops mesoscopic twin structures visible under naked eyes. When it is in the form of epitaxial thin film form, it is strained to match the substrates, so the cubic phase is maintained at room temperature.

Neither LAO nor STO generate too much scientific excitement, very interesting results were observed at the LAO/STO heterojunctions. In the following section, the major experimental results and basic understanding on LAO/STO properties and mechanisms are reviewed.

2.1.3 LAO/STO interface: properties

Ohtomo and Hwang first published the results on conducting interface of LAO/STO in 2004 [26]. The result is quite striking as a conducting interface is created out of insulators. The key elements are (1) n-type interface (atomic layers stacking as $SrO\text{-}TiO_2\text{-}LaO\text{-}AlO_2$) is conducting while p-type interface (atomic layers stacking as TiO_2 -$SrO\text{-}AlO_2\text{-}LaO$) is insulating (2) n-type interface shows high mobility (up to 10k $cm^2V^{-1}s^{-1}$) at low temperature. The suggested mechanism is electronic reconstruction induced by the diverging electrostatic potential resulted from the polar discontinuity. Since then, many researchers started to study this system, there are two general directions: one is on the electronic properties and potential electronic applications of the LAO/STO interface, and the other focused on the origin or mechanism of formation of the 2DEG at the interface with some overlap between these two directions.

The electronic properties on LAO/STO interfaces include metal-insulator transition, superconductivity and magnetic properties at the interface. In 2006, Thiel *et al.* [48] demonstrated that metal- insulator transition occurs with a critical thickness of 4 unit cell (uc) (~1.6 nm) of LAO overlayer even which some variation in deposition conditions (**figure 2.2** left); furthermore, 3uc

LAO on STO can be back gated to be conductive though originally it is insulating. Up to now, it is found that the critical thickness of 4 uc is quite robust for any preparation condition except very high oxygen pressure deposition (~10^{-1} Torr). Soon after, Reyren *et al.* [49] discovered that the interface is superconducting with critical temperature about 200 mK, and the superconducting thickness is confined to 10 nm, displaying a two-dimensional superconducting electron gas. Later, Caviglia *et al.* [50] used electric field effect to map out the transition between superconducting states and normal states, and it also demonstrates that superconducting states can be tuned by the local electric fields (**figure 2.2** right).

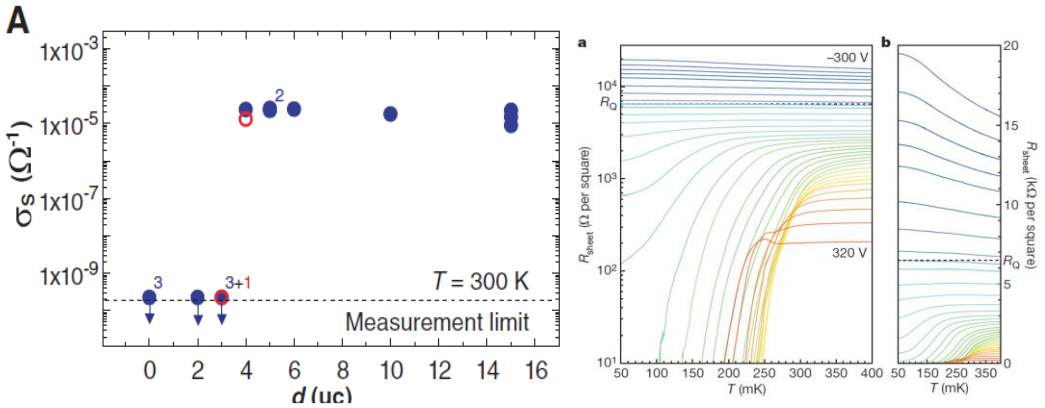

Figure 2.2 Electrical properties of LAO/STO interface. (Left) Sheet conductance dependence on the crystalline LAO overlayer thickness showing metal insulator transition at 4 uc, adapted from [48]. (Right) Electrical field tuning showing the superconductor insulator transition with a negative voltage applied, adapted from [50].

Another intriguing fact is the unusual magneotransport properties firstly reported by Brinkman *et al.* [51], namely, resistivity minimum fitting to the Kondo effect, large negative magnetoresistance and magnetic hysteresis of sheet resistance at low temperature. These results indicate the weak ferromagnetic nature of the interface. Neither STO nor LAO is magnetic, so the ferromagnetic interface is really surprising. Superconductivity and ferromagnetism reported in a single system makes it natural to ask the question of how ferromagnetism coexists with superconductivity.

Ariando *et al.* [52] proposed electronic phase separation model claiming that transferred charges form inhomogeneous nanoscopic patches of magnetic domains and relatively larger superconducting (diamagnetic) domains. Later, several groups [53, 54] macroscopically demonstrated the coexistence of ferromagnetism and superconductivity (**figure 2.3** left) by magnetic torque measurements while Bert *et al.* [55] directly imaged the magnetic dipoles and superconductivity mapping of the LAO/STO interface using scanning superconducting quantum interference device (SQUID) (**figure 2.3** right). It therefore confirmed the nanoscale phase separation of superconductivity and ferromagnetism in quasi-two dimension. The remaining question is how these two properties correlate with each other.

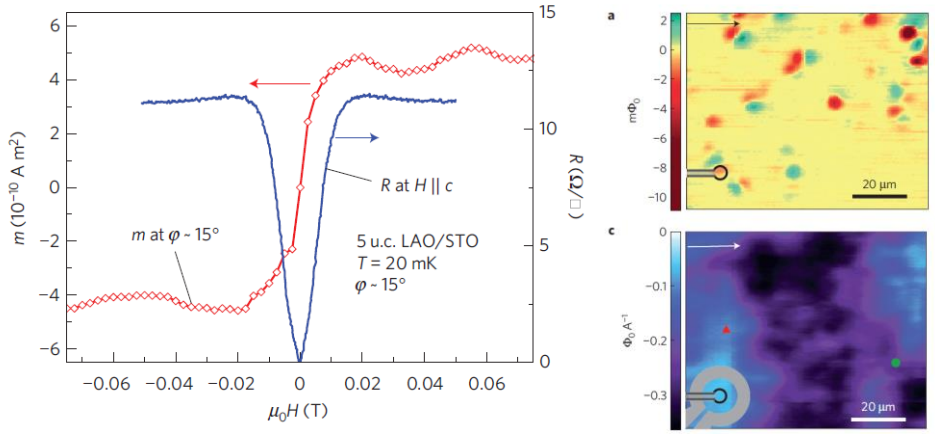

Figure 2.3 Coexistence of ferromagnetism and superconductivity at LAO/STO interface. (Left) Magnetic moments and sheet resistance dependence on the external magnetic field applying parallel to c-axis showing a coexistence region, adapted from [54]. (Right) Scanning SQUID mapping of magnetic dipoles and superconducting domains on the same sample of LAO/STO interface, adapted from [55].

2.1.4 LAO/STO interfaces: device and application concepts

Besides studying the novel physical phenomena emerged at LAO/STO interface, substantial efforts have been made to build electronic devices based on LAO/STO. The most significant properties for applications are quasi-2D feature of the high mobility electron gas and field effect

on metal-insulator transition. Early work has shown using a gating field, 3 uc originally insulating sample can be tuned to be conducting [48]. Later this properties has been used for diode design to enhance the breakdown voltage [56]. Further, the microscopic version of local gating using and conducting atomic force microscope (c-AFM) probe has been demonstrated by Cen *et al.* [57, 58]. They could create 2DEG nanowires with line width ~2 nm by applying a positive bias and erase the nanowires by applying a negative bias (see **figure 2.4** left). Later they used this technique demonstrated nanoscale single-electron-transistor [59], tunnel junctions [57] and photodetector [60], which really proves the concept of nanoscale devices based on LAO/STO interfaces. Just recently, Irvin *et al.* [61] from the same group reported the high mobility (~350 $cm^2V^{-1}s^{-1}$) LAO/STO nanowires (width ~8 nm) at room temperature, which is about 2 orders higher than the common unpatterned LAO/STO 2DEG. High mobility at room temperature make LAO/STO nanowires viable for room temperature electronic devices.

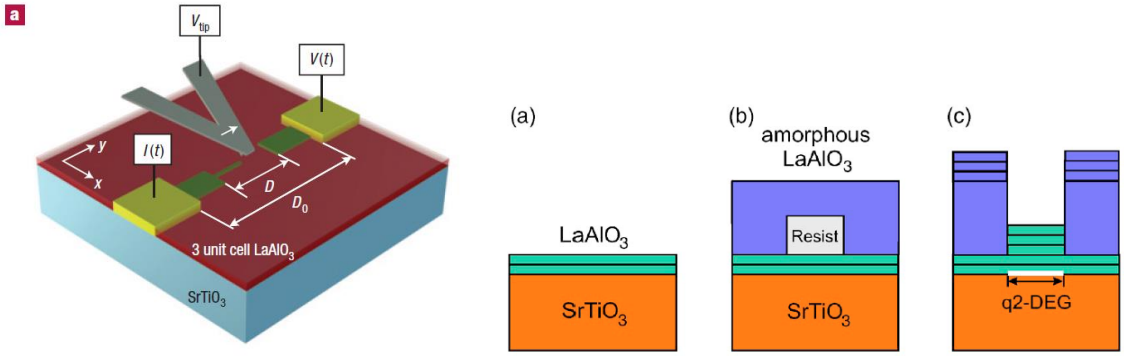

Figure 2.4 Patterning LAO/STO interfaces. (Left) C-AFM probe bias writing of conducting nanowires out of the originally insulting 3 uc LAO/STO at room temperature, adapted from [58]. (Right) Electron beam lithography procedures to pattern conducting 2DEG, adapted from [62].

Other patterning techniques, like e-beam lithography and photolithography, has been used to pattern LAO/STO. Schneider *et al.* [62] (**figure 2.4** right) have developed the scheme "growing 2 uc crystalline LAO-masking unwanted area with amorphous LAO- deposition another 3uc

crystalline LAO" to get the 2DEG only exist in the desired region, conducting features size ~200 nm were demonstrated. Integration of LAO/STO 2DEG to silicon is also another important step for the potential application of the 2DEG at the interface. Park *et al.* [63] reported growing LAO/STO//Si structures, despite the structural dislocations present on the heterostructure, the room temperature electronic performance and the c-AFM probe switching capability do not vary too much with those interface grown on bulk STO substrates. The applications on LAO/STO nano devices are really promising though a lot of technical problems such as large area growth need to be tackled.

2.1.5 LAO/STO interfaces: origins

Although the interesting physics and technical promise presented in LAO/STO interface, the fundamental question on the origin of 2DEG is still under debate. Currently, there are three major mechanisms [64]. First is interface electronic reconstruction to avoid the polarization catastrophe induced by the polar discontinuity at the interface between polar LAO and nonpolar STO (**figure 2.5**) [65-67]. The supporting experimental results include 4 uc critical thickness of metal-insulator-transition for a variety of preparation conditions [48], the asymmetry of conducting n-type interface and non-conducting p-type interface [26], 3 uc LAO/STO can be induced to be conducting upon gating [48, 57, 59, 60]. Other polar materials (e.g. $NaAlO_3$, $PrAlO_3$, $NdGaO_3$ [68], $LaGaO_3$ [69], $DyScO_3$ [70] and $LaVO_3$ [71]) interfaces with TiO_2-terminated STO also reproduces the 2DEG, tunable critical thickness when the polar material is diluted by a nonpolar material [72]. However, X-ray photoemission spectroscopy studies did not observed the potential build up in LAO as large as predicted by polarization catastrophe model [73]. Also there are a few polar oxides, such as $LaMnO_3$ and $LaCrO_3$ [74], which cannot create 2DEG at ABO_3/STO interface. Second is doping by thermal interdiffusion of Ti/Al or La/Sr atoms at the interface [75]; Inter diffusion of

cations at the interfaces causes of an effective solution of $La_xSr_{1-x}TiO_3$, which is conducting (see **figure 2.6a**). Later, interdiffusion mechanism was discounted by Reinle-Schmitt *et al.* [72], which demonstrated the critical thickness scaling with polar strength (proportion) of the overlayer made of solid solution of LAO and STO. It is also in conflict with the experimental results that p-type LAO/STO interfaces [26] and interfaces created by growing STO films on LAO substrates (i.e. STO/LAO) are insulating due to polarity has been compensated in the bulk LAO [76]. A third possible mechanism is creation of oxygen vacancies in STO substrates during the deposition process [77-80] (**see figure 2.6b**). Oxygen vacancies are known to introduce a shallow intragap donor level close to the conduction band of STO [81], and their action may be specific to this one substrate. Up to now, it is really hard to differentiate 2DEG originated from electronic reconstruction and oxygen vacancies. In chapter 4, we did a systematic study to tackle this problem.

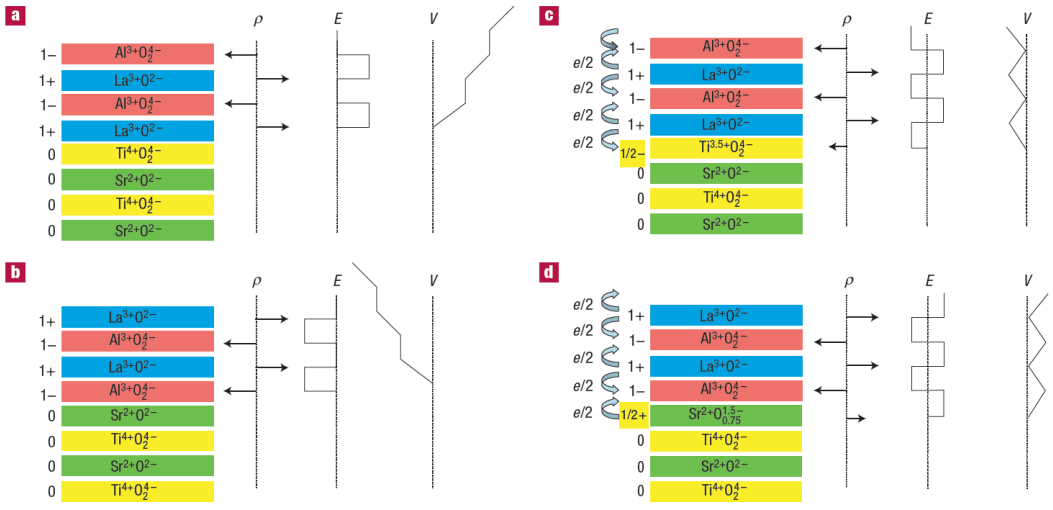

Figure 2.5 Polarization catastrophe model of LAO/STO interface. (a) n-type interface showing diverging electrostatic potential. (b) p-type interface showing diverging electrostatic potential. (c) n-type interface electronic reconstruction by electron transfer from LAO to STO to avoid the diverging electrostatic potential, resulting the interface Ti^{4+} to be $Ti^{3.5+}$. (d) p-type interface electronic reconstruction by hole transfer from LAO to STO to avoid the diverging electrostatic potential, resulting the interface oxygen vacancies formation. Adapted from [65].

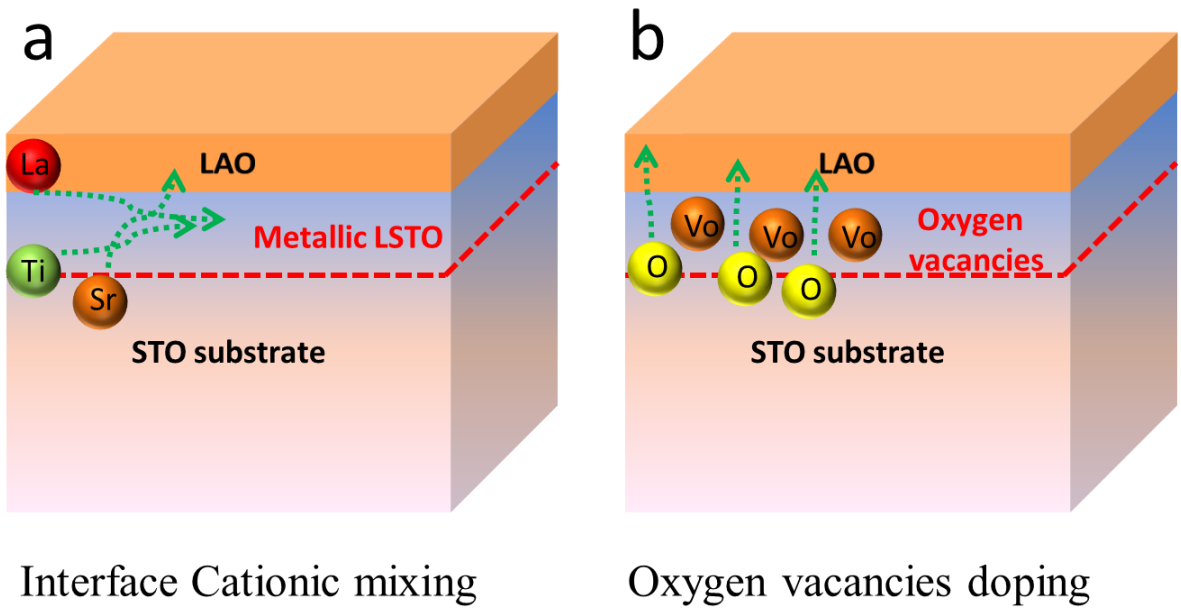

Figure 2.6 Cationic intermixing and oxygen vacancies are also possible reasons for 2DEG at LAO/STO interfaces. (a) Schematic representation of La/Sr intermixing at the STO surfaces during growth forming a conductive $La_xSr_{1-x}TiO_3$ thin layer in the interface region. (b) Schematic presentation of oxygen vacancies formation due to deposition of LAO, where Al has oxygen affinity, it grabs oxygen out of STO substrates, leading oxygen vacancies formation at the top surfaces of STO.

2.2 $LaMnO_3/SrTiO_3$ interfaces

2.2.1 $LaMnO_3$

Various interesting properties have been demonstrated in $LaMnO_3$ (LMO) bulk, thin films and multilayers, ranging from the occurrence of orbital waves to its use as a catalyst for water splitting [82-85]. LMO is a Mott insulator with an orthorhombic structure, based on a $\sqrt{2}a_0$, $\sqrt{2}a_0$, $2a_0$ unit cell where $a_0 \approx 3.9$ Å is the elementary perovskite unit cell parameter. In stoichiometric LMO, La and Mn are both 3+ ions. Therefore, LMO is a polar material which contains alternatively charged $(LaO)^{1+}$ and $(MnO_2)^{1-}$. Mn^{3+}, with electronic configuration $t_{2g}^3 e_g^1$ and spin $S = 2$, is a Jahn-Teller ion. If LMO had a perfect cubic perovskite structure one might expect a conducting ground state

due to the mobility of the unpaired electron in the degenerate e_g band. However the e_g orbital degeneracy is lifted by the Jahn-Teller effect, and distorted MnO_6 octahedral line up with alternating long and short Mn-O bonds in the *a-b* plane, leading to orbital ordering, which contributes to the electron localization [86]. As a result of superexchange coupling [87], the compound is an A-type antiferromagnet, with Mn spins ferromagnetically aligned in-plane, and alternate planes aligned antiferromagnetically. The Néel temperature is ~ 140 K. In bulk, the antiferromagnetism can be slightly canted to produce a weak ferromagnetism of ~ 0.18 μ_B per uc [88-90], which is attributed to the antisymmetric Dzyaloshinskii-Moriya interaction introduced by rotation of the MnO_6 octahedra. In thin films, ferromagnetism accompanied with insulating behavior is often observed, with a Curie temperature of ~ 115 K [91]. The origin of this ferromagnetism is still unclear, but in addition to the above-mentioned mechanism, defects and epitaxial strain can be important factors [91-93].

2.2.2 $LaMnO_3/SrTiO_3$ interfaces

The conductivity between LAO/STO interface and the simple electrostatic picture have invoked extensive studies on replacing LAO with other polar oxides. Among which, $NdGaO_3$, $LaGaO_3$, $PrAlO_3$, $NdAlO_3$, $DyScO_3$, $LaVO_3$, $GdTiO_3$, $LaTiO_3$ crystalline films grown on STO (100) substrate shows 2DEG at the interface. $LaCrO_3$/STO (100) interfaces are found to be insulating due to the cationic intermixing, instead of electronic reconstruction, is more efficient to diminish the otherwise divergent electrostatic potential [74, 94]. $LaMnO_3$ and low Sr doped $La_{1-x}Sr_xMnO_3$/STO (100) interface are found to be insulating as well. Since $LaMnO_3$/STO is a polar/non-polar interface, polar catastrophe is also expected, but why there is no interface conductivity?

Looking at the band diagrams of LMO/STO and LAO/STO (see **figure 2.7**), the difference lies in the relative magnitude of the band gap between the LMO and LAO. The band gap of LMO of 1.3 eV is smaller than that of STO (3.2 eV) while LAO band gap (5.6 eV) is larger than that of STO. Using the simple polar catastrophe model, electrostatic potential build up is expected in both cases. That is, both LMO and LAO valence band/conduction band bend upwards with the increasing thickness of LMO or LAO. When the band bending exceeds STO conduction band edge, electrons get transferred to the STO conduction band, which leads to 2DEG at the interface. This is different for LMO/STO interface. Due to LMO's smaller band gap, the band bending will lead to electron transfer the valence band of the LMO to the conduction band of LMO itself. In this picture, electron reconstruction occurs within LMO layer near the LMO/STO interface. Hence we will expect nonconductive interface, instead some other properties are changed. In a recent transmission electron microscopy-electron energy loss spectroscopy (TEM-EELS) studies [95] on the LMO/STO interface indeed found out that Ti valence at the LMO-STO interfaces remained at Ti^{4+} state while Mn valence near the interface are reduced to Mn^{2+} state. It supports the self-electronic reconstruction picture.

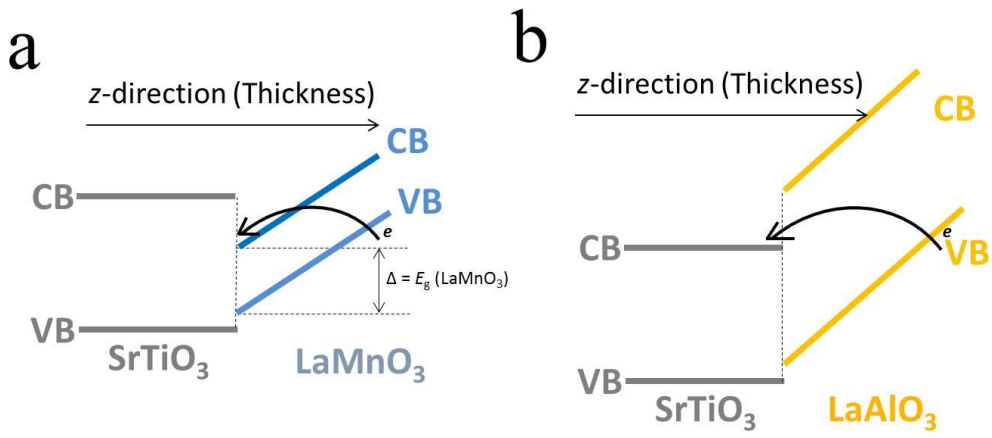

Figure 2.7 Electronic reconstruction of LMO/STO and LAO/STO interfaces due to polarization catastrophe. (a) Self electronic reconstruction of LMO layer in LMO/STO interface (b) electronic reconstruction from LAO to STO in LAO/STO interface.

The natural property to be considered is magnetic properties for LMO/STO interface due to the close correlation between the electronic and magnetic phases in LMO. **Figure 2.8** shows the example M-H and M-T curve for 12 uc LMO and $CaMnO_3$ (CMO) grown on STO. LMO film shows a typical M-H hysteresis of ferromagnetic features with ~ 0.2 T coercive field with a T_C of ~100 K. In contrast, typical diamagnetic features are shown in CMO film which mainly come from the STO substrates, hence no significant magnetic signal is from CMO. CMO remains in antiferromagnetic in nature. Since CMO is a non-polar material, CMO/STO experiences no polar discontinuity. Antiferromagnetic phase are likely to be preserved. The difference of the magnetism between the two strongly indicates the proposed self-electronic reconstruction model is the origin of magnetic phase in LMO films in LMO/STO heterostructures. To further test this hypothesis, a thickness dependent magnetic property was investigated from 1 to 24 uc. Both global measurement (Vibrating sample magnetometer-SQUID) and local scanning magnetic measurement by scanning SQUID microscopy (SSM) were carried out to eliminate possible magnetic signals from

contaminations. A critical thickness for the magnetic phase transition was found to be 6 uc. More details are illustrated in chapter 7.

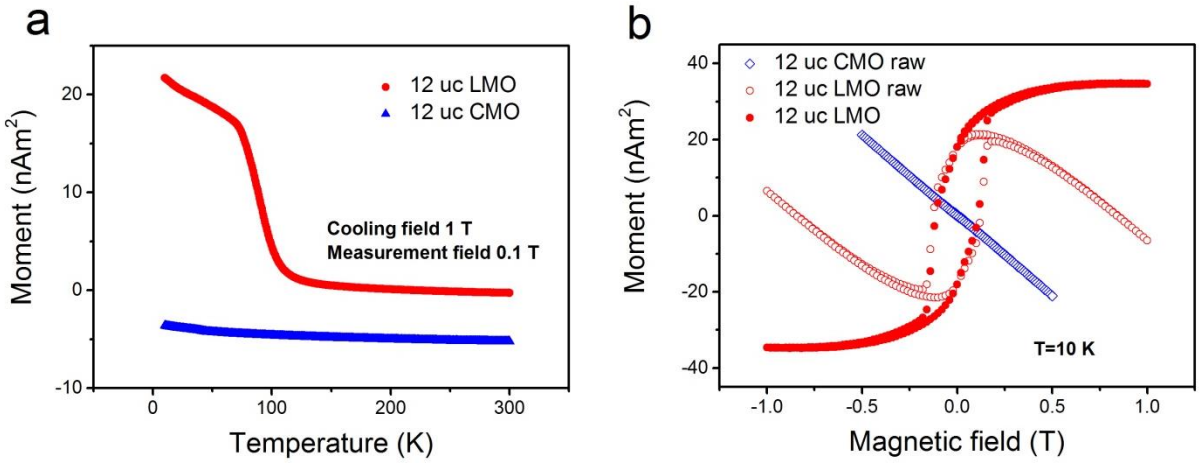

Figure 2.8 Different magnetic properties between 12 uc LMO and CMO films grown on STO substrates. (a) Field cooling curve for LMO shows a ferromagnetic behavior with T_c ~ 100 K while CMO shows no additional signal beyond diamagnetism from STO. (b) LMO films shows M-H hysteresis loop after subtraction of diamagnetic contribution from STO while CMO shows no explicit magnetic response at 10 K.

2.3 Ultrathin $BaTiO_3$ based ferroelectric tunnel junctions

2.3.1 Nanoscale Ferroelectricity

Ferroelectricity is another common ferroic order other than ferromagnetism which is extremely important for modern technologies. For a long time, ferroelectric study has only been confined in thick (~ μm) ferroelectric films. Nanometer scale ferroelectricity (nanoferroics) [96] would only be possible in recent years due to dramatic improvement in materials fabrication techniques. It has attracted extensive studies on the stability in nanometer scale. Is there a critical thickness for stable ferroelectrictiy? If there is, what is the critical thickness? Initially, theoretical scientists predict rather thick critical thickness (~ 40 Å BTO), but experimentalist report thinner stable ferroelectric films with better thin film fabrication and ferroelectricity characterization techniques. To account

for this discrepancy, the effect of the ferroelectric layer/electrode interface has been included to describe the experimental picture. In this model, Junquera *et al.* [97] predicted 24 Å (6 uc) critical thickness for $SrRuO_3$/BTO/$SrRuO_3$ geometry. Ghosez *et al.* [98] reported 3 uc of critical thickness for $PbTiO_3$ films, and Sai *et al.* [99] even reported stable ferroelectricity down to 1 uc of BTO and $PbTiO_3$. Experimentally, ferroelectricty in 2 monolayer ferroelectric polymer was reported [100]. 1 uc of BTO embedded in BTO/STO supperlattice has been shown to be ferroelectric via Raman studies on soft phonon modes [101]. The observed nanoscale ferroelectricity is not only important for physical studies but also established the basis for nanoscale ferroelectric devices for novel electronic applications.

2.3.2 Ferroelectric and multiferroic tunnel junctions

One natural application for nanoscale ferroelectricity is ferroelectric tunnel junctions (FTJs). An FTJ is a tunnel junction with ferroelectric spacer with structure of M1/FE/M2, where M1 and M2 are electrodes and FE is the ferroelectric spacer (see **figure 2.9**). The thickness of ferroelectric layer is usually less than 4 nm. The application of FTJ relies on the effect called tunnel electrical resistance (TER). It means that the resistance across an FTJ is dependent on the polarization direction of the ferroelectric layer. TER ratio is defined as

$$TER = \frac{R(\leftarrow) - R(\rightarrow)}{R(\rightarrow)} \times 100\ \% \qquad \text{eq2.1}$$

,where $R(\rightarrow)$ and $R(\leftarrow)$ is the junction resistance when the polarization is pointed right and left direction, respectively. The TER is in parallel to tunnel magnetoresistance (TMR) concept in magnetic tunnel junctions (MTJs). TER effect offers a fast and accurate way to read out the polarization state of the ferroelectric layer in a non-destructive way. It has paved the road for FTJs' application for memory and other electronic applications.

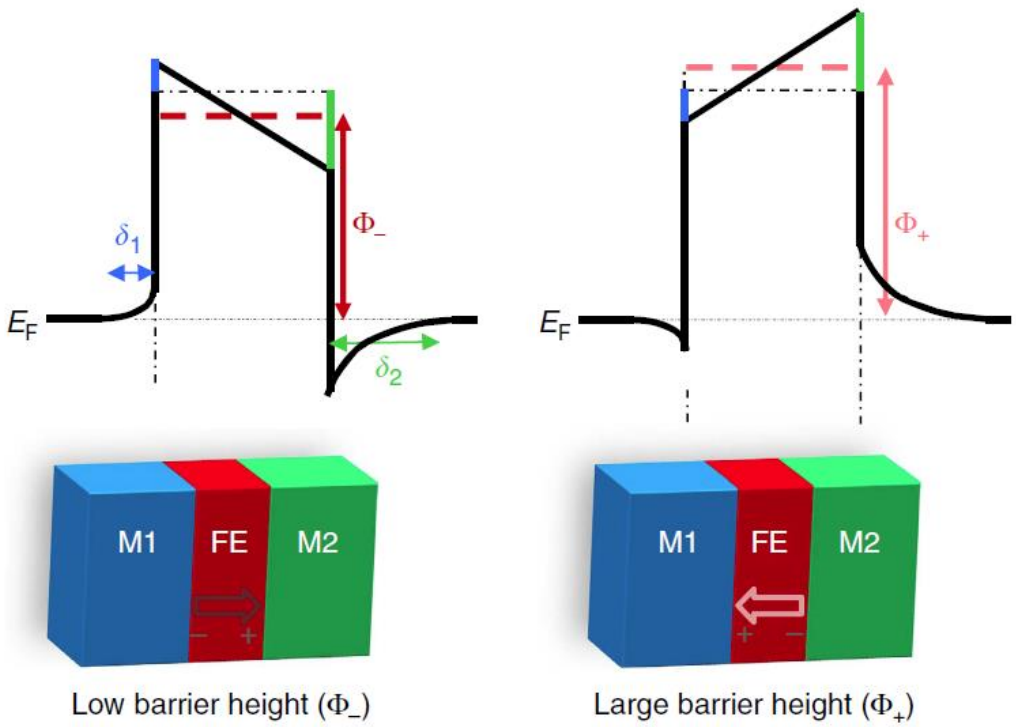

Figure 2.9 Schematic of an FTJ. The resistance state of the FTJ is controlled by the ferroelectric polarization direction, which is determined by the effective tunnel barrier height. Left image illustrates the "on" (low resistance) state and right is the "off" (high resistance) state. Adapted from ref. [102].

In an MTJ, both electrodes are ferromagnetic (e.g. FeCoB) and the tunnel barrier is a dielectric material (e.g. Al_2O_3 and MgO). The junction resistance is dependent on the parallel or antiparallel relationship of the direction of magnetic moment of the two electrodes. The TMR is defined as

$$TER = \frac{R(\leftarrow\rightarrow) - R(\rightarrow\rightarrow)}{R(\rightarrow\rightarrow)} \times 100\ \% \qquad \text{eq2.2}$$

,where $R(\leftarrow\rightarrow)$ and $R(\rightarrow\rightarrow)$ is the junction resistance when magnetic moment of two electrodes are antiparallel and parallel, respectively. If electrodes of an FTJ are replaced with ferromagnetic metals, a hybrid FTJ and MTJ are constructed. TER and TMR could coexist in this hybrid structure and this hybrid junction are called multiferroic tunnel junction (MFTJ) [103]. The incorporation of single phase multiferroic materials into MFTJ also promises another direction for MFTJ

construction. **Figure 2.10** summarizes a comparison of the structure and tunnel junction resistance characteristics of an FTJ, MTJ and MFTJ. When considering possible memory applications, an FTJ has a few advantages compared to a MTJ. First, the TER ratio of an FTJ is much larger than the TMR ratio of a common MTJ. Second, FTJs are voltage/field -controlled device, while MTJs are current controlled device. The energy consumption is much lower than the spin transfer torque-magnetic random access memory (STT-MRAM). In another way, combine an FTJ with a MTJ to build a voltage-controlled MTJ is also of high interest of many researchers. In the following few paragraphs, I will review the research efforts on FTJs and discuss motivation of my work on FTJs.

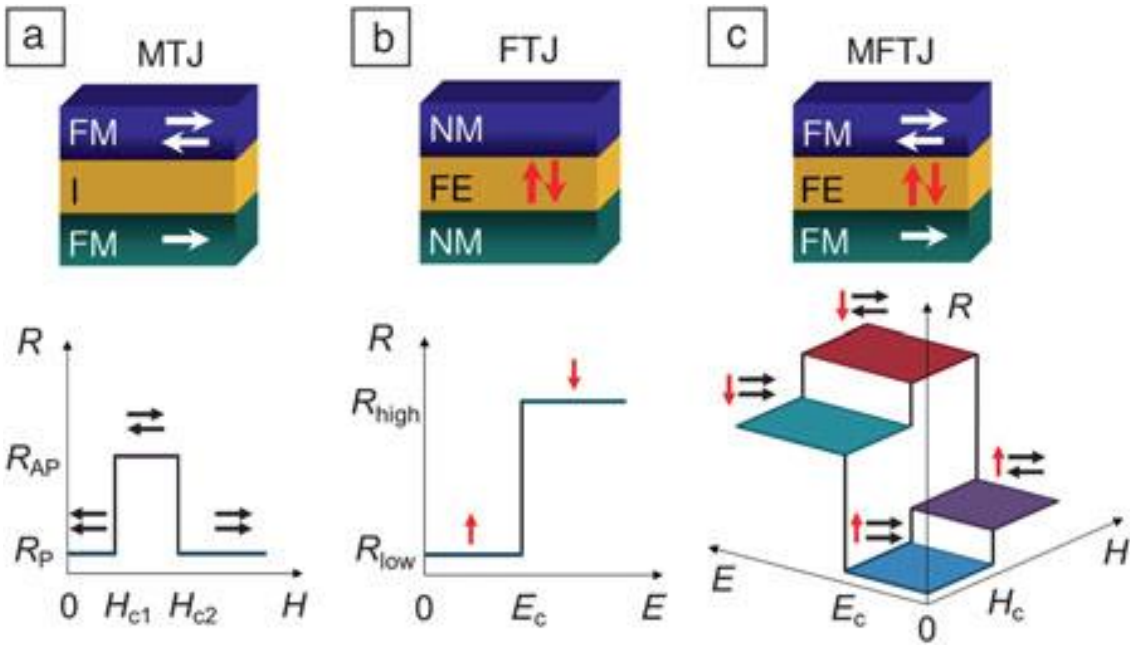

Figure 2.10 Comparison between an (a) MTJ, (b) FTJ and (c) MFTJ with its tunnel resistance dependence on magnetic field (H) for MTJ, electric field (E) for FTJ and both H and E for MFTJ. Image adapted from ref.[103]

The TER concept was initially proposed by Esaki *et al.* [104], but only get intensive experimental studies in the past decade [102, 103, 105-108]. The field is considered established after the

demonstration of the local correlation between a polarization state and the tunnel current intensity [109, 110]. As shown in **Figure 2.11**, c-AFM and piezoresponse force microscopy (PFM) patterns clearly show the difference of resistance is resulted by the polarization state of the ferroelectric film. Later, Chanthbouala *et al.*[108] showed on/off ratio, $R(\uparrow)/R(\downarrow)$, about 100 (TER ~10000%) in simple Co/BTO/$La_{0.67}Sr_{0.33}MnO_3$ junction gown on $NdGaO_3$ substrate at room temperature. Further, FTJ integration on silicon has been demonstrated [107]. The technology promise on FTJ based memory is huge.

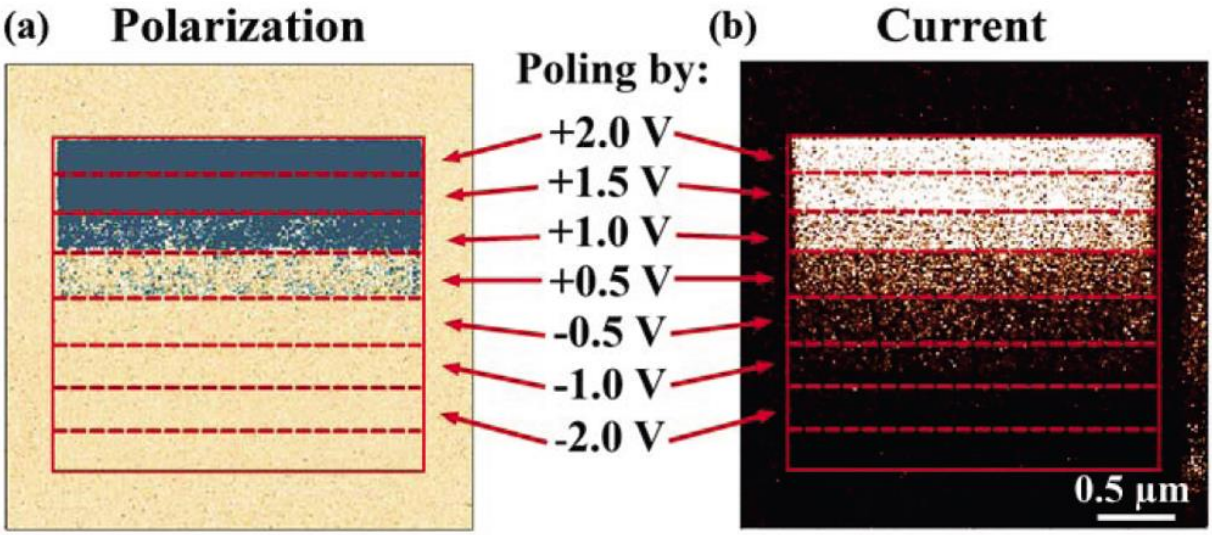

Figure 2.11 Correlation of the tunnel junction resistance with polarization states by PFM and conductive AFM. Different poled states (shading) in PFM (a) corresponds to different resistance/conductive states as shown in (b) c-AFM images. Adapted from ref. [109].

To realize the potential, researchers carried out extensive fundamental studies on the FTJ. In general, there are two major directions for FTJ physical properties research. First is on integration FTJ to conventional MTJ. The research is also in-line with another current hot research topic: multiferroics. The electromagnetic coupling at interfaces between the ferroelectric spacer and the ferromagnetic electrodes are of particularly of interest. If the coupling is strong, TMR ratio is controlled by the polarization states [24, 111]. **Figure 2.12** shows the negative TMR ratio in

Fe/BTO/$La_{0.67}Sr_{0.33}MnO_3$ is controlled up to 30% by the polarization direction of the 1 nm BTO film at low temperature. However, the underlying mechanism is still to be understood clearly.

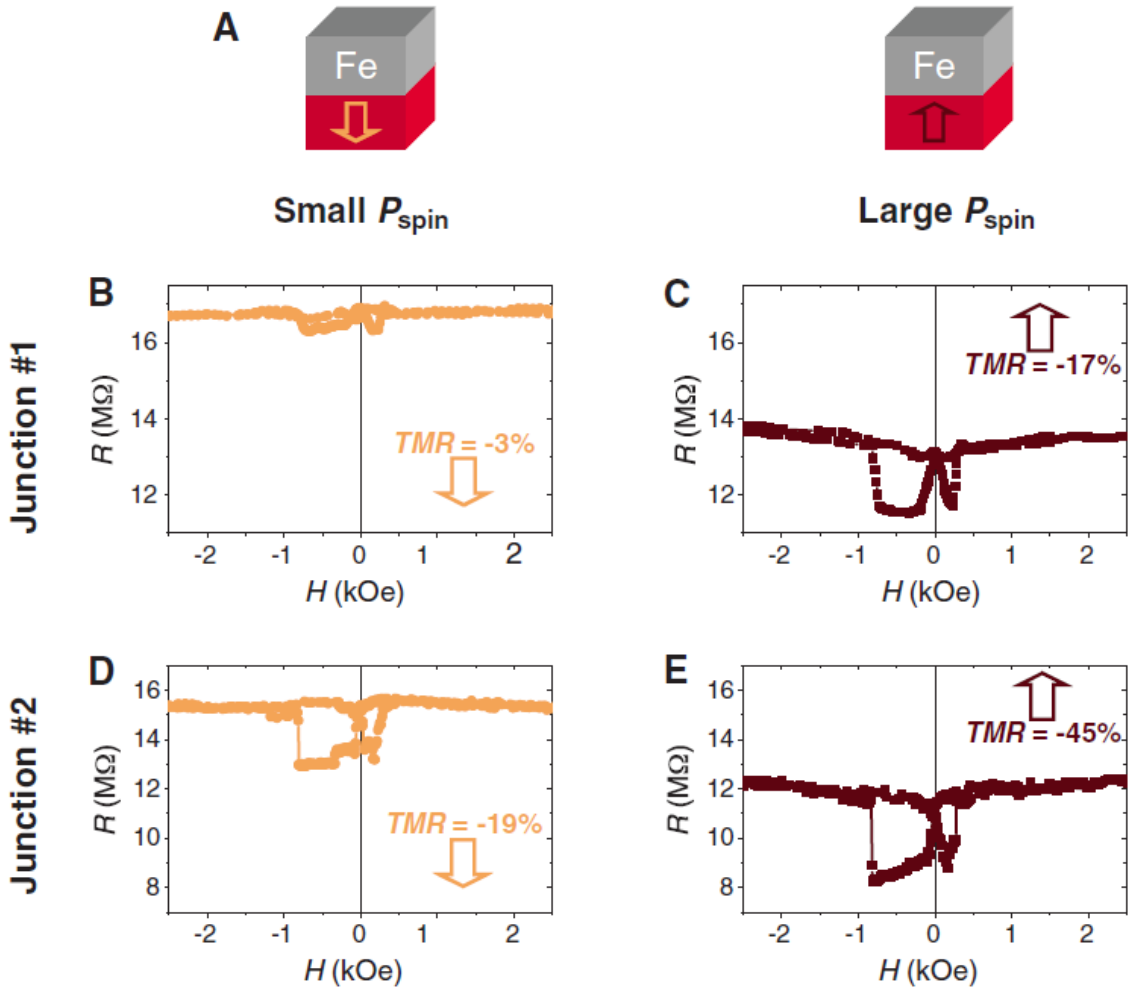

Figure 2.12 Ferroelectric control of TMR. (a) Schematics for different polarization direction relative to top Fe layer. (b) and (c) R(H) curve (V_{dc}=50 mV, T=4.2 K) for junction #1 with the ferroelectric polling in down and up direction, respectively. (d) and (e) similar R(H) curves for junction #2. Adapted from ref. [24].

On the other hand, if the coupling is weak, the MFTJ is more like a simple superposition of a MTJ and an FTJ. TER and TMR are presented independently in a $La_{0.7}Sr_{0.3}MnO_3/Ba_{0.95}Sr_{0.05}TiO_3/La_{0.7}Sr_{0.3}MnO_3$ junction at room temperature as illustrated in **figure 2.13**. It shows a four-state memory device responsive to both electric and magnetic field. A

few researchers also demonstrated same functionality using multiferroic (e.g. $BiFeO_{3}$[112, 113] and $La_{0.1}Bi_{0.9}MnO_{3}$[114]) thin film as the tunnel barrier.

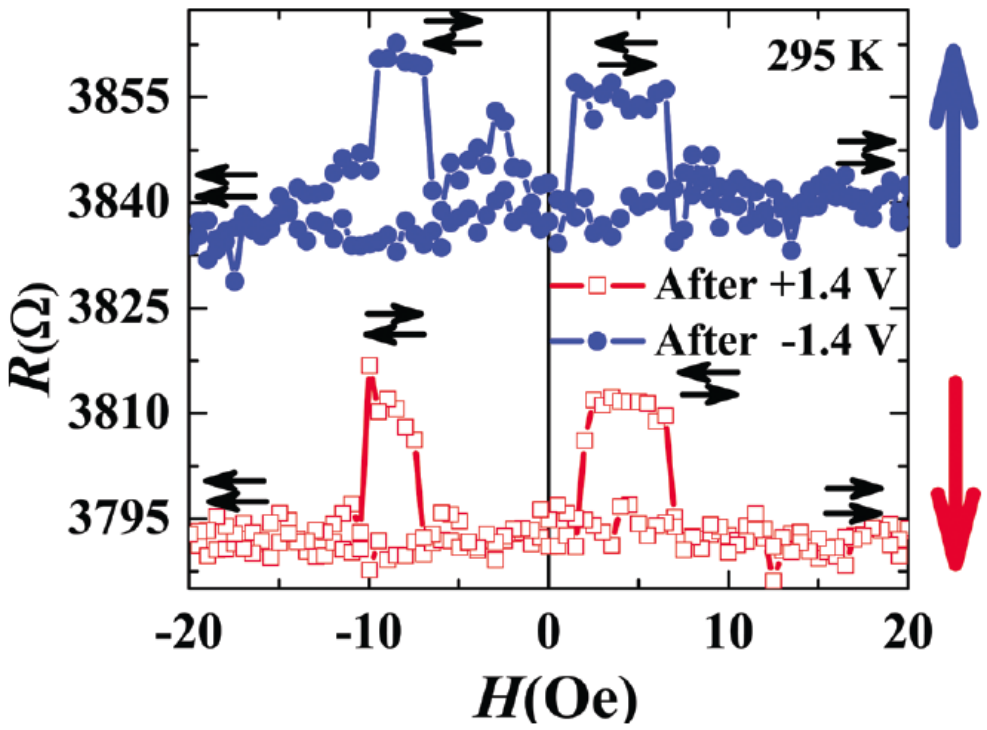

Figure 2.13 Coexistence of TMR and TER in an MFTJ shows a four-state resistance states dependent the relative magnetization and ferroelectric polarization direction. The TMR ratio itself is not strongly affected by polarization direction. The measurement temperature is at room temperature. Adapted from ref. [25].

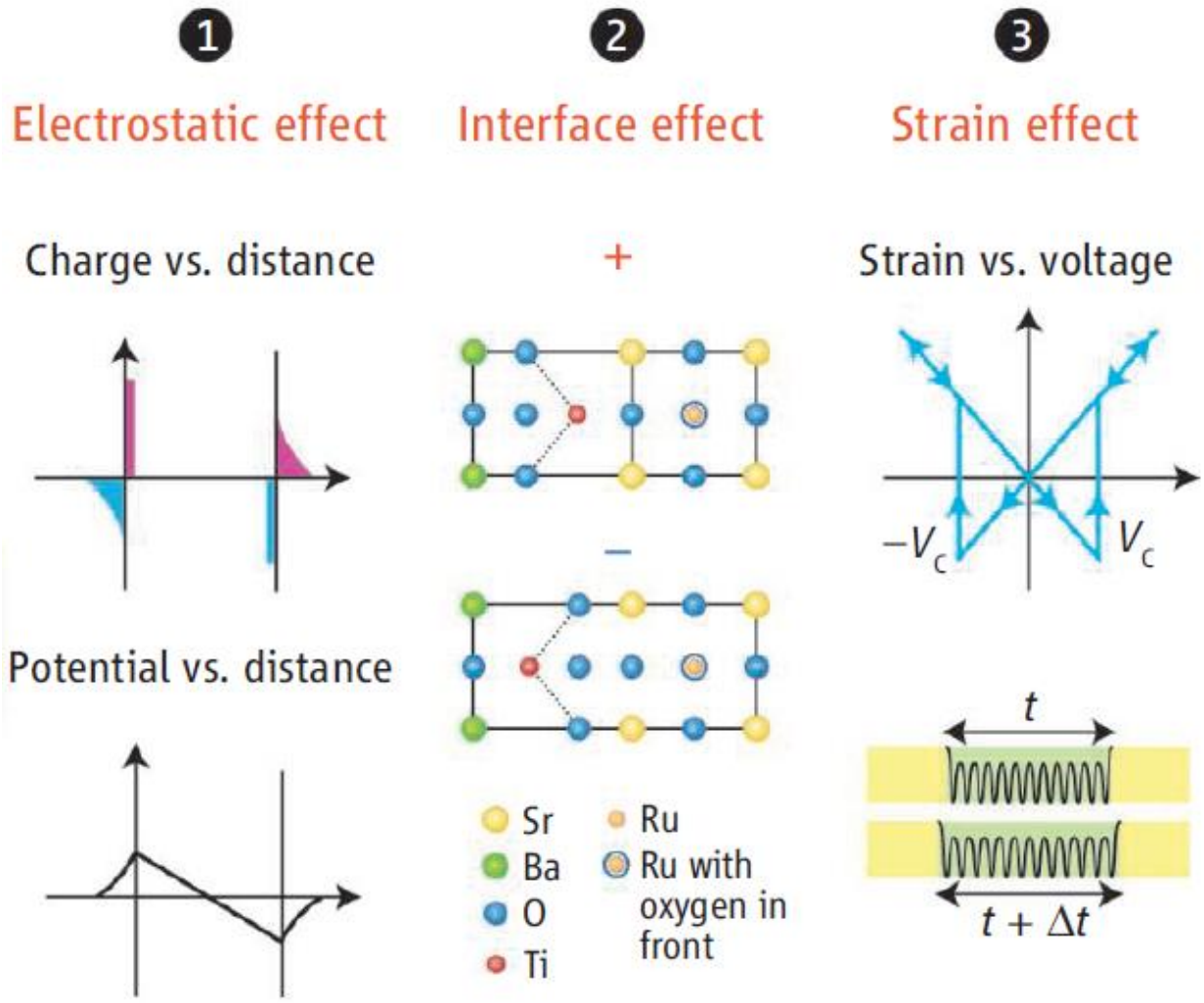

Figure 2.14 Three proposed origin of the TER effect in an FTJ. (1) Electrostatic effect, (2) Interface effect and (3) Strain effect, where t is the barrier thickness and Vc is coercive voltage. Adapted from ref. [106].

The second research focus is on the tuning the switching properties in plain FTJs, i.e. FTJs with non-magnetic electrodes. Early work [106] proposed three possible mechanisms for large TER in FTJs which is illustrated in **figure 2.14**. There are three possible origins: (i) electrostatic effect, space charge regions created at the electrode-barrier interfaces due to incomplete screening of polarization charge which lead to an asymmetric potential profile in FJTs with dissimilar electrodes. (ii) Interface effect, interface atoms being displaced in responds to polarization

direction change. (iii) Strain effect, where due to piezoelectric effect, the ferroelectric tunnel barrier thickness changes with the polarization reversal which lead to a difference in tunneling probability. Through careful theory simulation analysis [115], it is found out that the strain effect is minimal in normal FTJs due to the small coefficient of the piezoelectric constant and the thin thickness of the ferroelectric spacer. The interface effect needs more careful analysis of the local chemical environment at interfaces and it is less explored. The electrostatic effect on the switching properties is most widely studied. One of the characteristic study is on replacing one electrode of the FTJ from a metal to a semiconductor (structure of Pt/BTO/Nb:STO) [116], which set up a record on/off ratio of 10^4 at room temperature. The space charge region between BTO and Nb:STO are attributed to be main factor for the enhancement of on/off ratio. In another way, Yin *et al.*[117] reported that insertion of the metal-insulator transition manganite $La_{0.5}Ca_{0.5}MnO_3$ in $La_{0.7}Sr_{0.3}MnO_3/BaTiO_3/La_{0.5}Ca_{0.5}MnO_3/La_{0.7}Sr_{0.3}MnO_3$ junction leads to about two orders of magnitude of enhancement of the TER ratio. The common feature between the above two studies are the enhancement of on/off ratio by increasing the asymmetry between the two electrodes in an FTJ; the width of space charge region in ref. [116] and the conducting state of the $La_{0.5}Ca_{0.5}MnO_3$ in ref. [117] changes substantially from electron doping state to hole doping state which depending on the polarization direction. Asymmetrical electrodes are essentially asymmetrical interfaces. Since an FTJ itself consists of serials of interfaces, tuning interfaces is a natural approach to tackle this problem. Hence, the interface effect, especially the band offset at each interfaces with an FTJ, is carefully studied in BTO based FTJs. Relevant experimental results are discussed in chapter 8.

Chapter 3 Experimental Methods

This chapter focuses on the experimental methods. It covers various topics from substrate preparation, thin film growth, lithography process and characterization techniques include atomic force microscopy, x-ray diffraction, electronic properties measurements and magnetic properties measurements.

3.1 Sample Fabrication

3.1.1 Substrate Treatment

A good substrate is the basis for good epitaxial growth of thin films. Substrate surface preparation is the initial step for thin film deposition, for example, there is a very standard cleaning procedure for Silicon wafer. Surface cleaning is also very important for oxide thin film deposition. In fact, advance in the surface treatment technique is one of the milestones for high quality atomically abrupt oxide interface. In a normal perovskites like STO, the surface termination is usually a mixture of SrO and TiO_2 after the polishing the sliced wafer from single crystal ingot. The preparation of a specific terminated surface is highly desirable. The breakthrough was done by Kawasaki *et al.* [30], where only TiO_2 atomic layers are preserved by buffered NH_4F-HF solution etching. This technique is further improved by Koster *et al.* [118] by a three-step method, which is adopted here. Since STO is one of the most important substrate being used in my research projects, I will describe the substrate treatment method in details.

The three-step methods are: 1) ultrasonically clean the purchased STO (001) substrates with deionized water for 10 min. This step helps formation of $Sr(OH)_2$ surface layer due to the high reactivity of SrO with water at room temperature. 2) Dip the cleaned substrates into buffered

NH_4F-HF solution for 30 seconds. In this step, HF solution dissolves the $Sr(OH)_2$ surface layer, leaving only TiO_2 surface layer. The etching time is short to make sure that over-etching is minimal. Nitrogen blow dry the substrates. 3) Air anneal the dried substrates at 950 ℃ for 1.5 hours with ramping up and down rate of 5 and 3 ℃/min, respectively. The annealing process initiate the recrystallization process and recover a smooth surface of STO (100) surface. The effect of each step is explicitly demonstrated in **figure 3.1**. Atomic force microscope (AFM) images shows uniform and smooth pristine surface in the as received samples (**figure 3.1a**), after HF etching, atomic terraces are revealed but the terrace edges are not very sharp (**figure 3.1b**), air annealing process greatly improves the edges of the atomic terraces (**figure 3.1c**), makes it almost an ideal TiO_2 only terminated surface. A 3D image of one treated substrate is shown in **figure 3.1d**, where the atomic steps are much like staircases. One of the line profiling is shown in **figure 3.1e**, which quantitatively shows that the atomic terraces have the step size of 0.4 nm, which is the exact lattice constant of STO. Further from terrace width of 150 nm, we can calculate the miscut angle θ from equation 3.1

$$\theta = \arctan\frac{Height}{Width} = \arctan\left(\frac{0.4}{150}\right) = 0.15\,^{\circ}, \qquad \text{eq 3.1}$$

The miscut angle of 0.15 °is very consistent with that specified by the manufacturer.

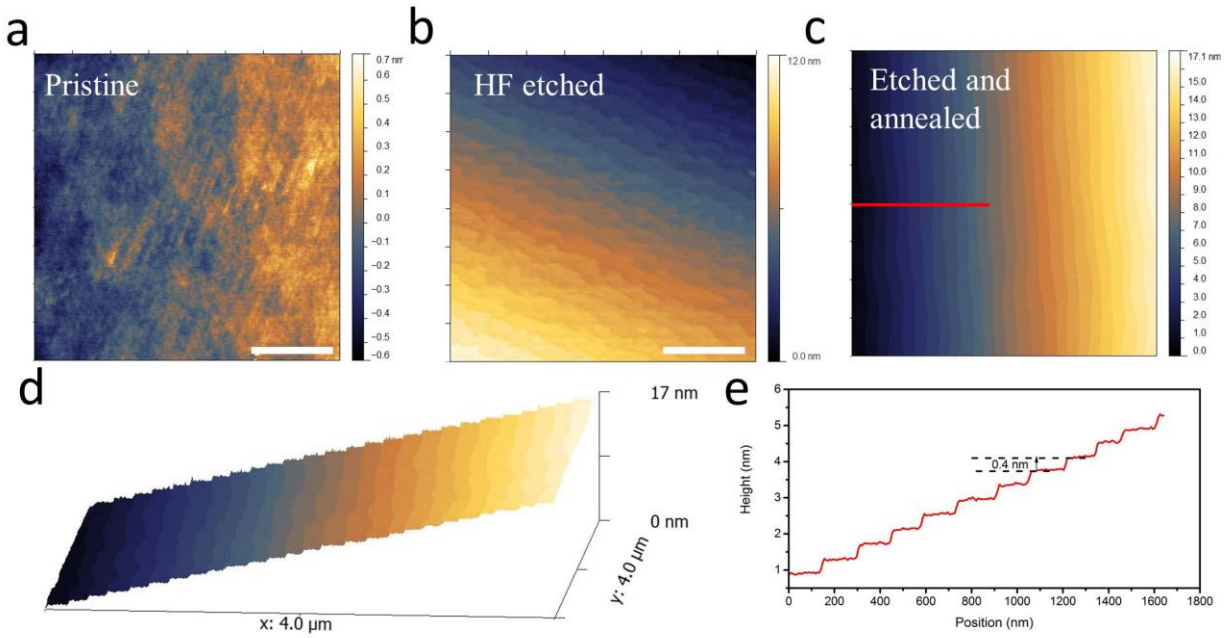

Figure 3.1 Surface treatment for STO (001) substrates. The surface morphology of STO substrates at different treatment stages: (a) as received, (b) buffered HF etched, (c) etched and air annealed. (d) 3D image of the etched and air annealed substrates (e) the etched substrates show a uniform 0.4 nm step height atomic terraces. The line profile corresponds to the red line section in (c). Scale bars in (a) and (b) are 1 µm in length.

Through this treatment, atomically flat, almost perfect TiO_2 terminated STO (001) surface has been achieved. Nb doped STO, with 0.5 wt % Nb doping concentration, can be treated in the same way due to the small atomic ratio of Nb (0.25 at.%) compared to Ti. Topography of one of the treated Nb:STO (001) substrates is shown in **figure 3.2**. The atomic terraces are much like that of STO substrates. Further, the phase image shows geometrical contrast at the step edges confirming that the Nb:STO (100) substrate is also single terminated.

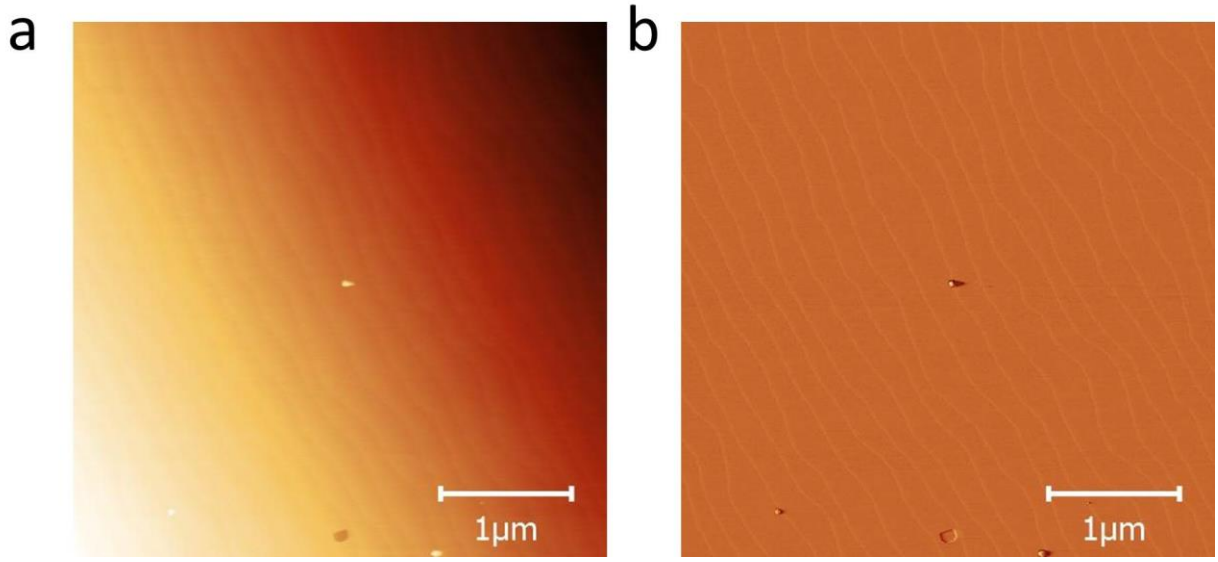

Figure 3.2 (a) Topography and (b) phase image of HF treated and annealed Nb:STO substrates with the same procedure adopted from STO substrate treatment methods.

Other substrates, where HF does not offer the differential etching ability of the A and B site atoms, usually are treated by thermal annealing as has been also reported by various studies. **Figure 3.3** shows the morphology of thermal treated $YAlO_3$ (YAO) (110) substrates and $NdGaO_3$ (NGO) (110). The annealing condition for YAO (110) substrate is 1050 ℃ for 5 hours, while NGO (110) is 1050 ℃ for 2.5 hours. For both substrates, the heating rate is 5 ℃/min and cooling rate is 3 ℃/min. More research works [31, 119, 120], from thermal annealing and wet chemistry methods, are devoted to develop new atomic controlled surfaces to build a full spectra of substrates for high quality oxide heterojunction growth.

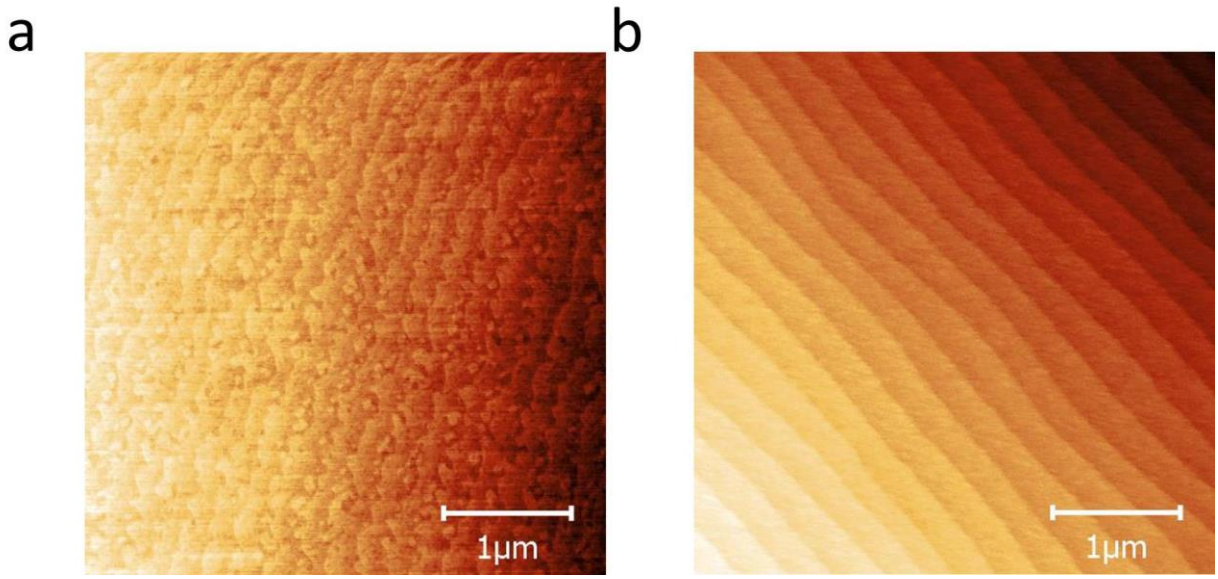

Figure 3.3 Morphologies of thermal annealed (a) YAlO3 (110) and (b) NdGaO3 (110) surfaces.

3.1.2 Pulsed Laser Deposition

Pulsed laser deposition (PLD) is the thin film growth technique I used for oxide thin film growth. It belongs to one type of physical vapor deposition method, similar to sputtering and molecular beam epitaxy. In history, pulsed laser deposition became a popular thin film deposition method since its capability of growing superior quality of thin films of high Tc superconductors compared other thin film growth techniques in the late 1980s [121].

Figure 3.4 shows a schematic setup of a PLD system. A PLD system can be divided into two parts, one part is optical system, which includes a pulsed laser generator and optical path leading to the PLD chamber. The other part is the PLD chamber with three primary components: 1) substrate holder with motors controlling substrate height and rotation, heater coil integrated with substrate holder 2) target holder with rotation and rastering motor and 3) molecular turbo pump, roughing pump and gas inlet and regulating valve. A high end PLD chamber has additional reflection high

energy electron diffraction (RHEED) chamber, for *in-situ* growth monitoring purpose, which is shown in **figure 3.4**.

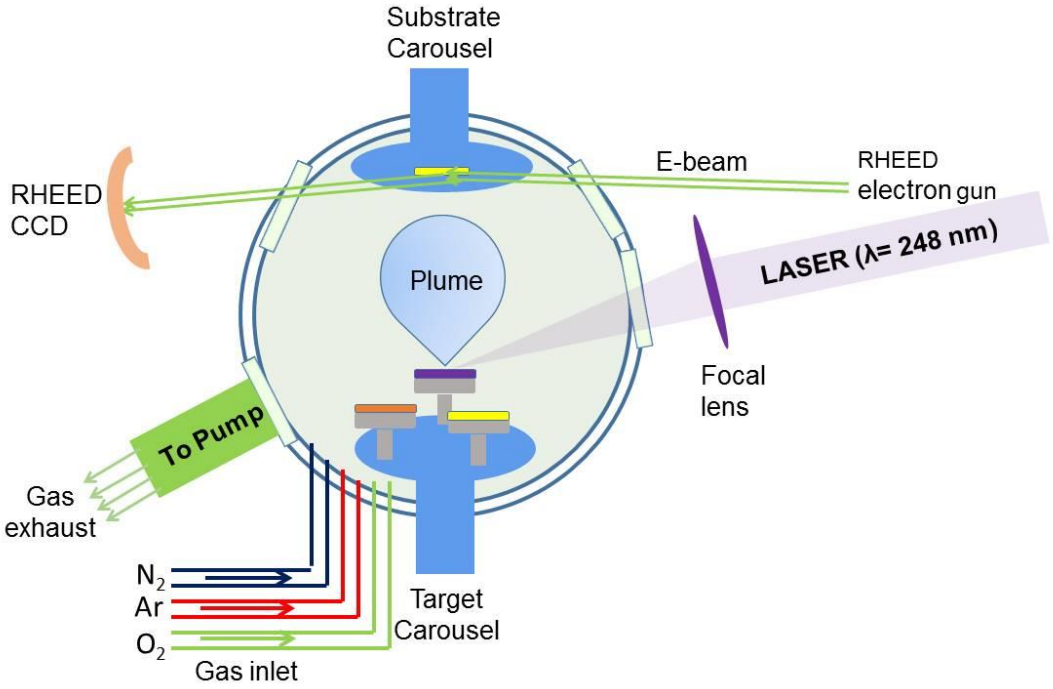

Figure 3.4 A schematic diagram of PLD set-up with RHEED. Key parts are labeled and pumping system is simplified.

Compared with other deposition methods, the most distinct feature of PLD is that it can preserve the stoichiometry of the target, especially for multicationic oxides. The other advantages include simple instrument setup, clean deposition process, availability of large gas pressure range (1 Torr to 10^{-7} Torr) and relatively fast growth rate. Considering above features, PLD is widely used in complex oxide thin film studies for research purpose. However, it has the limitation of small area deposition due to the laser plume is very directional. To solve this issue, beam scanners have been included in the modern PLD systems, where large area uniform thin film growth is achieved. For example, in our PLD system, thickness variation of the HfO_2 thin film over a 4-inch wafer is less than 4 %. It shows the potential of PLD for thin film deposition for industrial applications.

The basic process of PLD deposition is: 1) laser pulses are absorbed at the target surface, via a rapid thermal transfer process and target surface gets vaporized in the form of a plasma plume, which consists primarily atomic, diatomic and other neutral or charged low-mass species. 2) The plasma plume (see **Figure 3.5**) expands from the target surface towards the substrate. The energetic species get scattered by the background gas (e.g. O_2, N_2, and Ar) during the expansion process. 3) The plasma plume reaches substrate surface, where the atoms nucleate and grow thin film on the substrate.

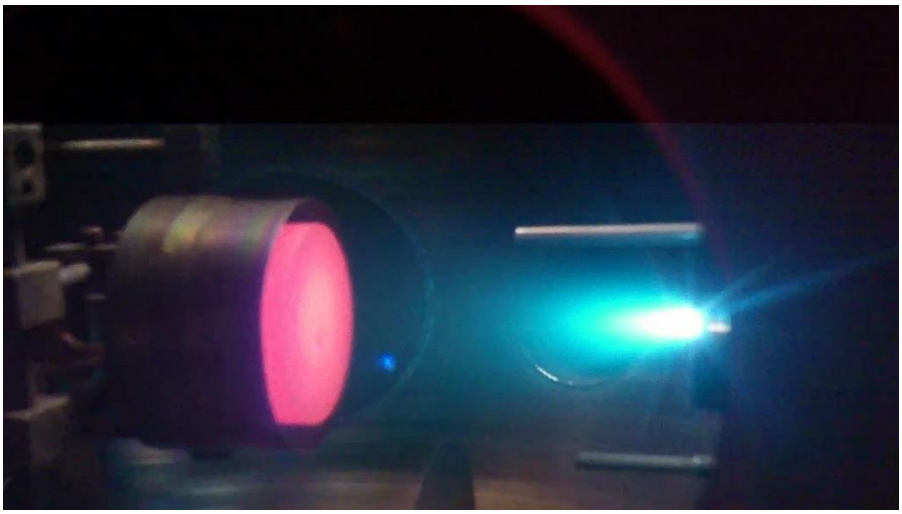

Figure 3.5 A photograph of plasma plume during PLD deposition. Bright blue colored plasma plume expands to the red hot substrates after each laser pulse. The plasma gets cooled during the expansion process towards to the heated substrate surface.

The thin film growth process in PLD process is far from equilibrium due to the high density of nucleation. The growth mode of the thin films is controlled by kinetics rather than thermal dynamic analysis. In simple kinetic studies, there are three types of growth modes, step-flow, layer-by-layer and multilayer growth (see **figure 3.6**). Step-flow growth occurs due to high surface mobility of the adatoms, it moves to step edges before any nucleation. Nucleation and growth starts from atomic steps (which are always present). Layer-by-layer growth occurs when the surface mobility

of adatoms is not as large as the step-flow case, but still large enough to diffuse across the length scale of atomic terrace width. Nucleation starts on the terrace plane, followed by growth and coalescence of nuclei. There is extensive interlayer mass transfer of adatoms so that there is no further nucleation before previous atomic layer is complete. Multilayer growth mode occurs at where interlayer mass transfer is very limited. Adatoms start to nucleate and grow at the absorption site and multiple atomic layers are grown simultaneously. From experimental perspective, deposition rate and substrate temperature are the most important parameters, multilayer growth at high deposition rate and low substrate temperature, while step-flow growth usually occurs at low deposition rate and high substrate temperature. Layer-by-layer growth fits in the intermediate conditions. The key difference among the three growth modes is the surface morphology evolution during the thin film growth process. Hence surface sensitive diffraction techniques (e.g. RHEED) are commonly used for in-situ growth monitoring. Section 3.1.3 elaborates more on RHEED.

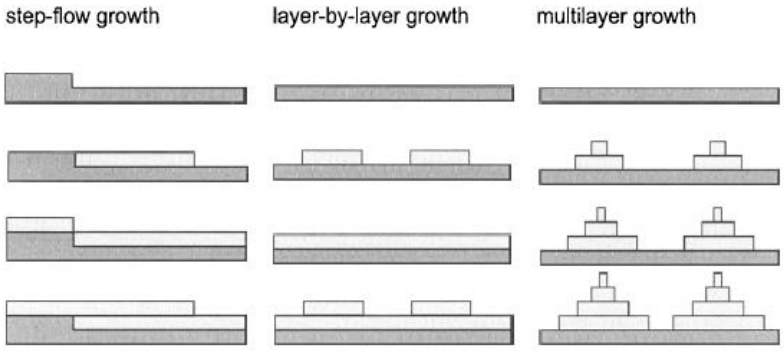

Figure 3.6 Different thin film growth modes. From top to bottom: surface coverage 0 uc, 0.5 uc, 1 uc and 1.5 uc, from Rosenfeld et al.[122].

In a typical PLD thin film process, there are several crucial parameters: 1) Quality of the target: high density target is preferred, to prevent large particles removed from target and deposited on the substrate. 2) Laser energy: an optimum range is desired and it is material specific. There is a

threshold energy density for effective plume creation but particles could be ejected from the target surface if the energy density is too high. 3) Substrate surface: atomically flat surfaces are preferred. 4) Substrate temperature: an optimum temperature is needed to provide the surface mobility of the arriving atoms to form a good crystal. 5) Background gas pressure: it can be used to tune the stoichiometry of the thin film (e.g. oxygen content) and also reduce damage of the grown thin film from the energetic plume by slowing down energetic species from plasma. The above five parameters determine the general procedures for optimization process of thin film growth by PLD. Starting with good targets and substrate, following efforts are devoted to find the optimized value for the laser energy, substrate temperature and background gas pressure.

The general process of a PLD deposition process include: loading substrate and target into the chamber, waiting for base pressure (e.g. 1×10^{-7} Torr), injecting O_2 gas to reach the targeted pressure (10^{-1} to 10^{-7} Torr range), heating up to the desired temperature (25 to 1050 ℃) (The actual substrate temperature is about 20% less than the heater temperature due to radiation heat loss), adjusting substrate position to get a good RHEED pattern, pre-ablating the target for a few minutes while target shutter is closed, ablating the target and monitor with RHEED software for the actual deposition and cooling down the sample and unloading the substrate and target from the chamber. The simple standard procedures make PLD an easy tool to be mastered by researchers.

3.1.3 RHEED

As mentioned in the above section, RHEED is usually used for *in-situ* monitoring purpose in a PLD set-up. **Figure 3.7** shows a schematic set-up for RHEED. Monoenergetic electron beam with typical energy of 10-50 keV strikes the sample surface with a glancing angle (less than 5 °). Due to the small glancing angle, RHEED is extremely surface sensitive with the sampling depth of only a few atomic layers. RHEED is very sensitive to the surface roughness down to monolayer

sensitivity. The glancing incident and reflection geometrical setup also does not block any vapor transfer process for the thin film growth. Great surface sensitivity and unique apparatus geometry make RHEED a perfect tool for *in-situ* characterization process for PLD.

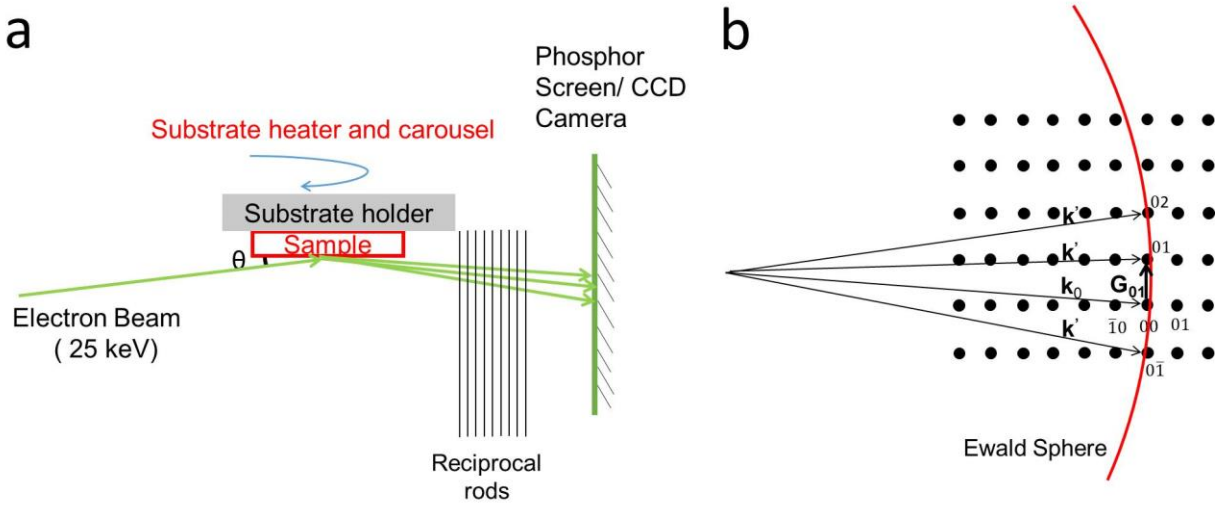

Figure 3.7 RHEED geometry and Ewald sphere construction. (a) A schematic illustration of a RHEED set-up. (b) Top view of the Ewald sphere construction to determine the diffraction conditions.

The operating principle of RHEED is based on electron diffraction for surface atoms. For diffraction analysis, Ewald sphere is constructed with the radius of $2\pi/\lambda$, where λ is the wavelength of the electron (~0.05- 0.1 Å). The reciprocal lattice for 2d thin films are infinitely thin rods perpendicular to the sample surface as shown in **figure 3.7a**. The construction of Ewald sphere is explicitly shown in **figure 3.7b** in top view direction. The diffraction condition is:

$$\mathbf{k}' - \mathbf{k}_0 = \mathbf{G}_{hk} \qquad \text{eq 3.2}$$

$\mathbf{k}'$and $\mathbf{k}_0$ a wave factor of scattered and incident beam, and $\mathbf{G}_{hk}$ is a reciprocal lattice vector with miller index of (hk). Since it is an elastic scattering process, $|\mathbf{k}'|=|\mathbf{k}_0|=2\pi/\lambda$. The reciprocal lattice points falling on the Ewald sphere surface get elastically scattered, like the reciprocal lattice points

(01), (02) and $(0\bar{1})$ (see **figure 3.7b**). It is worthy to note that the electron wavelength in RHEED is much smaller than the lattice constant of grown thin films, so that the Ewald sphere radius is much larger than the reciprocal lattice constants. As a result, Ewald sphere almost cuts the reciprocal lattice in a planar fashion, as demonstrated in **figure 3.7b**. Further, due to the low incident angle of the incident beam, low index lattice planes like (10) and (20) get diffracted strongly, which are commonly observed diffracted spots in RHEED.

Figure 3.8 shows an example RHEED pattern for treated STO (100) substrate at room temperature. Dashed semicircles are 0^{th} and 1^{st} order Laue Circles, which are resulted by the Ewald sphere with the (0k) and (1k) reciprocal lattice rods. On the 0^{th} Laue circle, the center brightest spot is called the specular spot (enclosed by white circle) because the scatter angle is the same as the incident angle, which is indexed as (00) spot. The specular point falls on the same reciprocal rod with the incident beam so it is invariant to sample rotation. It is very sensitive to surface roughness and hence its intensity is monitored during thin film growth process. The green lines in **figure 3.8** are Kikuchi lines, which are formed due to multiple scattering processes. The features on Kikuchi lines can be found somewhere else [123].

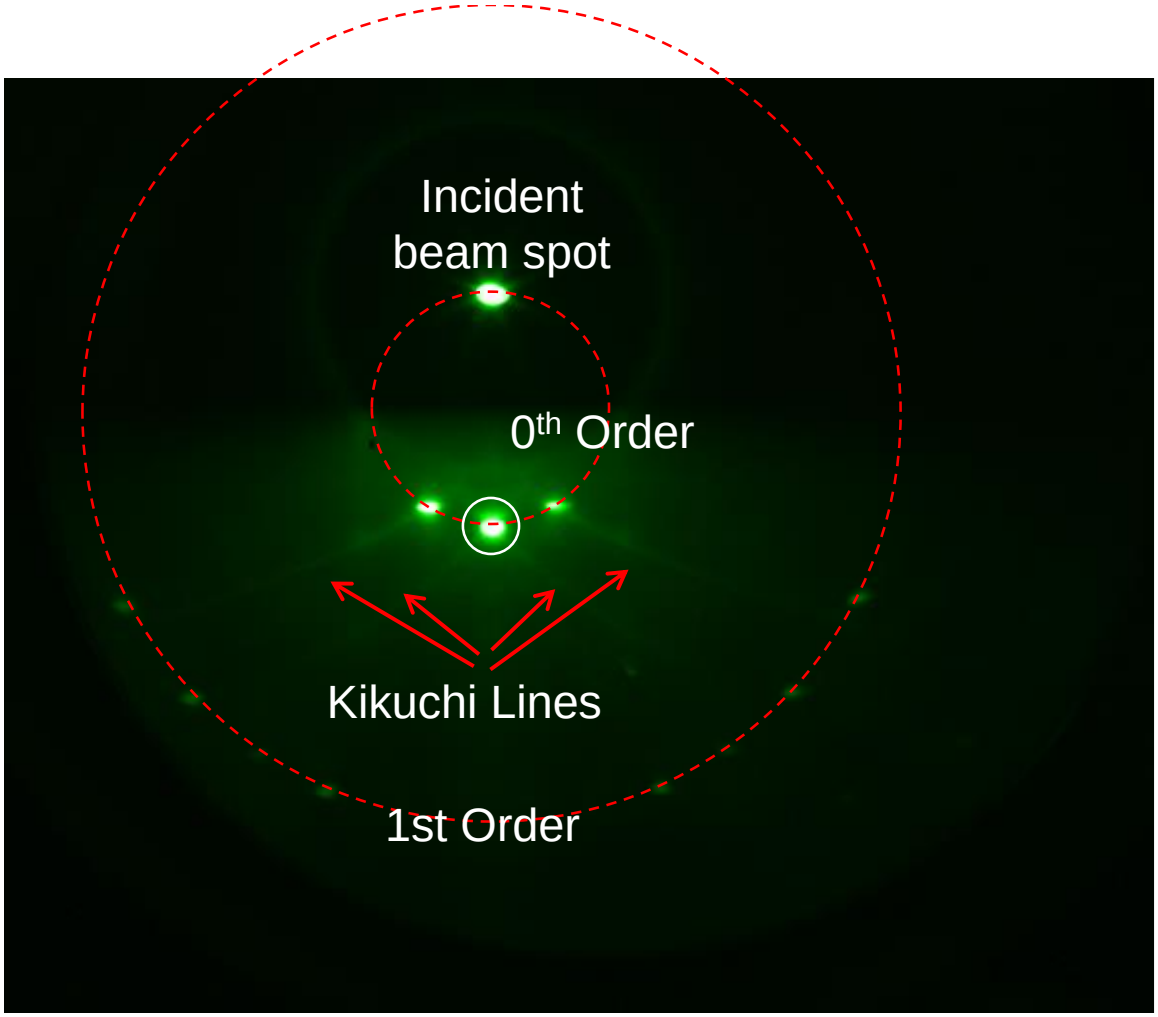

Figure 3.8 RHEED pattern for a treated STO substrate. Kikuchi lines are and 0 and 1st order Laue circles are labeled for clarity.

RHEED is a very versatile tool to monitor the thin film growth process. It can easily distinguish 2D and 3D growth mode, both from the RHEED pattern and the intensity oscillation of the specular spot. As shown in **figure 3.9**, RHEED pattern for layer-by-layer growth thin films is streaky after growth, and intensity of the specular spot oscillate with the growth time. On the other hand, dot matrix diffraction pattern are seen for island growth thin films. The intensity of the specular spot also decreases monotonically with growth time. Recall the discussion on the growth mode in section 3.1.2, the surface roughness change periodically for layer-by-layer growth but not for

island growth mode. Hence the RHEED intensity decreases monotonically for island growth mode. The emergent dot matrix is the results of electron diffraction of the island-shaped films, which creating more diffraction planes compared to the low roughness film in the layer-by-layer growth case. It is also found that the background intensity of island grown films are brighter than that of layer-by-layer growth films, which are attributed to the increasing extent of diffuse scattering because of the surface roughness. Furthermore, it is also quite often shown that thin film growth modes change from layer-by-layer mode to island mode after a certain thickness. The RHEED pattern is a superposition of the streaky lines and diffraction dot matrix.

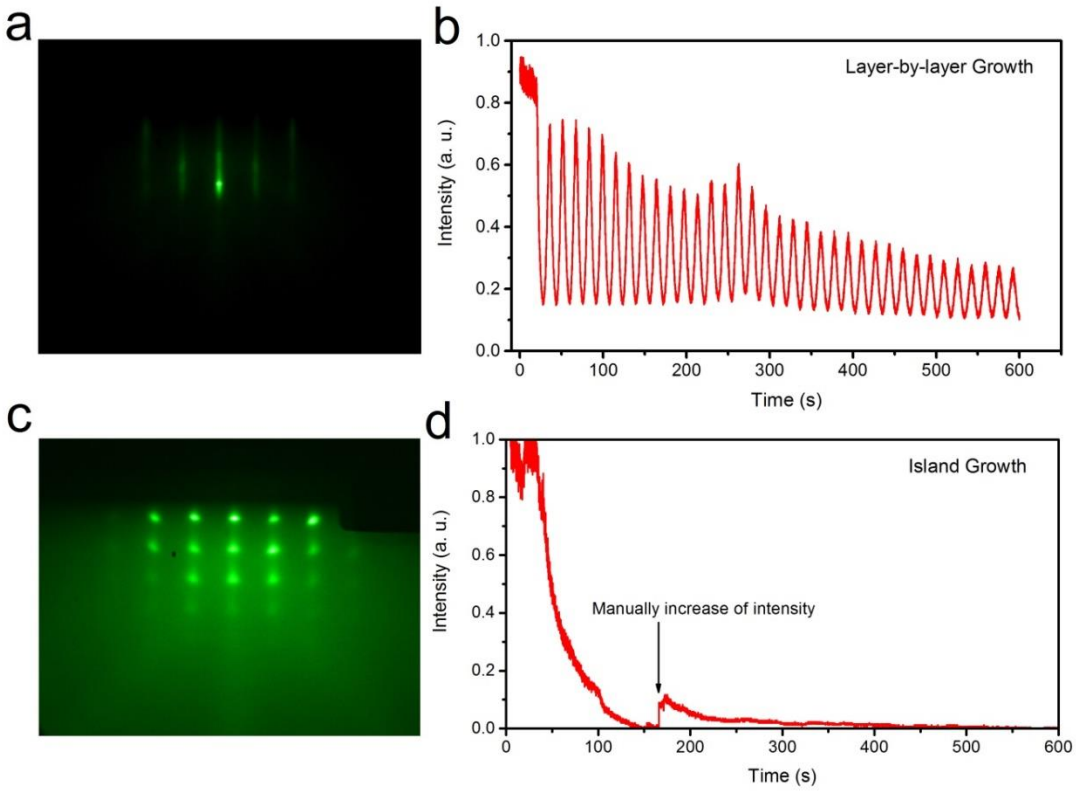

Figure 3.9 RHEED pattern and intensities for different growth modes. RHEED pattern for (a) layer-by-layer growth and (c) island growth modes. Growth time dependent RHEED intensity of the specular spot for (b) layer-by-layer growth and (d) island growth modes.

The oscillation of the RHEED intensity for layer-by-layer growth thin films offers an in-situ thickness monitor down to unit cell (usually a few Å). It is very beneficial for interface engineering, for example, superlattice periodicity with the precision of one unit cell. **Figure 3.10** shows an example of RHEED monitoring of LAO/STO superlattice deposition. Further, the atomic interface can be controlled more precisely with RHEED.

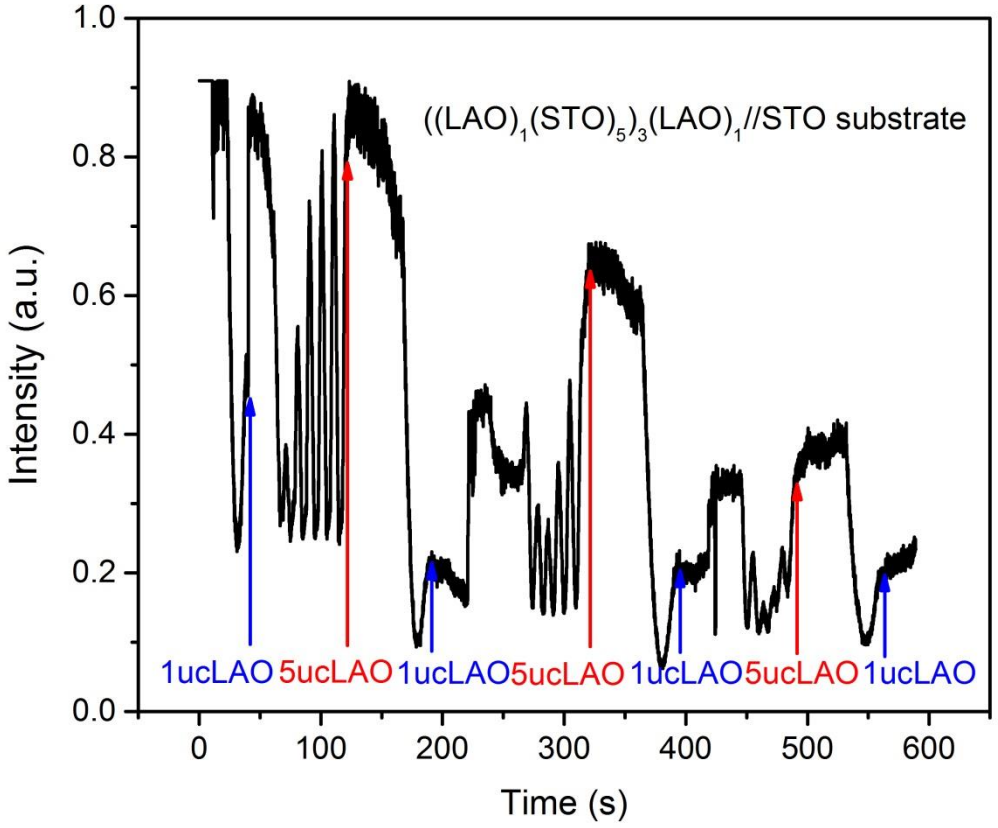

Figure 3.10 Growth time dependent RHEED intensity for LAO/STO controlled superlattice growth.

3.1.4 Sample Patterning

Patterning is a crucial step for device fabrication subsequent to thin film deposition. Photolithography and ion beam etching are commonly used tools to pattern a sample to the desired structure. **Figure 3.11** shows an example for the patterning process for FTJs fabrication. The key process is using a sacrificial AlN instead of photoresist to make the follow-up high temperature deposition possible. The starting point is deposition of uniformed BTO thin film (step a in **figure 3.11**). Followed by a spin coating, ultraviolet (uv) exposure and developing process of photoresist to get a positive image of the top electrode with photoresist (**figure 3.11b-c**). After that amorphous AlN is deposited followed by a lift-off process (step d-e), in which amorphous AlN forms a sacrificial mask with can withstand high temperature deposition. The top electrode $La_{0.67}Sr_{0.33}MnO_3$ deposited on BTO is crystalline and conducting while those on amorphous AlN are insulating (**figure 3.11f**). The final step (step g – j in figure 3.11) is another photolithography step to define the Pt electrode with photoresist mask. This process is easy because the Pt deposition is at room temperature.

This process is also applicable to define the conducting patterns of the LAO/STO interface. The only difference is the processes of the top electrode deposition steps are not necessary, instead, a wire bonding process is used to make the contacts for electrical properties measurements.

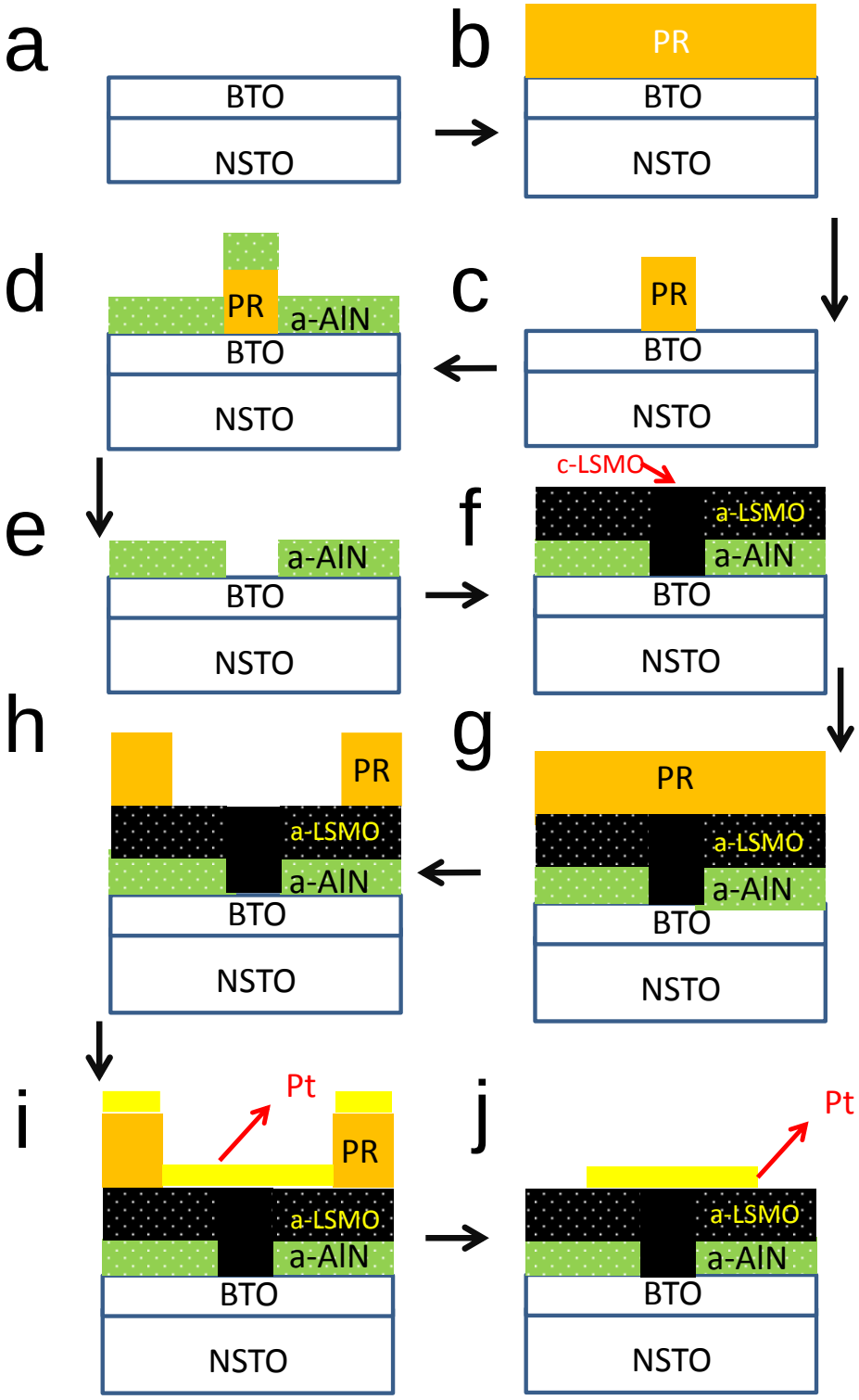

Figure 3.11 Patterning processes for Pt/LSMO/BTO//NSTO FTJs.

Besides this multistep process of patterning the samples, stencil lithography is also employed to pattern the thin films in a simple way. This approach is a single-step process as shown in **figure 3.12**. A mask is placed physically intact with the substrate and loaded to the substrate holder. During deposition, plume passes through the channels and other parts get blocked and the mask pattern is transferred into the deposited films. **Figure 3.13** shows one example the stencil masked film of $SrNbO_3$ on LAO (110) substrate, where the edges are well defined with the length features vary from a few hundred micrometer to sub-micrometer scale.

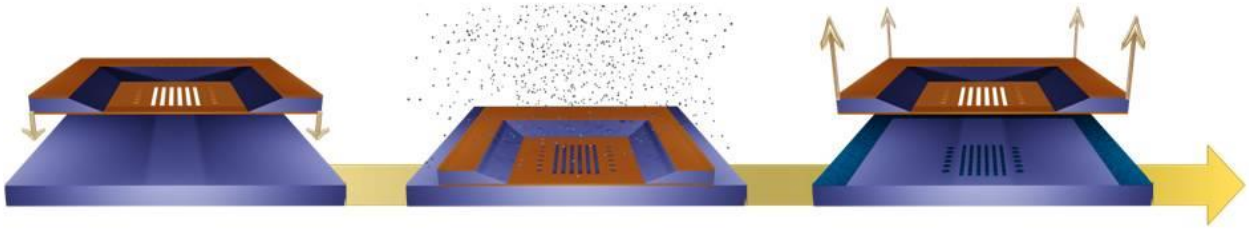

Figure 3.12 schematic steps for stencil lithography process. The brown patterned object is the stencil mask and the purple block underneath is the substrate. The grown film is bright purple in color.

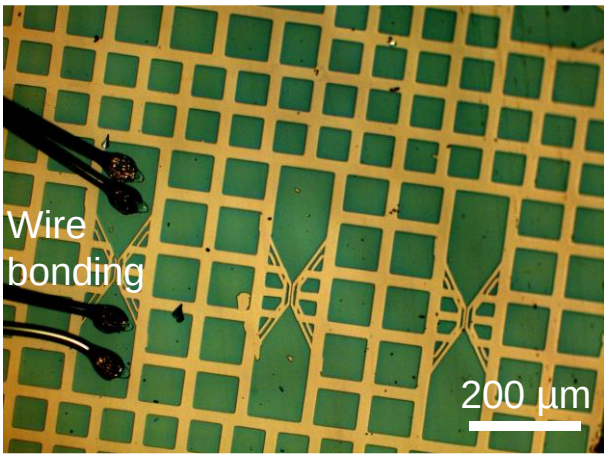

Figure 3.13 Patterned $SrNbO_3$ films deposited by stencil lithography with PLD. The structure features range from a few hundred micrometer (square blocks) to a few hundred nanometer (line pattern connecting blocks). It also shows the wire bonding can be applied on this patterned films to perform electrical measurements.

3.2 Sample Characterization

3.2.1 Atomic Force Microscopy

Atomic force microscopy (AFM) is one of a family of scanning probe microscopes which has grown steadily since the invention of the scanning tunneling microscope by Binning and Rohrer in the early eighties for which they received the Nobel Prize for Physics in 1986. AFM is one of the foremost tools for imaging, measuring and manipulating matter at the nanoscale. Unlike optical microscope and scanning electron microscope which using illuminated photons or electrons to visualize the sample, AFM uses the probe to "feel" the sample surface. It does not rely on the far field optics, so its resolution is not limited by the diffraction limit. In AFM, the interaction force between the probe and the surface includes the electrostatic repulsion, Van De Waals force, capillary force and others. The interaction force is highly dependent on the distance separation between the probe and the surface, as demonstrated in **figure 3.14a**. The height-force correlation provides the working principle of AFM. The scanning modes are also directly determined by the force-distance correlation. **Figure 3.14d** illustrates the force distance curve as the tip approach towards and retreat from the surface where the cantilever is modeled as the spring obeying the Hook's law. Capillary forces due to the absorbed moisture film on the sample surface causes the hysteresis loop of the force distance curve.

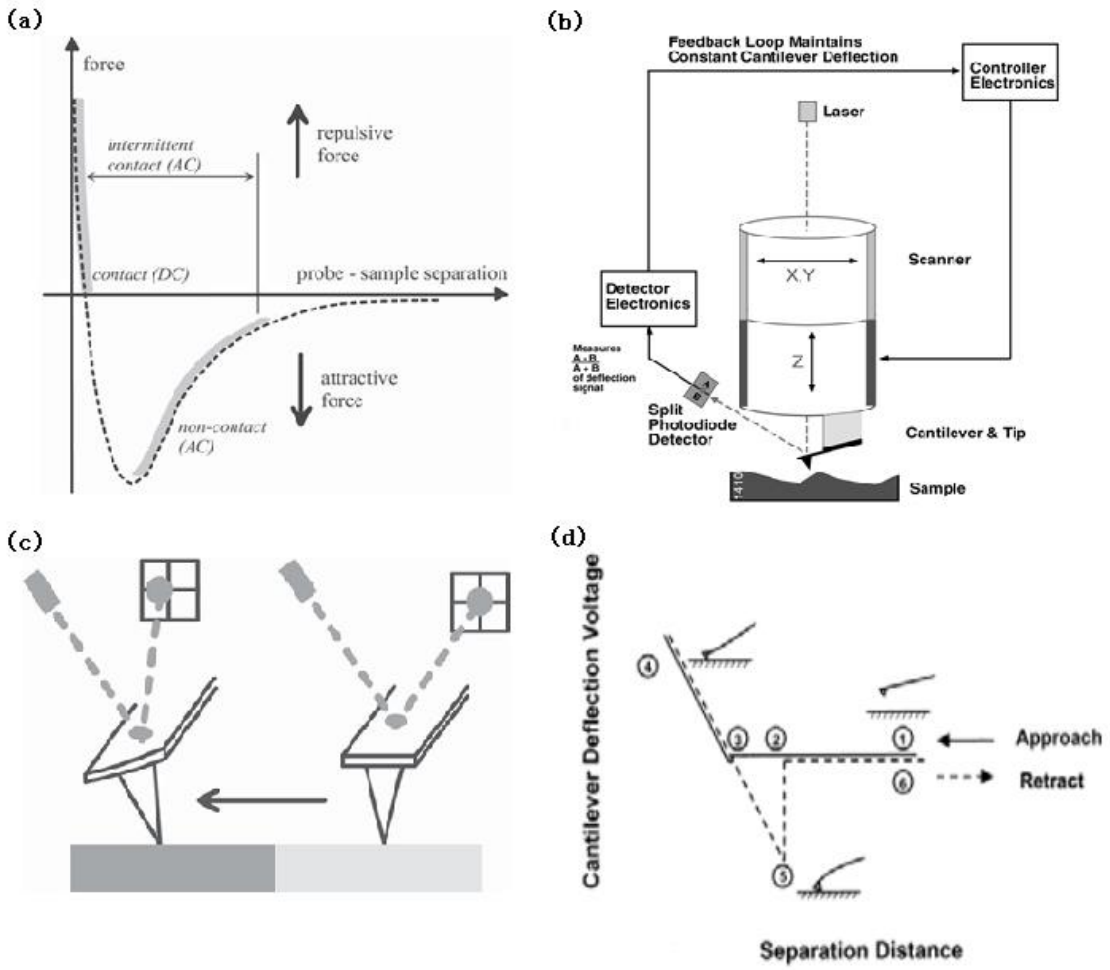

Figure 3.14 AFM set-up and principle. (a) The interactive force between the probe and the surface as a function of the distance separation. (b) Schematic diagram of the working system of the AFM. (c) Four-cell photodetector detection of cantilever deflection via laser beam. (d) The force distance curve when the probe approaches towards and retracts from the sample surface. Adapted from Vecco Inc. training note[1].

The apparatus of AFM is shown in **figure 3.14b**. It has four major components: (1) a cantilever with a sharp tip; (2) peizo-electric tube scanner which can scan across the sample with precise control the x, y and z position of the sample or tip; (3) data acquisition system where deflection data of the cantilever are monitored by a laser beam and 4-cell photodetector (see **figure 3.14c**);

[1] Scanning probe microscopy training notebook, retrieved 19 November 2015, from http://www.nanophys.kth.se/nanophys/facilities/nfl/afm/dim3100/Trng_Ntb_v3.0.pdf

(4) feedback control system, the feedback loop maintains either constant deflection (contact mode) or constant amplitude (tapping mode) by adjusting the z-position of the scanner. AFM tip detects the force information and causes a deflection in the cantilever, recorded by the four-cell photodetector through laser reflection system. In the next stage, the deflection information is transferred to the feedback control loop and is compared with the setting value of deflection or vibrating amplitude of cantilever. Finally, the z-position of the scanner changes to maintain the set signal. The recorded z-motion of the scanner gives the topographic information of the sample when the scanner scans through the entire sample surface.

AFM has three different scanning modes: contact mode, tapping mode and non-contact mode. In contact mode, the cantilever is maintained a constant deflection so that the surface tip separation is kept a constant in the repulsive force regime (**figure 3.14a**). The motion in z-direction of the scanner which is attached to tip/sample stage is used to plot out the topographic image when the scanner scans through the surface. Tapping/AC mode is a mode which the cantilever is driven to oscillate at or slightly below the resonant frequency. The oscillation amplitude is kept as constant by the feedback loop. The feedback loop needs to move the tip up or down to maintain the constant amplitude (typically 20-100nm) and hence a constant tip-sample interaction is maintained during imaging. In this way, the topographic images can be obtained. It lessens the sample damage and image distortion by friction comparing with contact mode. Hence, tapping mode is the common mode being used for our samples. All AFM images shown in section 3.1.1 are acquired by the tapping mode. Non-contact mode is similar to tapping mode but without any contact between the tip and sample. It is most suitable for the soft sample, like polymer and biological samples. AFM is a very versatile characterization tool when the AFM tip is changed functional materials. For

example, if the tip is coated with a magnetic material, it can be used to visualize the magnetic domain structure of a magnetic material. Conductive AFM (c-AFM) is another commonly used tool to map the sample conductivity. Moreover, c-AFM can be used to apply a local bias via the c-AFM tip to the sample to tune the properties of the oxide interfaces.

3.2.2 X-ray diffraction

X-ray diffraction (XRD) is one of the most important tools for structural characterization technique. X-rays are electromagnetic radiation with wavelength about 1 Å, which is comparable to most lattice constants (a few Å). The physical picture of x-ray diffraction is shown in **figure 3.15**. If the x-ray has an incident angle of θ relative to the crystal plane (hkl), the red highlighted path is the optical path difference between the two scatted x-ray beams.

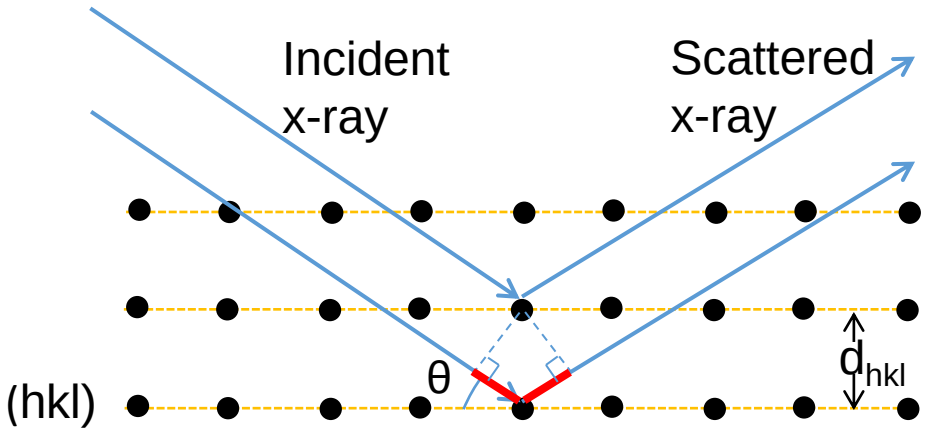

Figure 3.15 Schematics for XRD conditions.

Constructive interference occurs only when Bragg's law is fulfilled, which is described in eq 3.3.

$$n\lambda = 2d_{hkl}\sin(\theta) \qquad \text{eq 3.3}$$

Where λ is the wavelength (1.54106 Å for Cu Kα line) and n is an integral called diffraction order.

In equation 3.3, d_{hkl} is the spacing between the adjacent planes with miller indices is hkl. d_{hkl} is determined by the crystal system, the lattice constant and the miller indices. In the cubic system (which the perovskite oxides belong to) the relationship is shown in equation 3.3.

$$d_{hkl} = \frac{a}{\sqrt{h^2 + k^2 + l^2}} \qquad \text{eq 3.4}$$

In my studies, most of films are grown epitaxially on single crystal substrates. In this case, only the peaks with epitaxial relationship with substrate crystalline orientation are detected. For example, **figure 3.16a** shows that the epitaxial LMO films deposition on STO substrate XRD spectrum only has (001) and (002) peaks, which confirmed c-axis epitaxial relationship. For in-plane epitaxial relationship, both ω and φ scan must be carried out.

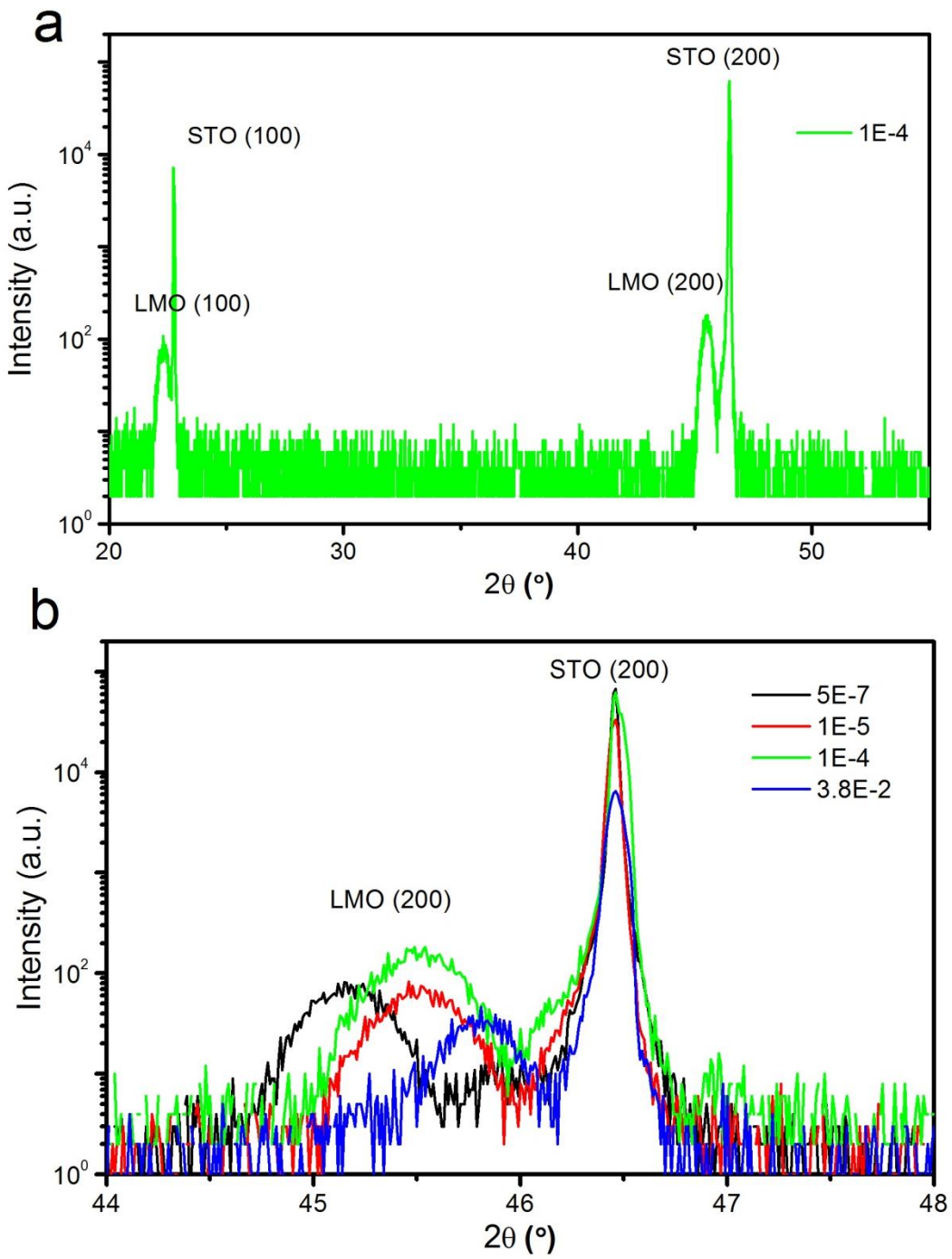

Figure 3.16 XRD of 20 nm epitaxial LMO thin film grown on STO (100) substrate. (a) Full XRD spectrum of LMO films deposited at 1×10^{-4} Torr. (b) Comparison of the XRD spectra near the (200) peak for different deposition pressures.

In **figure 3.16b**, there is a consistent shift of LMO (200) peak position towards lower angle when the deposition pressure for LMO decrease from 3.8×10^{-2} to 5×10^{-7} Torr. From Bragg's law, $d_{(200)}$ increases as the deposition pressure decrease. Further, according to equation 3.4, it could be deduced that the lattice constant increases with the decreasing in the oxygen pressure during deposition.

Except simple linear scan shown in **figure 3.16**, reciprocal space mapping is another important tool for epitaxial thin films analysis. Lattice constant and strain status of the film is easily visualized through the reciprocal mapping. Further studies will be discussed in the latter chapters.

3.2.3 Electrical properties measurement

Electrical transport measurements are one the essential tool to study electronic properties of the oxide interfaces. Electrical contacts are made through ultrasonic wire bonding method because the conducting channel is buried an insulating oxide layer (shown in **figure 3.17a**). For example, 2DEG in LAO/STO interface is covered by insulating LAO layer. If normal electrode contact is deposited through sputtering on LAO, then 2DEG cannot be probed. Wire bonding penetrates the LAO layer and directly contact with STO, where 2DEG resides, leading to characterization of the 2DEG in a simple way. Al wires are used as it normally forms an Ohmic contact on most oxides. When it bonds to the oxides, Al wires partially melt and form a secure connection with the sample, as is seen at the bonding point in **figure 3.13**.

Figure 3.17 b-d schematically describes the difference bonding patterns for electrical properties measurement on a uniform grown sample. Overall, four probe methods are used to eliminate the effect of the contact resistance. The current flows in from I^+ and flows out from I^-, where voltage is probed in between by V^+ and V^-.

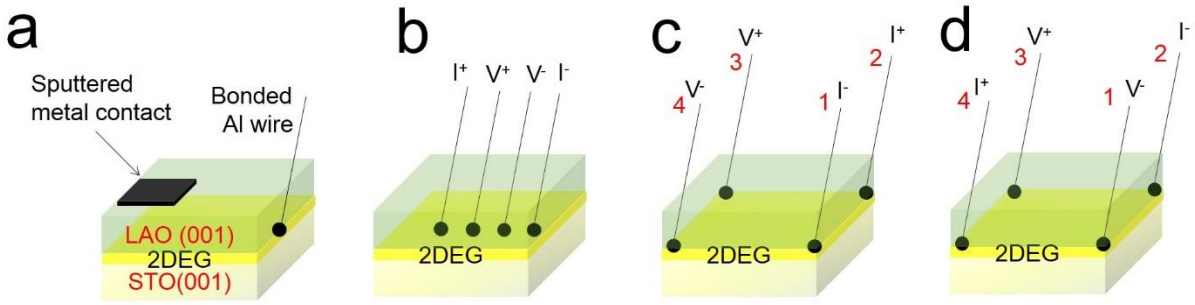

Figure 3.17 Wire bonding pattern on LAO/STO interface. (a) Difference between the wire bonding and surface sputtered metal contacts. (b) linear four probe bonding pattern (c) van der Pauw sheet resistance measurement bonding arrangement. (d) van der Pauw pattern for Hall effect measurement.

For linear four probe configuration (**figure 3.17b**) with spacing s between each electrode, the resistivity ρ can be calculated by equation 3.4

$\rho = 2\pi s \frac{V}{I}$, for bulk (semi-infinite sample volume), equation 3.5

,where ρ is resistivity, s is the distance between four probes, V is the voltage difference between voltage probes and I is the drive current. Semi-infinite sample means that sample thickness t is much larger than s.

For practical samples with finite sample volume, correction factors has to been included to be

$\rho = 2\pi s \frac{V}{I} C$, where C= (1/2ln2)*(t/s)^m, is the correction factor which dependence on value of t/s. In my research work, usually the conducting materials thickness is as thin as a few nanometers, which is much smaller than probe distance (t<< s). In this case, m=1 and hence C=(1/2ln2)*(t/s) and

$\rho = 2\pi s \frac{V}{I} \frac{1}{2ln2} \frac{t}{s} = \frac{\pi}{ln2} t \frac{V}{I} \cong 4.53 t \frac{V}{I}$, equation 3.6

Sheet resistance, Rs, is another quantity commonly referred to ultrathin conducting films, especially useful for the case that thickness of the conducting channel is not well defined.

$$R_s = \frac{\rho}{t} = 4.53\frac{V}{I}, \qquad \text{equation 3.7}$$

Equation 3.7 is commonly presented for conductive oxide interfaces, in the unit of Ω/□.

Besides linear four probe geometry for resistance measurement, van der Pauw geometry (**figure 3.17 b-d**) is another useful method to measure a two dimensional uniform conductive film. It has the advantage of simple bonding patterns, especially for the Hall effect. To improve the accuracy, symmetrical shaped samples are preferred. Most of our samples are in perfect squares, so we usually use van der Pauw method for electrical characterizations.

In van der Pauw geometry, current flows along one edge of sample and voltage difference is probed at the opposite side (**figure 3.17c**), which measures R_1. The same measurement is done with 90 ° ration of the square sample (i.e. probe 1: I^- , 2: I^+ , 3:V^+, 4: V^- change to 2: I^- , 3: I^+ , 4:V^+ 1: V^-, where 1,2,3 and 4 represents 4 corner connection point in **figure 3.17(c)**) which measures R_2. From R_1 and R_2, sheet resistance Rs can be calculated by

$$e^{-\pi\frac{R_1}{R_s}} + e^{-\pi\frac{R_2}{R_s}} = 1, \qquad \text{equation 3.8}$$

For a very uniform thin film, R_1 is almost as R_2, then $Rs=\frac{\pi}{ln2}R$, which is the same as equation 3.7. A more sophisticated analysis on the 4-probe measurement method can date back to FM Smits work in 1958 [2].

[2] F.M. Smits "Measurement of sheet resistivities with thefour-point probe" The Bell System Technical Journal 1958.

Rs measurement is usually measured as a function of temperature and magnetic field to study the electronic properties of a particular material. I-V measurements are very common for devices characterizations. Physical Properties Measurement System (PPMS) is the integrated system we use for this purpose. **Figure 3.18** shows a photo of our PPMS system. Its capability includes temperature range from 2 to 400 K, magnetic field 0- 9 T and 360 °of sample rotation which offers versatile functions for our measurements.

Figure 3.18 A photograph of our PPMS system mainly for electrical properties measurements.

R-T measurement is very useful to define the conductive behavior and phase transitions. Superconductor transition (**figure 3.19**) is one of the prominent examples showing the resistance drops to zero at the critical temperature.

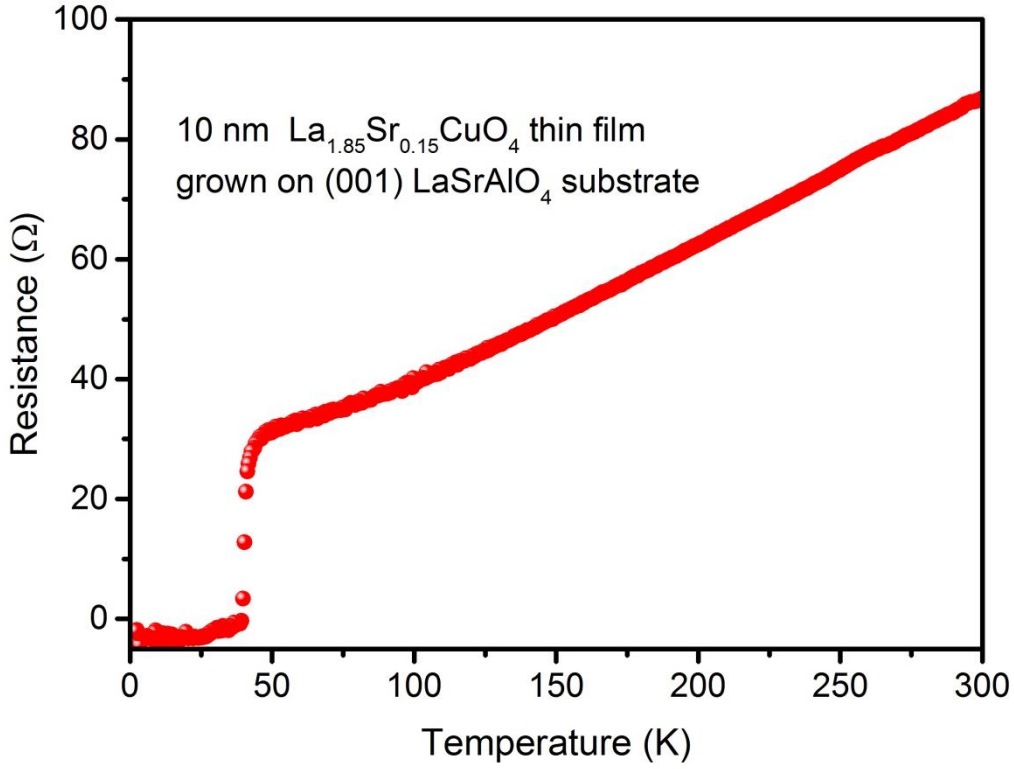

Figure 3.19 A typical R-T curve for 10 nm $La_{1.85}Sr_{0.15}CuO_4$ film grown on (001) $LaSrAlO_4$ substrates shows a T_c of ~ 40 K.

Hall measurement is the other important measurement to further analysis the transport properties of oxide interfaces. The Hall effect is originated from the Lorenz force of the mobile carriers under the influence of the magnetic field, as demonstrated and analyzed in **figure 3.20**. The equilibrium condition is that the Lorenz force is balanced by the electrostatic force caused by the transverse electric field, i.e.

$qvB=qV_H/W$ equation 3.9

, where q is the charge of the carrier, v is the drift velocity, B is the magnetic field strength, V_H is the Hall voltage and W is the sample width.

Further, a microscopic definition of current writes:

$I=qnv(Wt)$ equation 3.10

, where I is the current, q,v,W is defined before, n is the three dimensional carrier density and t is the sample thickness. Divide equation 3.8 by 3.9, it leads to:

$V_H/I=B/(qnt)=R_H$ equation 3.11

It shows that Hall resistance, R_H, is proportional to magnetic field with the slope of 1/(qnt).

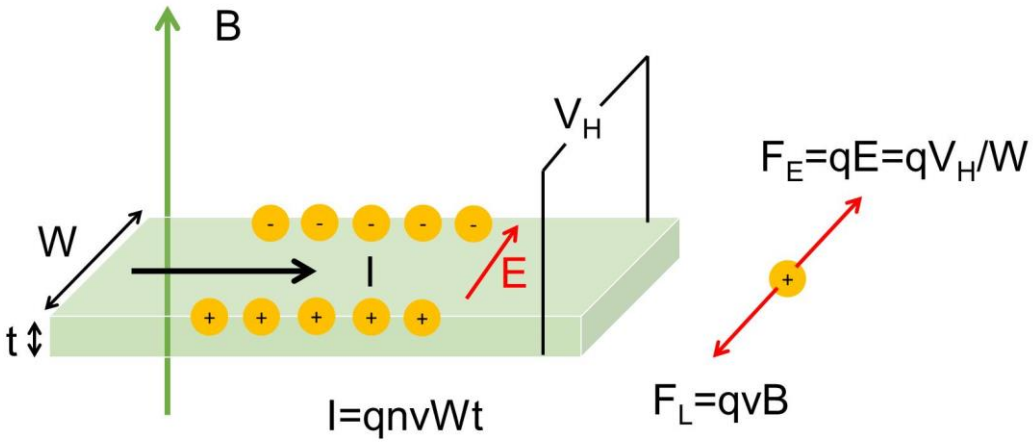

Figure 3.20 The Hall effect for current I pass through sample with width W and thickness of t under a perpendicular magnetic field B. Hall voltage is detected in the transverse direction.

Equation 3.10 confirms that the Hall measurement is a useful tool (1) to detect the carrier type (electrons or holes) in a conductive material (2) to quantitatively calculate the carrier density of the conductive system.

Furthermore, conductivity, σ is dependent on carrier density and mobility by:

$\sigma = 1/\rho = qn\mu$ equation 3.12

where q and n is defined before and μ is the carrier mobility which describes scattering frequencies of a physical system.

Recall equation 3.6, 3.10 and 3.11, mobility μ can be calculated as:

$\mu=1/(R_H * qnt)$ equation 3.13

In short, from Hall measurement, carrier concentration is measured through fitting of the experimental curves of R_H versus B. Carrier mobility μ is calculated from value of R_H and slope of the Hall curves. R_H vs T and Hall measurements for various temperatures all routinely carried out to find the trend of carrier density and mobility dependence on temperature in order to find out crucial parameters which dominate transport properties.

Magnetoresistance (MR) measurement is another important measurement for samples potentially responsive to magnetic field.

$MR(B) = [R(B)-R(0)]/R(0) \times 100\ \%$ equation 3.14

, where R(B) is the resistance with the magnetic field of B and R(0) is the resistance without magnetic field. Normally the resistance is four-probe linear geometry. For normal metals and semiconductors, MR is normally positive and quite small (less than a few present). The origin is Lorenz force cause electrons to spiral around magnetic field direction, which effectively increases the scattering probability which reduces the carrier mobility. For samples with certain magnetic orders, the interaction is much stronger and usually involves spin induced scattering events. In this case, angular magnetoresistance (AMR) is very important to differentiate different scattering mechanisms. In **figure 3.21**, it shows the sample geometry for AMR measurements. The AMR is plotted as a function of angle θ, the angle between the magnetic field and sample surface normal direction. The analysis of significance of change of anisotropy in AMR in LAO/STO interfaces will be discussed later in chapter 5.

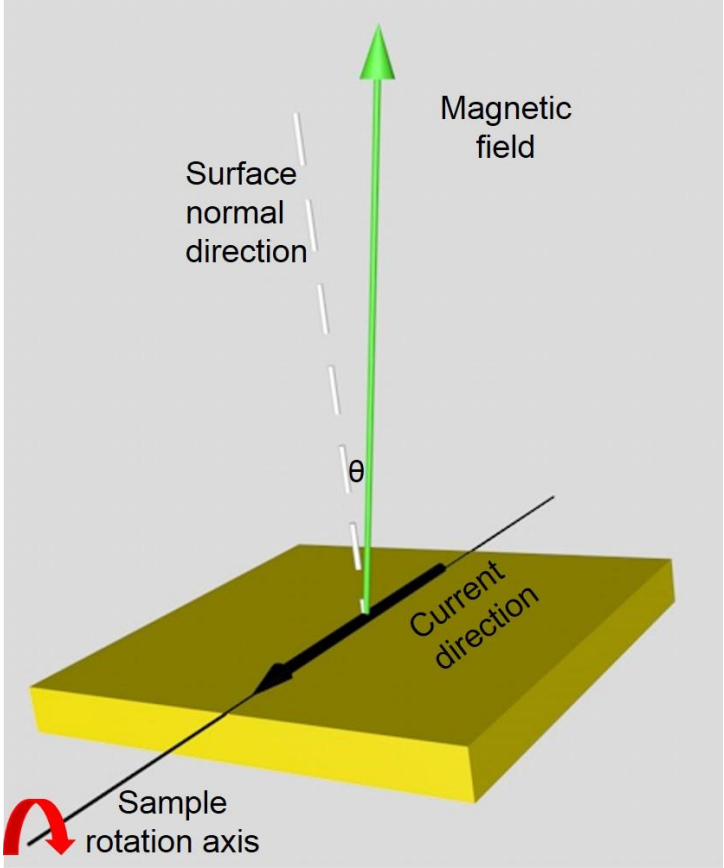

Figure 3.21 Schematic sample geometry for AMR measurement.

3.2.4 Magnetic properties measurement

Magnetic properties are another focus of my research topics. Generally, materials are divided into diamagnetic, paramagnetic, ferromagnetic, ferromagnetic and antiferromagnetic materials depending on the response of magnetic moment with the external magnetic field. The instrument to measure magnetic moment is called as magnetometer. Common magnetometers include: Inductive pickup coils/extraction magnetometer, Superconducting QUantum Interference Device (SQUID), Vibrating sample magnetometer (VSM), which are flux based magnetometers. Force based magnetometers include Faraday force magnetometer, alternating gradient force magnetometer and torque magnetometer and optical magnetometry (magneto-optic Kerr effect). JMD Coey wrote a comprehensive review on the principle, advantage and limitations of each

technique [124]. Among them, SQUID has the highest sensitivity (10^{-11} Am^2) but with the drawback of slow measurement speed. VSM-SQUID, building VSM setup with the SQUID pickup coil, is more popular magnetometer because it combines the advantages of high sensitivity of SQUID and fast measurement speed of VSM. Our lab has one VSM-SQUID setup by Quantum Design (see **figure 3.22**). It has the capability of temperature range of 2-400 K and magnetic field up to 7 T.

Figure 3.22 A photograph of our VSM-SQUID system for magnetic properties characterization.

There are two common measurements done to magnetic samples: magnetic moment temperature curves (m-T curve) and magnetic field dependent moment curve (m-H hysteresis). In m-T curves, there are two subtypes, one is called zero-field cooling curve (ZFC) and the other is called field cooling curve (FC). For normal m-T measurements, normally samples is cooled to low temperature at 0 field (ZFC) and then magnetic moment is measured from the heating up process. Similar

procedures are adopted for FC curve but there is a specific field applied during the cooling process. **Figure 3.23a** shows typical ZFC and FC curves for $La_{0.67}Sr_{0.33}MnO_3$. From the similarity of the FC and ZFC curve, it shows that the spontaneous magnetic moment exist in $La_{0.67}Sr_{0.33}MnO_3$ below the Curie temperature about 350 K. For m-H measurements, magnetic moment is measured after a specific magnetic field is applied at a fixed temperature. The typical m-H hysteresis loop is shown in **figure 3.23b**, from which important parameters including coercive field (H_c), saturation magnetic moment (Ms) and remanent magnetic moment (Mr) for a particular material are obtained.

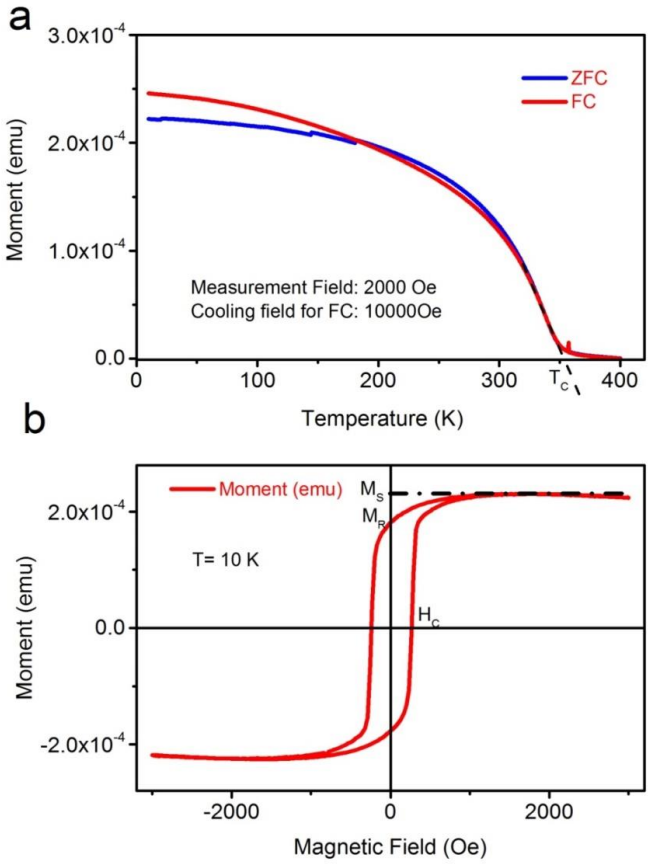

Figure 3.23 Magnetic properties of 20 nm $La_{0.67}Sr_{0.33}MnO_3$ grown on (100) STO substrate. (a) ZFC and FC curves in the temperature range of 10-400 K. (b) m-H hysteresis loop for 20 nm $La_{0.67}Sr_{0.33}MnO_3$ at 10 K.

To study magnetic properties in a microscopic picture, scanning SQUID microscopy (SSM) is the right tool to do it. The essential part of a SSM sensor is the superconducting pickup loop. The SSM we used has the inner size of our pickup loop is about $3 \times 5\ \mu m^2$. **Figure 3.24a** shows an optical image of the pickup loop. While scanning, the sensor is gently positioned in contact with the sample and the contact angle is ~ 10˚ (see **figure 3.24b**). A SSM image effectively maps out the stray field from the magnetic sample and provides the information of magnetic domain distribution in micrometer scale like a magnetic force microscopy (MFM). SSM offers the same function of magnetic force microscopy but with much better sensitivity (**figure 3.24c and d**). The detailed information will be discussed further in Chapter 7.

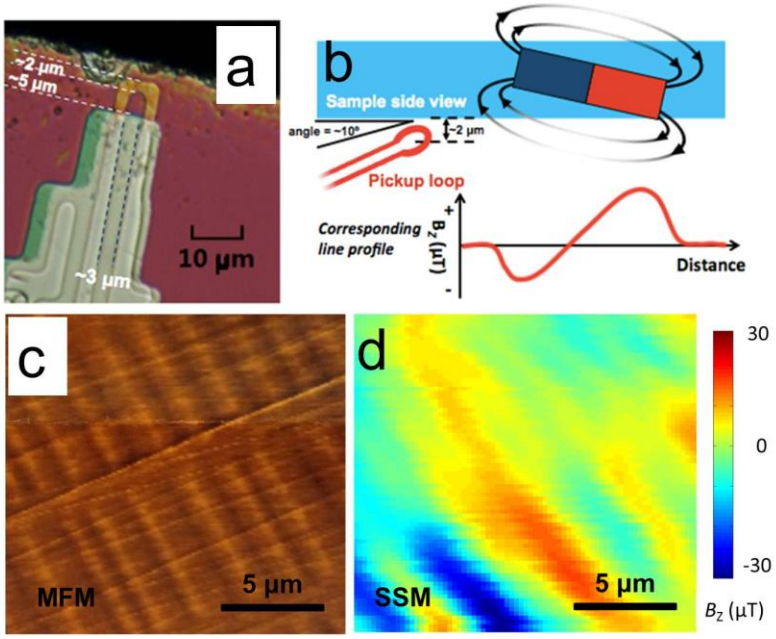

Figure 3.24 Schematic drawing of SSM principle. (a) Optical image of the pickup loop of SSM sensor. (b) Sketch of SSM configuration in scan position and magnetic field signal detected by SSM of a ferromagnetic domain. (c) Magnetic force microscopy and (d) scanning SQUID microscopy (SSM) images for a hard disk surface.

Chapter 4 Origin of the Two-Dimensional Electron Gas at LaAlO3/SrTiO3 Interfaces: The Role of Oxygen Vacancies and Electronic Reconstruction

Abstract

Despite the interesting phenomena observed in $LaAlO_3/SrTiO_3$ (LAO/STO) interface, debates over the origin of two-dimensional electron gas (2DEG) at the interface remains. The similar transport properties of the amorphous LAO/STO to the crystalline LAO/STO raise more controversy. Here, we tackled this problem by a systematic comparison oxygen annealing and LAO layer thickness manipulation (reducing thickness by argon milling and increasing thickness by deposition) effect on the transport behaviors in both amorphous and crystalline LAO/STO interfaces. We successfully distinguished electrons due to polarization catastrophe and oxygen vacancies by their thermal activation energy and found crystal quality really matters for polarization catastrophe induced carriers.

4.1 Controversy over origins of LAO/STO interface conductivity

As discussed in the chapter 2, 2DEG observed at LAO/STO interface triggered intensive research on this system. Metal-insulator transition, electric field effect, superconductivity and ferromagnetism are the interesting properties presented in this system. The capability of being patterned to nanoscale and possibility of integration with silicon industry show the promises of its applications in future oxide electronics. However, the origin of 2DEG is still debatable. The common three origins are polarization catastrophe induced electronic reconstruction, interface cationic (Ti/Al and/or La/Sr) intermixing and oxygen vacancies, illustrated in **figure 2.5** and **2.6** in chapter 2. In this chapter, we have focused on electronic reconstruction model and the oxygen vacancies model since the atomic intermixing is proved unlikely [72].

Recently, several experimental reports [125-128] on 2DEG created from amorphous oxide thin films deposited on STO substrates draw attention to reconsider the origin of 2DEG. In 2007, Shibuya *et al.* [125] reported metallic conductivity at interfaces between amorphous $CaHfO_3$ films and STO single crystal substrates, and they attributed the conductivity to the effect of plume bombardment of STO substrates during the PLD process. Later, Chen *et al.* [126] demonstrated metallic interfaces between STO substrates and various amorphous oxide overlayers, including LAO, STO and yittria-stablized zirconia thin films fabricated by PLD. The origin of the 2DEG in such amorphous/crystalline heterostructures was attributed to formation of oxygen vacancies at the surface of the STO. Moreover, metallic interfaces between Al-based amorphous oxides and STO substrates have also been realized by other less energetic deposition techniques such as atomic layer deposition [127] and electron beam evaporation [128]. The electronic properties of STO-based amorphous heterostructures [126, 127] are, to some extent, similar to those of crystalline LAO/STO heterostructures [48, 51], including the metallicity accompanied by the presence of Ti^{3+} ions and a sharp metal-insulator transition as a function of over layer thickness. These results call into question the polarization catastrophe model.

To differentiate the different origins of 2DEG, a comprehensive comparison between crystalline and amorphous $LaAlO_3/SrTiO_3$ in electrical and optical properties is investigated. Firstly, basic structural and photoluminescence properties are investigated in amorphous LAO/STO interfaces. Secondly, the LAO thickness dependent amorphous LAO/STO interface conductivity is investigated. After that, oxygen annealing was carried out for both conductive amorphous and crystalline interfaces to examine the effect of the oxygen vacancies. To evaluate the effect of polarization catastrophe effect, thicknesses of the crystalline and amorphous LAO layers are

modified by Ar milling and re-deposition process. Through these carefully designed experiments, we offer a much better understanding of the origins of 2DEG at LAO/STO interfaces.

4.2 Experimental Methods

Amorphous LAO films were deposited from a single crystal LAO target on untreated (100)-oriented STO substrates by PLD (KrF laser $\lambda = 248$ nm) at room temperature and different oxygen partial pressure. During deposition, the repetition rate of the laser was kept at 5 Hz and the fluence of laser energy was fixed at 1.3 J/cm^2. The deposition rate of amorphous LAO films was calibrated by transmission electron microscopy measurements. Crystalline LAO films were fabricated on TiO_2-terminated (100)-oriented STO substrates at 750 ℃ in 10^{-3} Torr oxygen partial pressure. The growth of crystalline LAO films was monitored *in-situ* by reflection high energy electron diffraction (RHEED). Electrical contacts onto 5×5 mm^2 samples (both amorphous and crystalline interfaces) were made with Al wires using wire bonding and electrical measurements were performed by a Quantum Design physical property measurement system from room temperature to 5 K. While the sheet resistance of all LAO/STO heterostructures was measured in the van der Pauw geometry, the magnetoresistance measurements were performed in the four-probe linear geometry.

The Ar-milling experiment was performed in an INTEL VAC Ion-Beam Milling System. Ar+ ions beam accelerated at 200 V at 4 ml/min and irradiated perpendicularly onto the samples mounted on a 6-inch Si wafer. The Ar pressure was kept as 6.4×10^{-2} Pa during milling. The milling rates of LAO layers were calibrated by an in situ secondary ion mass spectroscopy setup, which were 1.7 Å/s and 0.8 Å/s for amorphous and crystalline LAO layer, respectively.

4.3 Basic properties of amorphous LAO/STO interfaces.

4.3.1 Structural Properties of amorphous LAO/STO interfaces

Figure 4.1 shows the transmission electron microscopy images of a typical amorphous LAO/STO interface. In the zoom-in image, we could identify that there is some ordered state at the first LAO uc, and it gets more and more disordered with thicker films. It intuitively confirms that no long-range ordering is preserved for room temperature deposited LAO films, different from room temperature deposited crystalline γ-Al_2O_3 on STO [129].

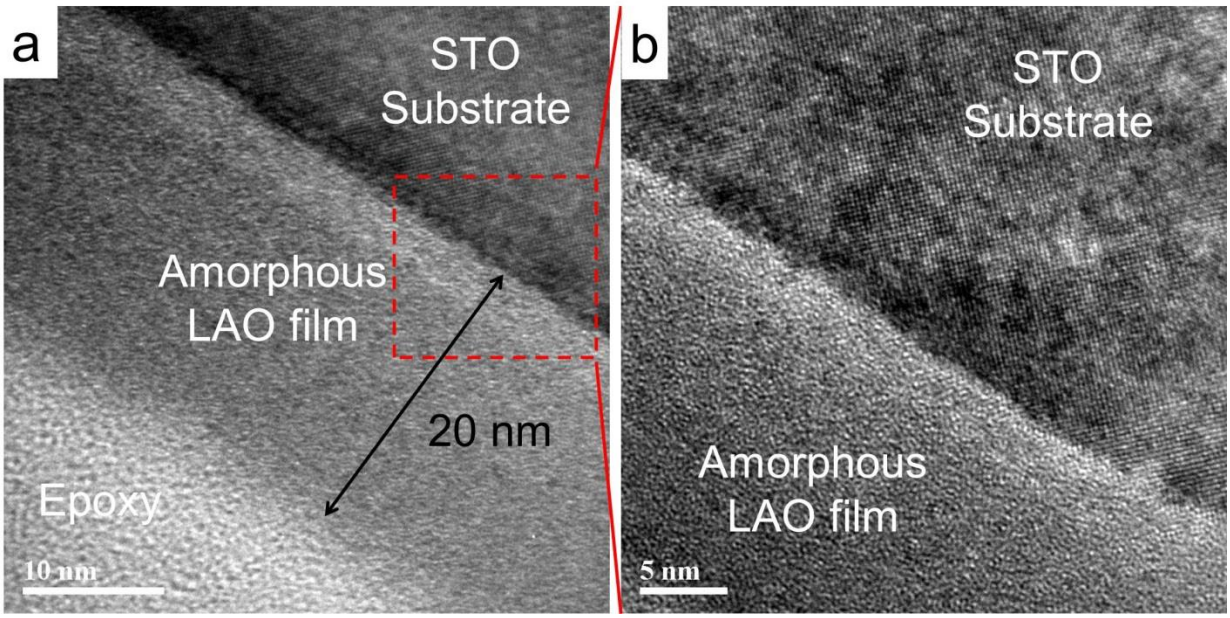

Figure 4.1 Transmission electron microscopy images of a LaAlO3 (LAO) film deposited on an untreated SrTiO3 (STO) substrate at room temperature and 10^{-6} Torr oxygen pressure. (b) the enlarged interface region of (a).

4.3.2 Photoluminescence of amorphous LAO/STO interface

To investigate the possible oxygen vacancies in the amorphous LAO/STO interface, photoluminescence (PL) spectra (excited by a 325 nm laser) of an as-received STO substrate and 20 nm amorphous LAO films deposited on STO substrates at different oxygen partial pressure ranging from 10^{-1} Torr to 10^{-6} Torr were investigated. As shown in **figure 4.2a**, PL intensity of the

as-received STO substrate is weak, but the characteristic PL peaks of oxygen vacancies at wavelengths ranging from 380 nm to 420 nm [43, 77, 81] in STO can still be seen. The different PL peaks probe the different oxygen vacancies defect levels and different occupancy probability between the defect levels, where further studies are needed to clarify the distribution of the defect levels within STO. However, it is worthy to do a rough estimation that 380 nm PL peak which corresponds to oxygen vacancies level is just 10 meV (380 nm equivalent to 3.26 eV transition and room temperature band gap of STO is 3.27 eV) below the STO conduction band. The PL intensity of amorphous LAO/STO heterostructures is enhanced by a factor of 5 to 9, relative to the as-received STO substrate, depending on oxygen partial pressure. Moreover, the multiple PL emission peaks are much more pronounced, and the PL intensity increases with decreasing oxygen partial pressure. Considering that 20 nm amorphous LAO films grown on Si substrates present no PL signal (**see figure 4.2b**) and the PL peaks from various defects in LAO bulk crystals appear only at ~600 nm and above [130], we are able to attribute the large enhancement of PL intensity between 350 nm and 475 nm in amorphous LAO/STO heterostructures to the creation of oxygen vacancies in the STO substrates near their interface during the deposition process. The PL spectra in **figure 4.2b** indicate the presence of oxygen vacancies in STO substrates, not in LAO layer or other substrates. Furthermore, amorphous LAO deposited on MgO and Al_2O_3 shows insulating properties. It was also found that the amorphous LAO has band gap greater than 5 eV (**figure 4.3**), similar to crystalline bulk LAO. Hence the conductivity cannot come from simple amorphous LAO films and it must be related to the interface properties.

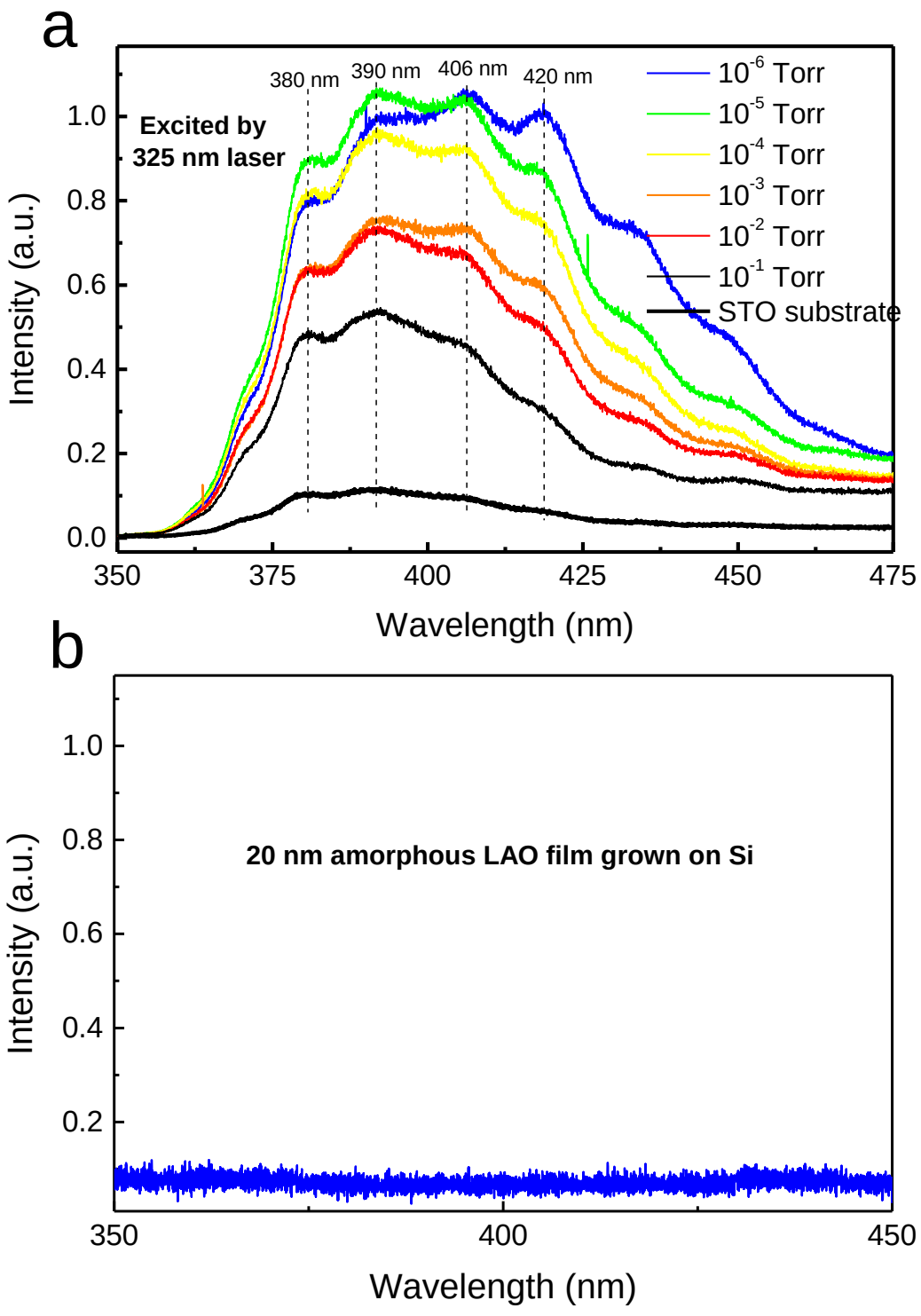

Figure 4.2 PL spectra for amorphous LAO/STO interfaces. (a) Deposition pressure dependent PL intensity for amorphous LAO/STO interface. (b) PL spectrum for 20 nm amorphous LAO on Si.

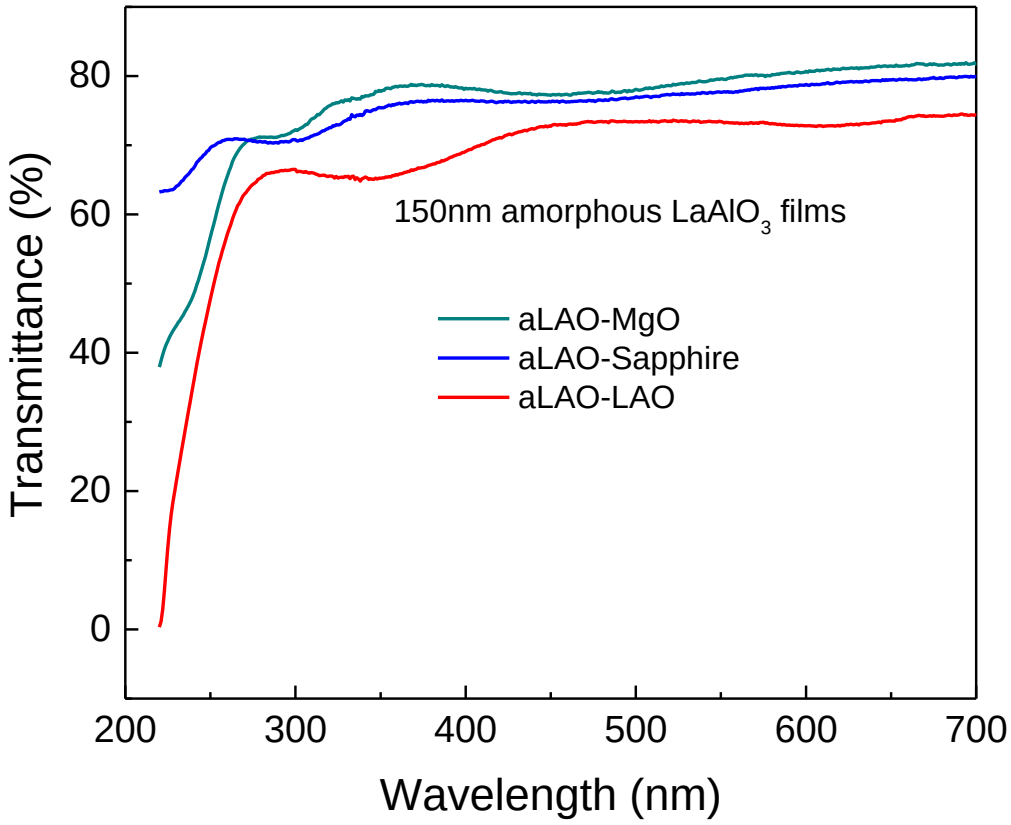

Figure 4.3 UV-vis spectra of 150 nm amorphous LAO layers grown on different substrates.

4.3.3 Transport properties of amorphous LAO/STO interface

Figure 4.4a shows the temperature-dependent sheet resistance (R_s-T) of the 20 nm amorphous LAO/STO heterostructures fabricated in different oxygen partial pressures from 10^{-3} Torr to 10^{-6} Torr. The heterostructures exhibit metallic behavior in the investigated temperature range (5- 300 K). The room temperature sheet resistance increases with oxygen partial pressure. The corresponding carrier density and mobility data are illustrated in **figure 4.3b**. The room-temperature carrier density of ~10^{14} cm^{-2} is comparable with that of unannealed crystalline LAO/STO heterostructures [51, 52], which were directly cooled down to room temperature in the deposition oxygen pressure after high temperature growth. Moreover, both the temperature-dependent carrier density (n_s-T) and mobility of such amorphous LAO/STO heterostructures are

similar to those of unannealed crystalline LAO/STO heterostructures [51, 52, 131], including the carrier freeze-out effect below ~100 K. We are therefore led to conclude that the conductivity emerging at the interface between amorphous LAO films and STO substrates originates largely from oxygen vacancies created in STO near the interface during film deposition.

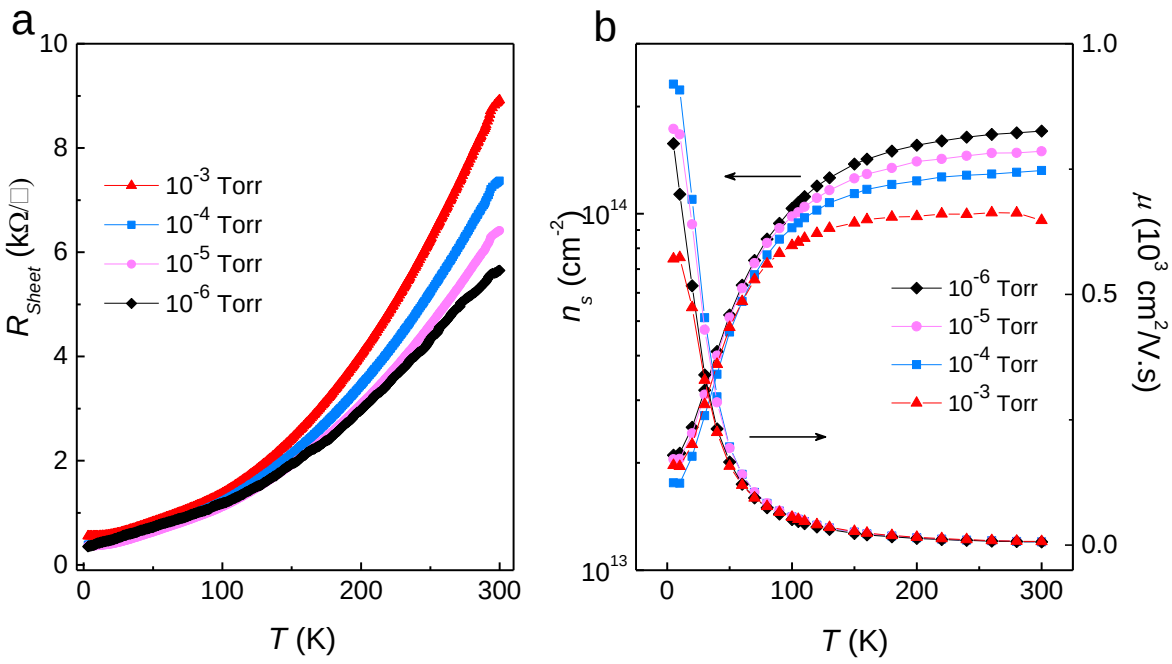

Figure 4.4 Electrical transport properties of amorphous LAO/STO heterostructures. (a) The temperature dependence of sheet resistance (R_s-T) and (b) sheet carrier density (n_s-T) and the corresponding mobility for 20 nm amorphous LAO/STO heterostructures fabricated at different oxygen pressures from 10^{-3} Torr to 10^{-6} Torr.

4.3.4 Critical thickness for metal-insulator transition of amorphous LAO/STO interfaces

The other interesting property worth studying is the minimum thickness for conducting amorphous LAO/STO interfaces. As known before, the previous reported critical thickness of 4 uc in crystalline LAO/STO is a strong evidence for polarization catastrophe resulted interface conductivity. Will the same thickness be present in amorphous interfaces? To answer this question, we systematically examined the LAO layer thickness dependence of sheet resistance for amorphous LAO/STO heterostructures, as a function of oxygen partial pressures. For samples

deposited at 10^{-1} Torr, no measurable conductivity was ever detected up to a 100 nm LAO layer thickness. As shown in **figure 4.5a**, for samples prepared at 10^{-2} Torr and lower pressure, a sharp drop by more than four orders of magnitude in sheet resistance occurs at a certain LAO layer thickness, which strongly depends on oxygen pressure (**figure 4.5b**). A similar sharp transition in resistance as a function of overlayer thickness was observed by Chen *et al.* [126] and Lee *et al.* [127]. However, the critical thickness for different pressures in our case is different from those reported by Chen *et al.* This is in contrast to the oxygen-annealed crystalline LAO/STO case, where the critical thickness of 4 unit cell (uc) [48] is robust over a large oxygen pressure range from 10^{-2} to 10^{-5} Torr and also can be repeated by a number of research groups.

We also found that the critical thickness in the amorphous case depends on some other factors such as laser energy and substrate-target distance which affects the kinetic process of redox reaction occurring at the top STO surfaces. For example, as we increased the substrate-target distance in our experimental setup by a factor of two and lowered the laser fluence from 1.3 J/cm^2 to 0.7 J/cm^2, the critical thickness at 10^{-3} Torr changed from 1.5 nm to 6 nm. Also, there is no pronounced difference in the sheet resistance when the amorphous heterostructures are fabricated on TiO_2-terminated or randomly-terminated STO substrates. This is drastically different from crystalline interfaces where conductivity only existed in interfaces based on TiO_2 terminated STO.

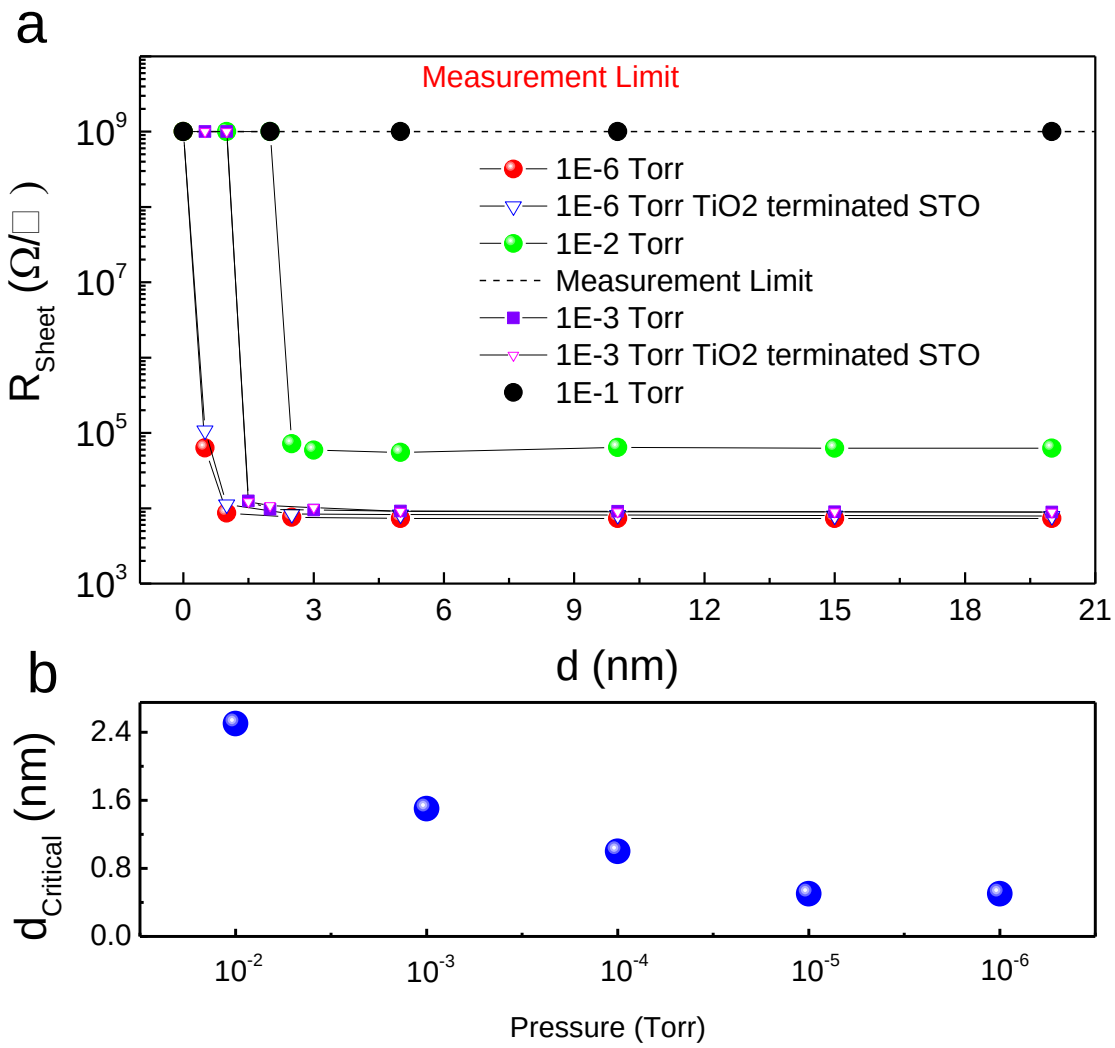

Figure 4.5 Critical thicknesses for appearance of conductivity in amorphous LAO/STO heterostructures. (a) Thickness dependence of room-temperature sheet resistance of amorphous LAO/STO heterostructures prepared at different oxygen pressures and on different STO substrates. Triangle symbols represent TiO_2-terminated STO substrates, while circles represent untreated STO substrates. (b) Critical thickness as a function of deposition oxygen pressure with other experimental conditions fixed.

There are three intriguing features in figure 4.5 worthy to explain: i) the sharp conductivity transition, ii) the oxygen pressure dependence of the critical thickness, and iii) the saturation of the sheet resistance with the amorphous overlayer thickness. When the overlayer is deposited,

chemically reactive species such as Al [132] have a strong propensity to attract oxygen ions from the surface of the STO, even at room temperature. The conductivity transition is explained by percolation of the electrons associated with the oxygen vacancies. The wave function of these electrons will be Bohr-like orbitals with radii of a few nm , resulting from the large dielectric constant of STO (ε_r = 300 at 300 K) and the large effective mass (~5m_e) [133]; the percolation carrier density is ~10^{13} cm^{-2} in one monolayer. The oxygen-depletion process from the STO surface will depend on how much reactive oxygen is available in the ambient atmosphere during deposition, thereby explaining why the critical thickness decreases at lower oxygen pressures. At the carrier densities required for percolation, the vacancy concentration at the STO surface is of the order of a few percent, a value that is already high and the further formation of vacancies will be inhibited [134]. This explains the saturation of the sheet resistance.

4.4 Comparison of properties of amorphous and crystalline LAO/STO interfaces.

4.4.1 Oxygen annealing effect on transport and PL properties

From section 4.3 studies, it shows the oxygen pressure is a prominent parameter in amorphous LAO/STO conducting properties, i.e. room temperature sheet resistance and critical thickness for the metal insulator transition. PL signal also semi-quantitatively shows that oxygen vacancy contents very dependent on deposition oxygen pressure. Previously literature also argues the effect of oxygen vacancies in crystalline interfaces. Oxygen annealing at elevated temperature is an efficient way to remove oxygen vacancies, hence the difference in transport properties before and after oxygen annealing would explicitly elaborate the role of oxygen vacancies in both types of interfaces.

Conductivity of all the amorphous LAO/STO heterostructures, regardless of deposition oxygen pressure, vanishes after a 1 h post-anneal at 600 ℃ in flowing oxygen (1 bar), as can be seen in **figure 4.6a**. At the same time, the PL intensity of all oxygen-annealed amorphous LAO/STO heterostructures decreases significantly and approaches the intensity of the as-received substrate (**figure 4.6b**). This confirms that oxygen vacancies in STO create the conductivity. In contrast, crystalline interfaces (10 uc LAO thickness) post-annealed under identical conditions remain conductive, although there is a decrease in carrier concentration and the room-temperature sheet resistance increases by a factor of seven (**figure 4.6c**); for example, an unannealed crystalline sample has a room temperature carrier density of 8.26×10^{13} cm^{-2}, which decreases to 1.62×10^{13} cm^{-2} after post-annealing. Moreover, the n_s-T of the unannealed crystalline LAO/STO sample shows carrier freeze-out below about 100 K, with n_s dropping to 1.90×10^{13} cm^{-2} at 5 K. In contrast, the carrier density of the post-annealed crystalline samples exhibits little temperature dependence, changing from 1.62×10^{13} cm^{-2} at 300 K to 1.38×10^{13} cm^{-2} at 5 K. Such post-annealing experiments are quite reproducible as shown in **figure 4.7**.

From the carrier freeze-out effect in unannealed crystalline LAO/STO samples, which also exists in oxygen-deficient STO films [81], an activation energy ϵ of 4.2 meV (fitted from $n_s \propto e^{-\epsilon/k_B T}$) is estimated, which is roughly consistent to the oxygen vacancy defect level position deduced from PL peaks. Following the same fitting method, the activation energy of carriers in oxygen-annealed crystalline LAO/STO samples is 0.5 meV, ~ eight times smaller than unannealed samples. The huge difference in the activation energy indicates that there are two contributions for 2DEGs for unannealed crystalline interfaces. Oxygen vacancies induced carriers only contribute to conductivity when temperature is larger than ~50 K (estimated from the $n_s - T$ curve) while the other source starts to contribute for temperature as low as 5 K.

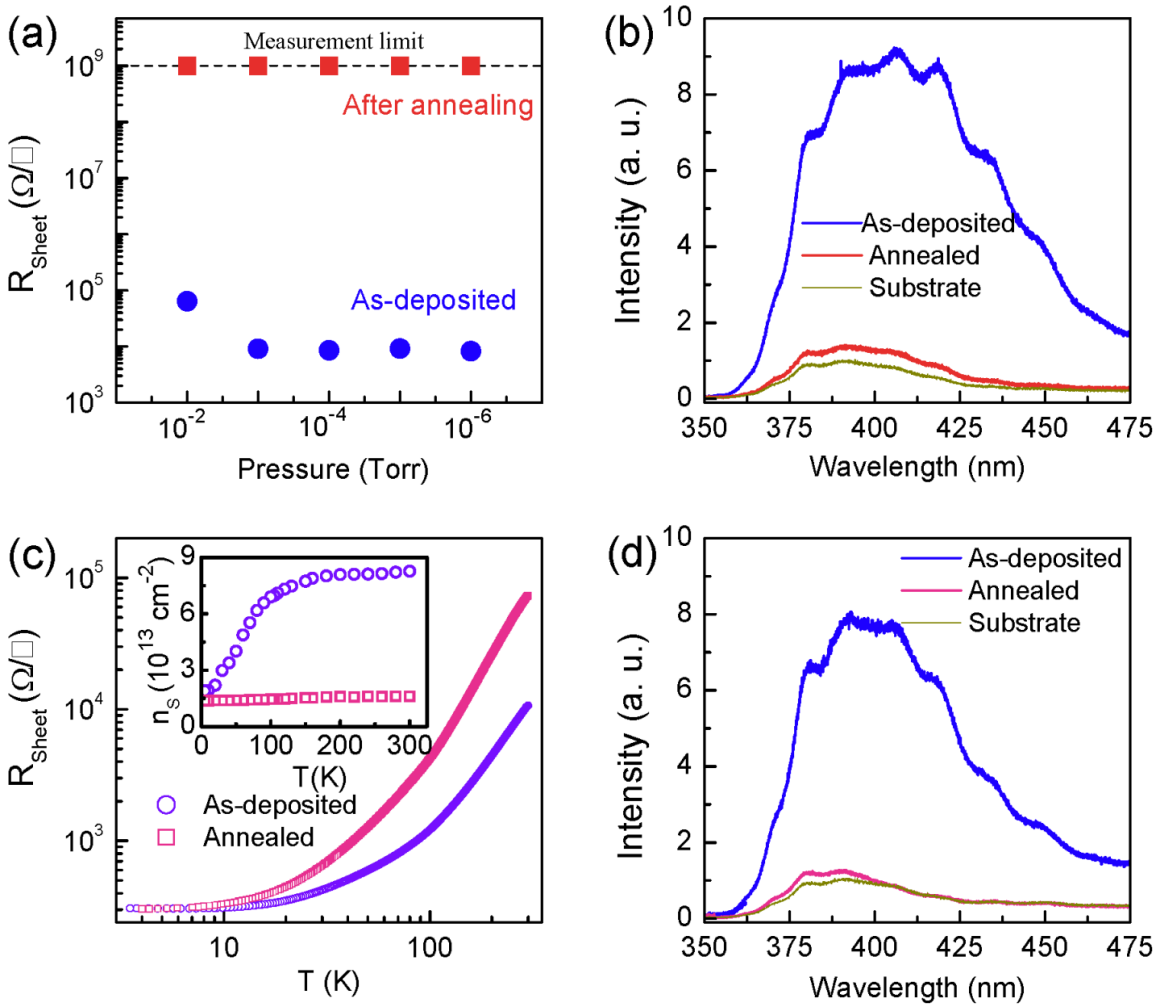

Figure 4.6 Oxygen-annealing effect. (a) Room-temperature sheet resistance of 20 nm amorphous LAO/STO heterostructures prepared at different oxygen pressures before and after oxygen-annealing in 1 bar of oxygen gas flow at 600 °C for 1 h. (b) PL intensity of the 20 nm amorphous LAO/STO heterostructures fabricated at 10-6 Torr before and after oxygen-annealing. (c) Rs-T, (inset) ns-T and (d) PL spectra of a 10 unit cell (uc) crystalline LAO/STO heterostructure prepared at 10^{-3} Torr and 750 °C before and after oxygen-annealing in 1 bar of oxygen gas flow at 600 °C for 1 h.

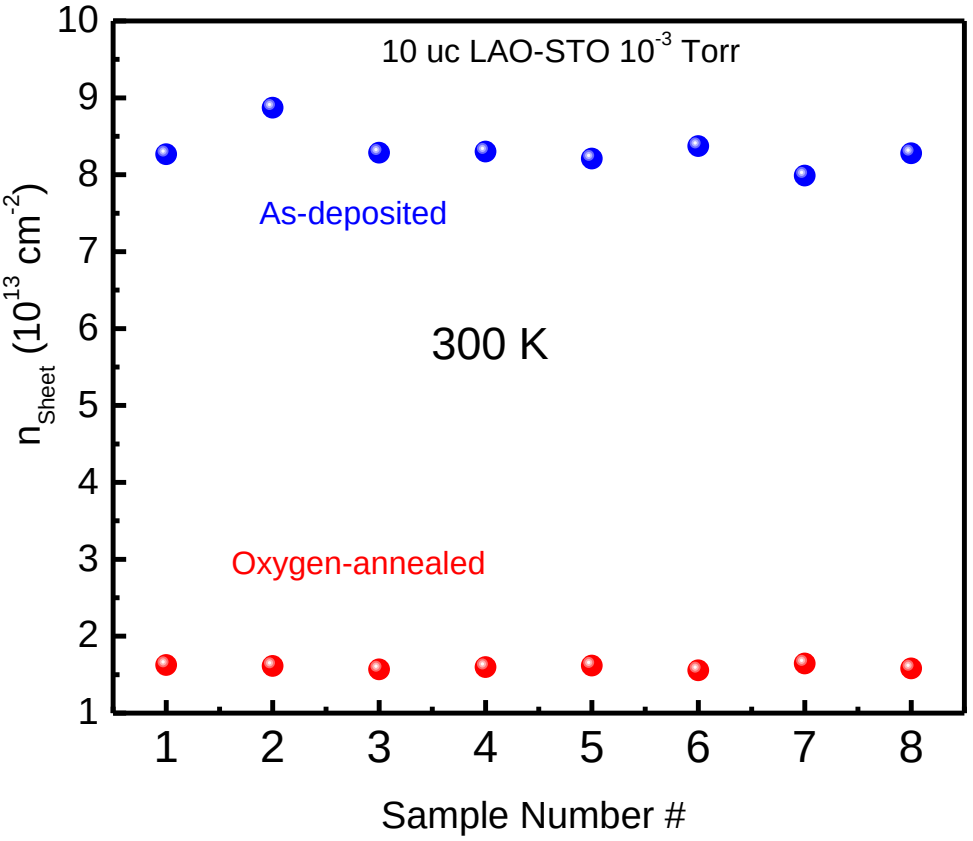

Figure 4.7 the change of the room temperature carrier density upon the effect of oxygen annealing process for 10 crystalline LAO/STO samples. All samples show that the carrier density decrease from 8×10^{13} to 1.6×10^{13} cm^{-2} after the oxygen annealing process.

On the other hand, PL intensity was also recorded for crystalline interfaces before and after the oxygen annealing process with the substrate as a reference sample. As shown in **figure 4.6d**, the PL intensity falls back to the substrate level, much similar to the effect of post-annealing on the PL signal of amorphous samples (**see figure 4.6b**). Hence we conclude that oxygen vacancies are also generated in the crystalline interface fabrication process, and the oxygen annealing process is an efficient way to remove oxygen vacancies.

Based on above analysis, it could be concluded that oxygen vacancies contribute substantially to the conductivity in both amorphous and unannealed crystalline LAO/STO heterostructures. Specifically, for amorphous LAO/STO samples, the existence of oxygen vacancies in STO substrates is the principal origin of the interface conductivity. For unannealed crystalline LAO/STO samples, oxygen vacancies are only partially responsible for a part of the interface conductivity, which can be eliminated by oxygen-annealing.

4.4.2 Ar-milling effect on transport properties

In section 4.4.2, the effect of oxygen vacancies were studied via oxygen annealing experiments. In this section the effect of the polarization catastrophe is investigated by changing the LAO thickness near the critical thickness. We performed Ar-milling experiments to reduce the LAO thickness for both amorphous and oxygen-annealed crystalline LAO/STO heterostructures, which were fabricated at 10^{-3} Torr. **Figure 4.8a** shows a typical thickness dependence of the conductivity (solid red squares) for oxygen-annealed crystalline heterostructures with a critical thickness of 4 uc. We used a 4 uc sample in the Ar-milling experiments. After removing the top unit cell of LAO, the conductivity disappears, as shown by the hollow red diamonds in **figure 4.8a**. This result agrees with previous reports [50, 135]. Moreover, step-by-step (step size of 1 uc) Ar milling of an oxygen-annealed 10 uc crystalline LAO/STO sample generates the same critical thickness of 4 uc for maintaining the interface conductivity (black hollow stars). On the other hand, Ar-milling the unannealed crystalline heterostructure from 10 uc down to 2 uc produces little change in conductance (blue circles), because the conduction by oxygen vacancies remains.

To facilitate control of the Ar-milling rate in the amorphous overlayer case, where the milling rate of LAO was more than twice that of the crystalline case, we intentionally enlarged the critical thickness to be 6 nm by increasing the substrate-target distance and decreasing the laser fluence.

Figure 4.8b illustrates the LAO layer thickness dependence of conductivity (green solid squares) for amorphous LAO/STO samples. As the top amorphous LAO layer is removed, one nm at a time, from a 6 nm LAO/STO sample, the conductivity of the heterostructures is retained (green hollow diamonds). This is similar to unannealed crystalline interfaces but drastically different from oxygen annealed crystalline interfaces.

Previous report [43] has shown that Ar milled STO would create conductivity at room temperature. To check this issue, an insulating 2 nm amorphous LAO/STO sample was used as reference. After the removal of the top 1 nm of amorphous LAO, the heterostructure remains insulating. This excludes the possible conductivity by the Ar-milling process.

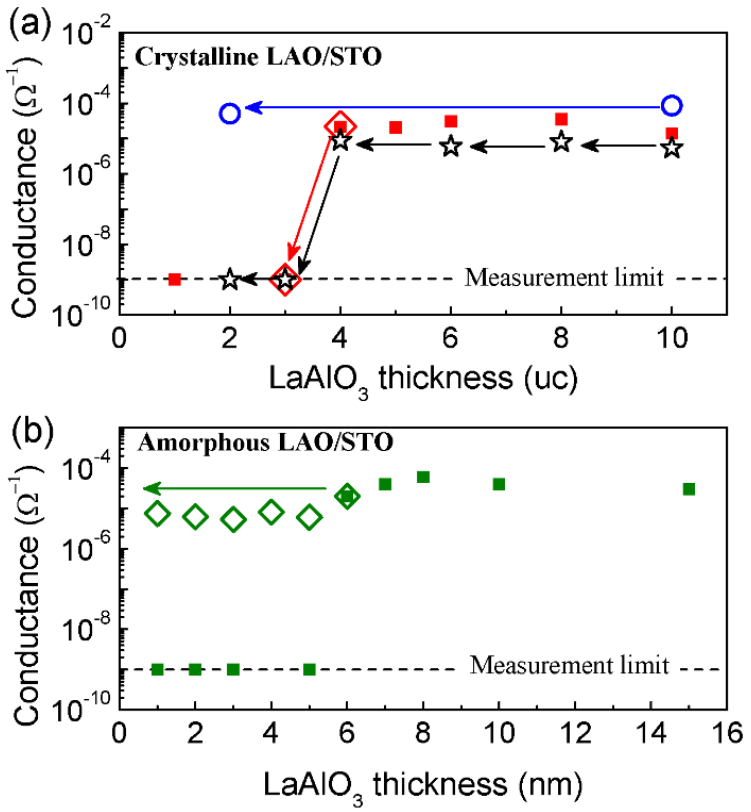

Figure 4.8 Ar-milling effect. (a) Thickness dependence (red solid squares) of room-temperature conductance of oxygen-annealed crystalline LAO/STO heterostructures fabricated at 10-3 Torr and 750 °C, showing a critical thickness of 4 uc. The red hollow diamonds denote that the

conductivity of the 4 uc sample disappears after the removal of the top 1 uc LAO by Ar-milling. Moreover, the blue hollow circles represent the conductance of an unannealed 10 uc crystalline LAO/STO heterostructure and after the removal of the top 8 uc LAO by Ar-milling. The black hollow stars represent the conductance of another oxygen-annealed 10 uc crystalline LAO/STO sample after step-by-step Ar milling. (b) Thickness dependence (green solid squares) of room-temperature conductance of amorphous LAO/STO heterostructures fabricated at 10-3 Torr, showing a critical thickness of 6 nm. The green hollow diamonds represent the conductivity of the 6 nm sample that remains after the removal of the top LAO layer 1 nm at a time by Ar-milling. All the arrows represent the Ar-milling process.

The Ar-milling experiment further confirms that the conductivity in amorphous LAO/STO heterostructures originates principally from oxygen vacancies in the STO substrate. The conductivity formed due to oxygen vacancies is not much affected by the overlayer thickness directly contrast to the electronic reconstruction induced conductivity. The appearance of conductivity in oxygen-annealed crystalline LAO/STO samples is reversible across the critical thickness of 4 uc, which will be further proved in next re-growth experiments. Interface conductivity of oxygen annealed crystalline interfaces is closely associated with the interface electronic reconstruction due to the potential build-up in the crystalline LAO overlayer [65-67]. Once the thickness is reduced below 4 uc, the build-up potential is not enough to cause the electronic transfer so that the interface becomes insulating. This is consistent with the electronic reconstruction at the interface and also the built-in electric field in the polar LAO layer observed by Huang *et al.* [136], who recently performed band alignment mapping across the crystalline interface by cross-section scanning tunneling microscopy.

4.4.3 Re-growth effects on transport properties of crystalline LAO/STO interfaces

To explore furthermore on the reversibility of the thickness dependent conductivity in oxygen annealed crystalline interfaces (see **figure 4.8a**), we re-grew LAO on a crystalline LAO/STO heterostructure after the LAO layer was milled from 4 uc to 3 uc. After the Ar milling, (n×2) surface reconstruction patterns was observed by RHEED both before and after deposition (**figure**

4.9a). No RHEED oscillation was seen during the deposition, which was likely caused by the surface reconstruction of LAO after Ar ion milling. The thickness of the newly deposited LAO layer was estimated to be 2 uc based on calibrated growth rate. Although the re-grown sample shows a measurable room temperature sheet resistance of ~190 kΩ/□, its R_s-T curve exhibits a semiconducting behavior as seen in **figure 4.9b**. Oxygen annealing in 600 ℃ and 1 bar of oxygen flow for 1 h only results in a slight change in sheet resistance, which proves that the partially restored conductance is not from oxygen vacancies. Instead, the partially restored conductance suggests that the polarization catastrophe mechanism still works for the re-grown sample but is limited by the poor crystallinity of the re-grown LAO layer.

For comparison, another re-growth experiment was performed. We first fabricated a 3 uc crystalline LAO/STO heterostructure, which was *ex-situ* measured to be highly insulating. Then one more unit cell of LAO was deposited on such a heterostructure. No surface reconstruction was seen over the entire deposition process (**figure 4.9c**). During the re-growth, periodic RHEED intensity oscillation was obtained. The re-grown sample was subsequently oxygen-annealed and the R_s-T curve shows a typical metallic behavior (**figure 4.9d**). Such re-growth experiments demonstrate that the good crystallinity of the LAO layer is crucial for the polarization catastrophe mechanism for the case of crystalline LAO overlayers.

At last, I would like to add a comment on the Ar milling effect on the crystalline samples. At the time of performing experiments, we considered the etching effect primarily and surface modification as the minor effect. Later, Aurino *et al.*[3] performed a through structural analysis on the Ar milling effect on crystalline LAO/STO heterostructures, in which they identified surface

[3] Aurino et al. "Reversible metal-insulator transition of Ar-irradiated $LaAlO_3/SrTiO_3$ interfaces" Physical Review B, **92**, 155130 (2015).

become amorphous as well as being etched. However, they also found sample becomes insulating after etching with Ar. Hence our primary conclusion remains still valid.

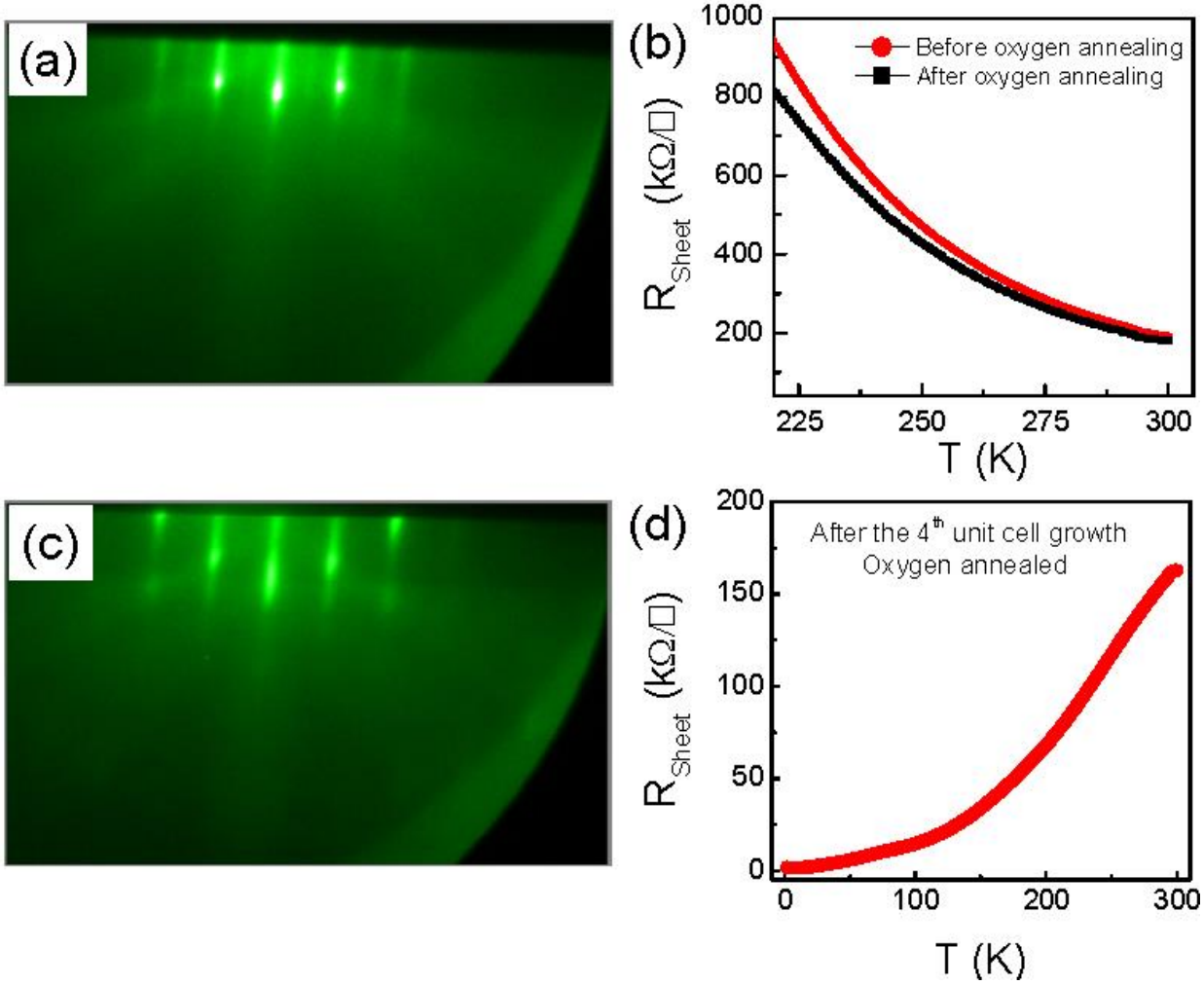

Figure 4.9 Re-growth experiment. (a) Reflection high energy electron diffraction (RHEED) pattern after depositing a new LAO layer (estimated to be 2 uc) on a crystalline LAO/STO heterostructure with the LAO layer etched from 4 uc to 3 uc. (b) R_s-T curves of the re-grown sample stated in (a) before and after oxygen annealing. (c) RHEED pattern after depositing one uc LAO on an as-grown 3 uc crystalline LAO/STO heterostructure. (d) R_s-T curve of the re-grown sample described in (**c**) after oxygen annealing.

4.5 Summary

In conclusion, we did a systematic comparison of transport properties between amorphous and crystalline LAO/STO interfaces through oxygen annealing, Ar milling and re-growth treatments, using PL as a probe for oxygen vacancies. We found that despite there being a critical overlayer thickness of LAO for appearance of conductivity at the LAO/STO interface for both crystalline and amorphous forms of LAO, the explanation in the two cases is different. Unlike the 4 uc critical thickness for the oxygen-annealed crystalline heterostructures, there is no universal critical thickness when the LAO is amorphous. The critical thickness then depends sensitively on deposition conditions, and oxygen vacancies in the STO substrate account for the interface conductivity. Oxygen vacancies also contribute substantially to the conductivity of crystalline LAO/STO heterostructures which have not been annealed in oxygen post deposition. Electrons from electronic reconstruction from polarization discontinuity are degenerate but electrons from oxygen vacancies are thermally activated with small activation energy. The reversible thickness dependence of conductivity across the critical thickness of 4 uc in oxygen-annealed crystalline heterostructures indicates that the interface electronic reconstruction due to the potential build-up in LAO overlayers is ultimately responsible for the conductivity in this case. Moreover, our experiments demonstrate that the crystallinity of the LAO layer is crucial for the polarization catastrophe, which will be further elaborated in chapter 6.

In a simple form, table T1 summarizes the key findings, which offers a clear picture how oxygen vacancies and electronic constructions contribute in LAO/STO interfaces, depending on their fabrication and treatment conditions.

Table 4.1 Different characteristics of crystalline and amorphous LAO/STO interfaces.

	Crystalline LAO/STO		**Amorphous LAO/STO**
Subtype	Oxygen Annealed	As deposited	Amorphous
Carrier Behavior	Almost Degenerate	Carrier Freeze out	Carrier Freeze out
Origin of carriers	Polarization Discontinuity	Polarization Discontinuity + Oxygen vacancies	Oxygen vacancies
Crystallinity	Crucial for conductivity	Not crucial	Not necessary

Chapter 5 Nature of Electron Scattering in $LaAlO_3/SrTiO_3$ Interfaces near the Critical Thickness

Abstract

The 2D electron gas observed at the interface of a polar ($LaAlO_3$) and non-polar ($SrTiO_3$) interface has potential for oxide electronics. Controlling and enhancing the carrier density and electron mobility, critical for device applications, would require a detailed understanding of these interfaces. This interface two dimensional electron gas (2DEG) exhibits a metal insulator transition between 3 to 4 unit cells of $LaAlO_3$. Using reflection high energy electron diffraction (RHEED) we show that the insulator to metal transition of the $LaAlO_3/SrTiO_3$ (LAO/STO) interface after the third layer of LAO occurs at 65% LAO surface coverage. At this critical value of surface coverage we further show that the electron mobility is highly sensitive to the surface coverage, carrier density (varied by back gating) and Kondo scattering (seen at high carrier concentrations). We relate these effects to interface strain, carrier-carrier scattering and magnetic scattering from possible Ti^{3+} defects created by the back gating.

5.1 Different scattering mechanisms of 2DEG LAO/STO interfaces

The two-dimensional electron gas (2DEG) at the interface between a polar (LAO) and non-polar (STO) insulating oxide offers opportunities to develop multifunctional devices. The prospect of this interface will depend on both its performance compared to existing technologies and its ability to integrate with complementary metal-oxide-semiconductor (CMOS) technology. As a measure for the 2DEG electronic quality, the carrier density and mobility are commonly used, and they strongly relate to the quality of the hosting material and interface. A good understanding of the material growth and interface formation therefore would be required to be able to control and tune the electron density and mobility. Experimental efforts have demonstrated control of the mobility

of 2DEG in this system by strain effect [137], conducting atomic force microscopy (CAFM) biasing [57, 59-61] and solvent effect on the polar surface [138, 139] and LAO stoichiometry [140, 141]. While carrier-carrier and magnetic scattering effects have been discussed [51], a careful study of their manifestation in a single system is yet to be performed.

LAO/STO interfaces have a characteristic critical thickness between 3 to 4 uc [48] of LAO to observe the conductivity. Previously, the thickness dependence of transport properties of LAO/STO interfaces was usually carried out with the step size of 1 uc. In this chapter, we carefully control the thin film deposition process to make the step size down to sub-unit-cell scale. The interested thickness regime is between 3 and 4 uc. The first intuitive purpose is to find a more accurate critical thickness for metal-insulator transition. The second purpose is to explore how carrier density and mobility changes across the metal-insulator transition, and hence determine the dominant scattering mechanisms in this thickness regime.

5.2 Experimental: controlled sub-unit-cell thin film growth

LAO thin films with thicknesses between 3 to 4 uc were deposited on TiO_2 terminated (001) STO substrates at 750 ℃ and 10^{-3} Torr oxygen pressure by PLD (KrF laser λ=248 nm) followed by post annealing at 600 ℃ at 0.5 bar oxygen flow for 1 hour. During deposition, the growth process was *in-situ* monitored by RHEED. Since LAO adopts a layer-by-layer growth mode, RHEED intensity oscillates periodically with period equal to the growth time of 1 uc of LAO layer. If we stop the laser before a unit cell growth completes, then a sub-unit-cell growth control can be achieved. Sub-unit-cell grown films are expected to have larger surface roughness compared to the fully covered unit cell films. **Figure 5.1** demonstrate the above described difference in surface morphology by AFM. Compared the surface morphology of 3.5 uc to 3 uc LAO/STO heterojunctions, there are

randomly distributed islands residing on atomic terraces which are clearly seen in 3 uc LAO thin films. In another way, 3.5 uc LAO can be regarded as that 4th unit cell only covers 50% of the sample surface area. During the LAO film growth, islands are firstly formed and then coalescence occurs to form a continuous film. By stopping the laser at different fractions of a unit cell, different stages of surface coverage ratio can be achieved. We have deposited a full serious surface coverage ratio from 50% to 100% of the 4th uc of LAO in the step size of 5% (deposition corresponding to two laser pulses). Experimentally, it is easily controlled because our deposition rate is as slow as 40 sec/uc. All experimental conditions are fixed to maintain a constant deposition rate for all depositions. **Figure 5.2** shows two examples to control the thickness of LAO to be 3.60 and 3.80 uc (i.e. 60% and 80% coverage of 4th uc).

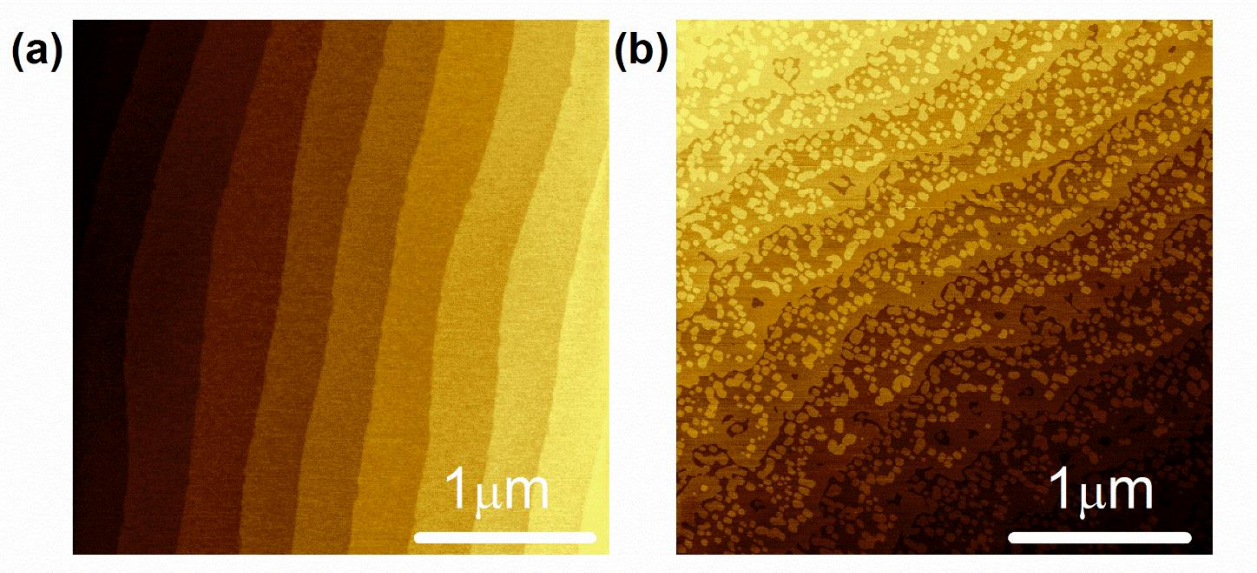

Figure 5.1 (a) and (b): 3 μm × 3 μm AFM images of 3 and 3.5 uc LAO on TiO_2 terminated STO substrates respectively.

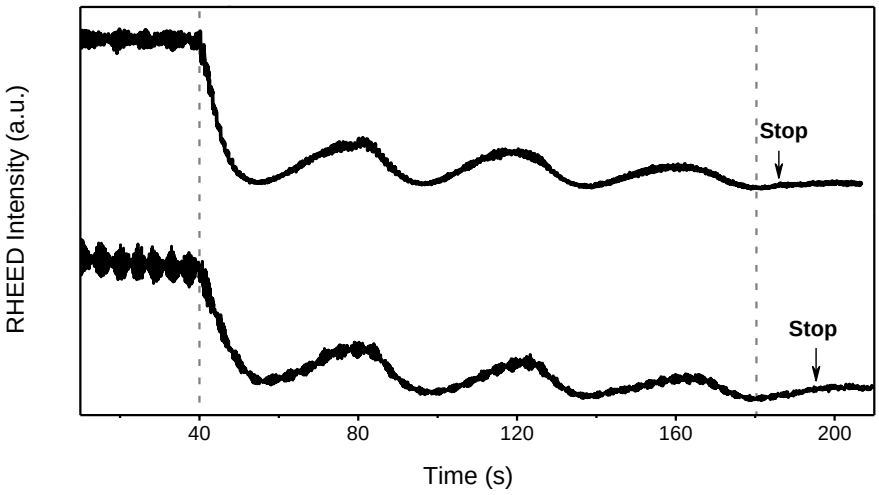

Figure 5.2 RHEED intensity oscillations of fractional layer growth of 3.6 and 3.8 uc of LAO, respectively. Dashed lines are guides to the eye.

5.3 Exact critical thickness

Using controlled RHEED monitoring technique, a number of thickness between 3 and 4 uc LAO crystalline films are grown on treated STO (100) surface. Then room temperature resistance measurements were carried out. We found out that there is a very sharp transition in the room temperature conductivity even in sub-unit-cell scale. As shown in **figure 5.3a**, a four order difference in room temperature conductance was observed at 3.60 uc with only an increment of 0.05 uc (two layer pulses). We have repeated three times to confirm the transition and it is quite reproducible to the accuracy of 0.05uc.

The conductive behavior was also tested for conductive samples, whose thickness is larger than 3.65 uc. **Figure 5.3b** shows that the fitting of R with T^2, which is seen to be a linear relationship, which is identical with the LAO/STO interface with LAO thickness larger than 4 uc. The similarity in the transport behaviors confirms that 3.65 uc, or 65% surface coverage for 4^{th} unit cell, is a more accurate value for the metal-insulator transition critical thickness. Further, compared to a similar

study done by Lee *et al.*[142], where they often see large variance of conductance for 3.5 uc LAO/STO samples, our observed critical thickness is more reproducible.

The 4th polar layer critical thickness of 65% could be explained by 2D percolation theory. The 4th uc islands with size ~100 nm shown in **figure 5.1b** should be conducting. In order for global conductivity which can be measured across the 5×5 mm^2 area, the island density has to reach a critical value readily described by the 2D site percolation theory with a threshold between 0.593 (square shaped islands) and 0.697 (honeycomb shaped islands) [143]. However, considering the dynamic deposition process of LAO growth where conducting islands nucleate and coalesce, it is not possible to define a single unique shape for the conductive islands (**figure 5.1b**) leading to an average of 0.65 for the percolation threshold.

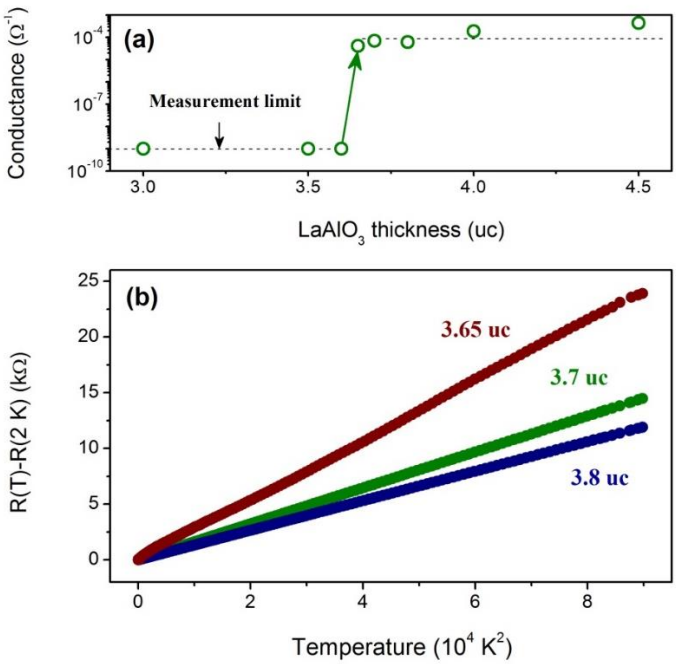

Figure 5.3 (a) Room temperature (300 K) sheet conductance shows a sharp metal insulator transition at LAO thickness of 3.65 uc. Dash lines are given as guides to the eye. (b) Sheet resistance versus T^2 of LAO/STO interface with different LAO layer thickness.

5.4 Electron-electron and strain induced scattering

Since we have found a more accurate critical thickness, the next question we want to ask is what contributing factors to interface conductivity are at the vicinity of the critical thickness. Towards this direction, field effect is the natural choice. A complete series of field effect measurements were carried for multiple samples with thickness from 3.5 to 4 uc at T = 2 K. STO substrates are used as back gates with the gate voltage ranges from -100 V to 200 V. Negative gate voltage is to reduce the carrier concentration and positive voltage is to increase the carrier concentration. Upon application of gate voltage, Hall measurements were carried out to calculate the carrier density and mobility. For reference, bare STO substrate (0 uc LAO thickness) carrier density was top gated by an ionic gel electrolyte in an electric double layer transistor (EDLT) configuration with a Hall bar pattern [50 μm (width) × 160 μm (length)].

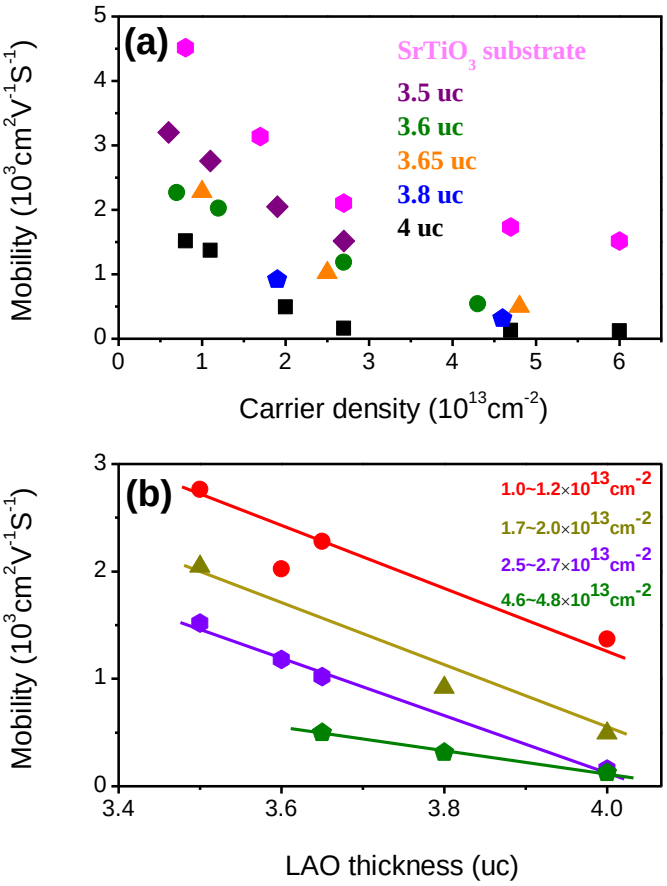

Figure 5.4 A wide range of carrier density of LAO/STO interface is achieved by field effect using STO as a back gate while variation of bare STO carrier density is achieved by top gating using ion liquid at 2 K. (a) Carrier mobility versus carrier concentration of electrons (field induced and 2DEG of LAO/STO interface) with LAO thickness ranging from 3.5 to 4 uc (b) Carrier mobility of 2DEG at LAO/STO interface versus LAO thickness for different carrier concentration ranges.

Figure 5.4a shows the carrier density and corresponding mobility for different LAO thicknesses. A wide range of carrier density, 1×10^{13} to 6×10^{13} cm^{-2}, is achieved using this back gating set-up; and carrier mobility varies from 100 to 5000 $cm^2V^{-1}s^{-1}$. The general trend is lower mobility with increasing carrier density. Considering the previous observed resistance linearly proportional T^2 relationship, we could attribute this trend to carrier-carrier scattering in the Fermi liquid model. Mobility decreases linearly with increasing carrier density before saturation for 4 uc LAO/STO. The almost linear decrease relationship are also present in other thickness but saturation trend is

not observed in 3.5, 3.6, 3.65 and 3.8 uc samples most likely due to the maximum achieved carrier concentration are not high enough.

The other noticeable trend is that for similar carrier concentration, the thinner the overlayer, the larger the mobility, with the highest mobility observed in bare STO substrate. For instance, with the carrier density level ~ 2.7×10^{13} cm^{-2}, the mobility of 3.5, 3.6, 3.65 and 4 uc samples are 1518, 1182, 1022 and 160 $cm^2V^{-1}s^{-1}$ respectively. This trend is explicitly shown in **figure 5.4b** where carrier mobility decreases linearly with the LAO thickness in a narrow carrier density range to maintain the same carrier-carrier scattering effect for all LAO thickness interfaces. In the carrier density range from 1×10^{13} to 2.7×10^{13} cm^{-2}, the slope is a constant value of -2830 $cm^2V^{-1}s^{-1}uc^{-1}$. The large slope shows extremely high sensitivity of carrier mobility on the surface coverage ratio of 4th unit cell of LAO, which has never been observed before. The effect of surface coverage on mobility is most likely due to the effect of strain (e.g. TiO_6 octahedron distortion), where the surface STO experiences a compressive strain by the coherent grown LAO layer on top. Since the 2DEG is confined at top few uc of STO [144], which experience much larger strain from the LAO expitaxial layer than the bulk. Our trend of decreasing of mobility with increasing LAO thickness of the 2DEG at LAO/STO is consistent to previous report [145]. However, up to date, such a high sensitivity of mobility on strain is only seen in the thickness interval between 3.5 and 4 uc of LAO across the metal-insulator transition.

Before we move on, we would like to address the issue that every data point in **figure 5.4a** is an average of at least three samples to minimize the error. **Figure 5.5** shows an example of how three samples of LAO thickness 3.65 samples are measurement to get a data point in **figure 5.4a**. There is a large variation of carrier mobility and carrier concentration for as prepared samples with same thickness and same growth conditions. Upon gating to tune the carrier concentration to a fixed

value, the carrier density spread is much smaller. The triangle symbol represents the average value of 3 samples being gated to a constant carrier concentration. Every data point in **figure 5.4** is obtained in this manner.

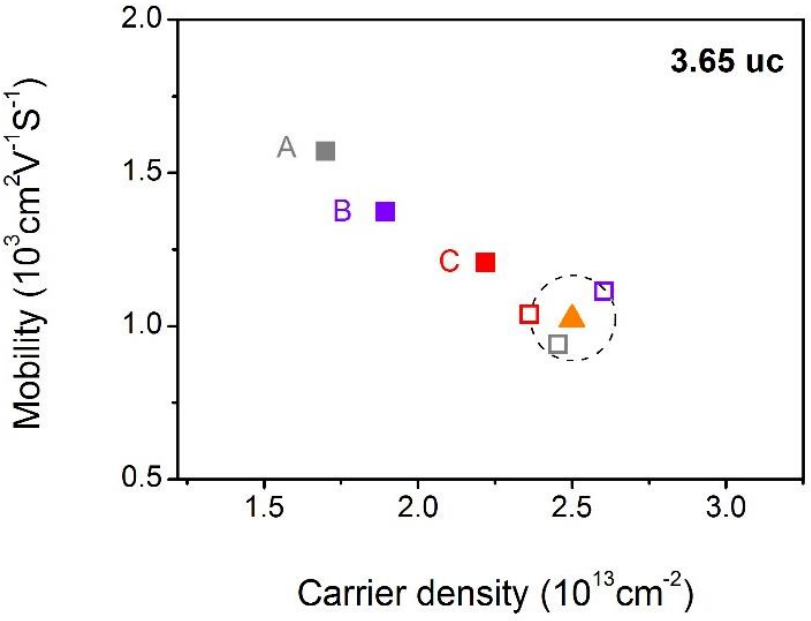

Figure 5.5 Carrier mobility mapping with carrier concentration for three 3.65 uc LAO/STO samples before and after back gating. Solid squares denotes three as grown samples A, B and C and open squares represents the carrier mobility of samples being gated to the fixed carrier density ~ 2.5×10^{13} cm^{-2}. The average value of mobility and carrier density of three samples is the data point (yellow triangle) being plotted in **figure 5.4**. The dashed circle shows much less spread in carrier mobility once carrier density is gated to a common value compared to as prepared samples.

Furthermore, the possible effect of sensitivity of the carrier mobility on the LAO thickness is the surface stoichiometry, since stoichiometry has been shown to be important for LAO/STO interface conductivity [146-148]. The possibility that surface stoichiometry of partially covered surface is different from the fully covered surface. To minimize this issue, we have kept laser fluence, substrate-target distance and oxygen pressure the same throughout different depositions. Hence most likely the stoichiometry variation between samples are minimum. Within a sample, determination of the stoichiometry variation between the surface monolayer and the underneath

layer is extremely challenging. The phase image of AFM scanning would see a contrast due to the chemical composition difference (La/Al segregation). Here we show the phase image of 3.5 uc sample along with topography image in **figure 5.6**. It does not show additional phase contrast between the surface of 3 uc and the 1 uc partial coverage on top except the topological effect (the edge of the islands). This serves as an implicit evidence for uniformity of surface stoichiometry throughout.

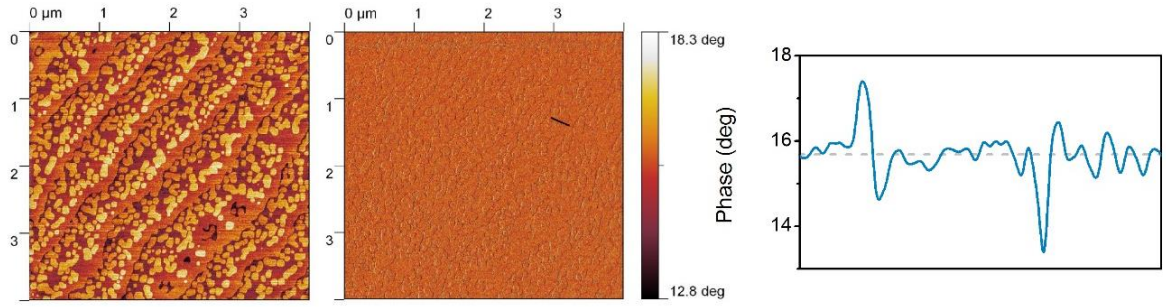

Figure 5.6 The topography (left) and phase image (middle) of LAO(3.5 uc)/STO. The right figure shows the line profile (marked as a black line in phase image) crossing one island. This indicates that major phase contrast comes from the topological effect (edge of the island). With no contrast in phase image except the topography contrast, no chemical composition change occurs for the partially grown 4th uc.

5.5 Kondo like scattering at high carrier density

Refer to **figure 5.4b**, we found that the slope of the mobility versus LAO thickness is 1060 $cm^2V^{-1}s^{-1}uc^{-1}$ when the carrier density is ~ 4.7×10^{13} cm^{-2}, which is much smaller compared to the slope when carrier density is lower than 2.7×10^{13} cm^{-2}. The different slope value indicates the possible additional scattering mechanism at high carrier density. **Figure 5.7a and 5.7b** show that appearance of resistance minimum due to gating 3.65 and 4 uc LAO/STO interface to high carrier density, respectively. The temperature of resistance minimum is found to be dependent on the LAO thickness even though the carrier concentration is maintained at the same level. **Figure 5.7c**

shows the temperature of resistance minimum when the carrier concentration is kept at 4.8×10^{13} cm^{-2}. Top gated STO substrate shows no upturn of resistance at low temperature while 3.65, 3.8 and 4 uc LAO/STO samples show temperature of resistance minimum at 15, 17 and 20 K respectively.

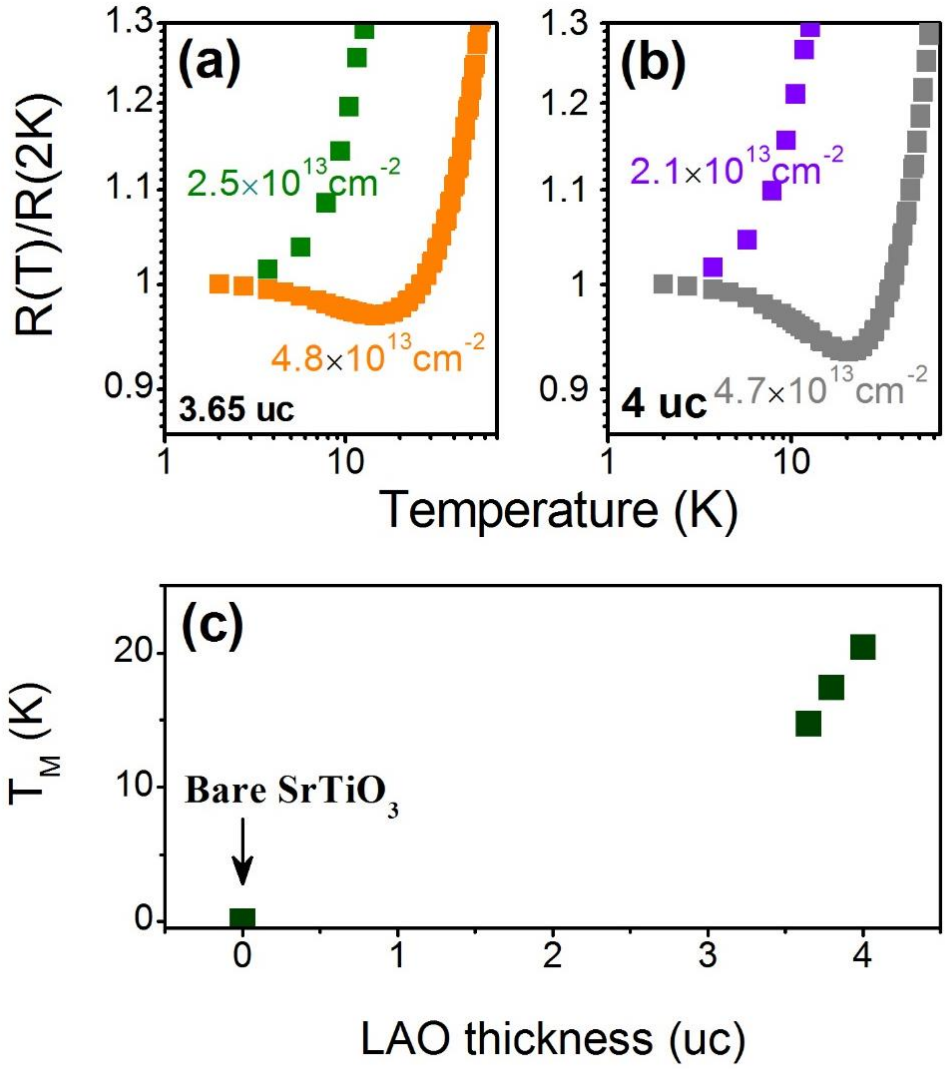

Figure 5.7 (a) and (b): The sheet resistance versus temperature curves of LAO/STO for LAO thickness of 3.65 and 4 uc respectively for different carrier densities. (c) LAO thickness dependence of the temperature of resistance minimum TM at a carrier density of $(4.5\pm0.3)\times10^{13}$ cm^{-2}.

The appearance of resistance minimum could be resulted by weak localization and Kondo effect. To further distinguish these two possible origins, we carried out angular magnetoresistance (AMR) measurements for the samples before and after gating. It is defined by MR(%) = (R(B)-R(0))/R(0) × 100%, where R(0) is the resistance without magnetic field while R(B) is the resistance with magnetic field B. The sample position is defined by the angle θ between magnetic field and the normal of sample surface. When θ is 0º or 180º, field is out of plane and when θ is 90°, magnetic field is in plane but perpendicular to current direction. As shown in **figure 5.8**, anisotropic MR is shown in 3.65 uc sample carrier density is 2.5×10^{13} cm^{-2}. MR is 14% in out of plane direction and -1% in in-plane direction when magnetic field is 2 T and temperature is at 2 K. This is consistent with reported 2DEG MR features [149, 150]. MR become negative isotropic with a constant value of -4% when carrier density is 4.8×10^{13} cm^{-2} where it shows the resistance minimum at low temperature. Similarly, anisotropic MR (48% for out of plane MR and -2% for in-plane MR) changes to isotropic negative MR of -6% for 4 uc LAO/STO interface when the carrier density changes from 2.1×10^{13} to 4.7×10^{13} cm^{-2}. Isotropic negative MR is one of the characteristics of Kondo scattering besides the resistance minimum. In a simple picture, anisotropic MR observed at lower carrier density arises from orbital effects on scattering. Isotropic MR is more related to spin effect on scattering and hence related to scattering originated from localized magnetic moments.

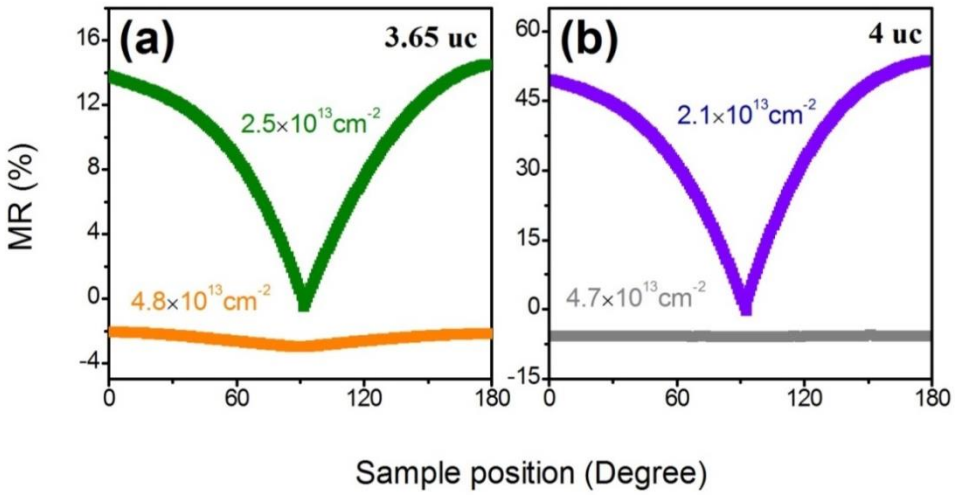

Figure 5.8 (a) and (b): Angular dependent magnetoresistance of 3.65 and 4 uc LAO/STO respectively at different carrier densities at 2 K and a magnetic field of 2 T.

The change from anisotropic to isotropic MR with only a factor of two increase of carrier density sheds light on the possible origins of the magnetic moments (necessary for Kondo scattering) at the LAO/STO interface. A similar trend in electrolyte gated Kondo effect on STO [151] was seen but at carrier concentration much higher (9.2×10^{13} cm^{-2} in bare STO versus 4.7×10^{13} cm^{-2} in our 3.65—4 uc LAO/STO interface). The Kondo center is likely from localized Ti^{3+} with d^1 electronic configuration. The Ti^{3+} state was confirmed by the electron energy loss spectroscopy [65], resonant inelastic x-ray scattering [152] , x-ray photoemission [153, 154] and x-ray absorption specsrtopy studies [155], while electrolyte gated bare STO single crystal was regarded as admixture of magnetic Ti^{3+} and delocalized electrons which fill the Ti 3d bands partially [66, 155, 156]. Our experimental results on the similarity among bare STO substrate and 3.5---4 uc thickness LAO/STO interfaces on tunable Kondo effect unifies the above two ideas. In short, electrons, either transferred from the LAO due to polar discontinuity or from electrostatic induction by back gating, can change the electronic states of Ti near the surface of STO leading to partially filled Ti 3d states. Part of them form localized magnetic centers $Ti^{3+,}$ while the left over become delocalized

and can be probed by transport measurements [152, 156]. The interaction between the two leads to the Kondo effect.

It is interesting to compare the observed Kondo scattering in bare STO with LAO/STO interfaces. The difference is that LAO/STO interface needs much less carrier concentration to observe the similar Kondo effect. As described above, the compressive strain imposed by the LAO overlayer facilitates the localization of carriers and formation of localized magnetic moments, making the Kondo obvious even at a lower carrier concentration. This is also consistent with the fact that the temperature of resistance minimum is lower in thinner LAO/STO interface at the same concentration level (seen in **figure 5.7c**). The experimental evidence on Kondo effect observed in 26 uc LAO/STO interface [51] with higher resistance minimum temperature without external gating field also proves that strain tends to enhance Kondo scattering.

5.6 Summary

In conclusion, we observed a sharp critical thickness threshold for the onset of the 2DEG at the LAO/STO interface of 3.65 ± 0.05 uc of LAO, which can be explained by the 2D percolation model. Near the metal-insulator transition, carrier-carrier scattering, strain induced and Kondo like scattering are seen and strongly influence the transport properties of the LAO/STO interface. The carrier-carrier scattering causes a linear carrier density dependent decrease of the mobility at low carrier concentration regime. Dramatic strain effects on the mobility are observed near the critical threshold across a large carrier concentration range. Enhancement of the carrier density by a factor of two using electric field effect leads to a significant onset of Kondo scattering most likely from Ti^{3+} ions at the interface. Furthermore, strain enhances the Kondo scattering at high carrier

concentration. These experimental results will guide us in the fabrication of electronic and opto-electronic devices based on oxide interfaces.

In this chapter, the observed Kondo effect upon gating of the LAO/STO interfaces lead to an experimental proposal to study possible valence change of the Ti during the back gating experiments. I have planned to design a sample stage to make the back gating possible inside an X-ray photoemission (XPS) chamber. The *in-situ* XPS measurement of Ti valence states upon a gating bias would provide direct evidence on the possible appearance of the Ti^{3+}.

Chapter 6 Tailoring the Two Dimensional Electron Gas at Polar $ABO_3/SrTiO_3$ Interfaces for Oxide Electronics

Abstract

Integrating oxide electronics with silicon is one of the many strategies for microelectronics beyond Moore's law. The 2D electron gas at the polar/non-polar oxide interface has become an important platform for several novel oxide electronic devices. In this paper, the transport properties of a wide range of polar perovskite oxide $ABO_3/SrTiO_3$ (STO) interfaces, where ABO_3 includes $LaAlO_3$, $PrAlO_3$, $NdAlO_3$, $NdGaO_3$ and $LaGaO_3$ in both crystalline and amorphous forms, were investigated. A robust 4 uc critical thickness for metal insulator transition was observed for crystalline polar layer/STO interface while the critical thickness for amorphous ones was strongly dependent on the B site atom and its oxygen affinity. For the crystalline interfaces, a sharp transition to the metallic state (i.e. polarization catastrophe induced 2D electron gas only) occurs at a growth temperature of 515 ˚C which corresponds to a critical relative crystallinity of ~ 70 ± 10 % of the $LaAlO_3$ overlayer. This temperature is generally lower than the metal silicide formation temperature and thus offers a route to integrate oxide heterojunction based devices on silicon.

6.1 Need for comparison of diverse polar ABO3/STO Interfaces

Properties not seen in bulk but arise at the LAO/STO interfaces indicate that electronic/orbital reconstruction play a crucial role. The proposed polarization catastrophe model [65], describing electronic reconstruction at the LAO/STO interface to prevent the electrostatic potential divergence with LAO thickness, fits well in the picture. The polarization catastrophe model lead to extensive reports on conductive crystalline ABO_3/STO heterostructures, including $NdGaO_3$, $NdAlO_3$, $PrAlO_3$, [68, 70, 157, 158] etc. The model was challenged when Chen *et al*. [126] reported a 2DEG with similar carrier concentration and mobility at amorphous LAO/STO interface. It was

also found that even the conductivity of crystalline LAO/STO interface was affected by oxygen vacancies which are created during the growth process [77]. Our prior work [159] classified the 2DEG into two different carriers at LAO/STO interface: one from polar catastrophe (2DEG-P) and the other from oxygen vacancies in STO (2DEG-V). It was shown that the two carriers had different activation energies, 2DEG- P (~0.5 meV) and 2DEG-V (~4 meV) which lead to the 2DEG-V showing carrier freeze out at low temperature while the 2DEG-P remained degenerate down to 2 K. However, the comparison between 2DEG-P and 2DEG-V in diverse ABO_3/STO interfaces has not been explored yet as this could be important for oxide electronic devices. For instance, the amorphous oxide with low oxygen affinity does not lead to any conductivity at the amorphous ABO_3/STO interface. Will such polar oxide overlayers generate only 2DEG-P at the crystalline interface thereby increasing device reproducibility? What about the degree of crystallinity of the polar layer required for producing a 2DEG-P? We have shown the importance of crystallinity for 2DEG-P formation in our prior work [159]. In addition, Mathew *et al.* [160] reported that ion beam irradiation induced defects reduce carrier conductivity of LAO/STO interface and can be used for patterning the 2DEG-P. Hence, determination of the critical crystallinity for stable 2DEG-P is very important especially for future oxide electronics applications and integration with Si.

2D electron gas at complex oxide interfaces is unique as the entire medium is transparent in the visible light to mid-infrared range suggesting the possibility of opto-electronic devices based on this interface. Furthermore, as the carrier density can be tuned by the back gate voltage in virtue of the large dielectric constant of $SrTiO_3$, this could enable optical tunable properties as well. For wide spread application of oxide electronics, the compatibility for oxide growth on silicon is important, however silicon reacts aggressively with most metals at typical film growth temperature

about 600 ℃ [161]. Thus a systematic study of the temperature growth window of polar/non-polar interface is highly desired. Here we address these issues in various ABO_3/STO interfaces by a systematic comparison of transport properties of various amorphous and crystalline interfaces, including a growth temperature dependent study.

6.2 Experimental

All the samples were prepared by pulsed laser deposition equipped with in-situ reflection high energy electron diffraction (RHEED) with the KrF excimer laser (λ=248 nm). Laser energy density and frequency was kept at 1.2 J/cm^2 and 1 Hz for all depositions. Prior to deposition, (001) STO substrates were buffered-HF treated and air annealed in order to get TiO_2 terminated atomically flat surfaces. Crystalline ABO_3/STO heterostructures were deposited at 750 ℃ and amorphous ones at room temperature ~25 ℃. (The temperature was measured by a thermocouple spot welded to the heater plate surface. While the actual temperature of the substrate surface could be smaller by as much as 50 ℃, as it is difficult to measure we quote here only the heater surface temperatures). LAO/STO samples with different crystallinity were deposited at different temperatures from 25 ^{o}C to 850 ^{o}C and characterized both by X-ray diffraction and transport measurements. Oxygen pressure for all depositions was kept at 10^{-2} Torr. The thickness of crystalline film was monitored by RHEED oscillation, for amorphous samples this was controlled by growth duration. After deposition and cooling in deposition atmosphere, samples are named as as-deposited samples, and samples went through additional oxygen annealing process (at 500 ^{o}C in flowing 0.5 bar oxygen for two hours) are referred as oxygen annealed sample. Transport measurements were performed by Quantum Design Physical Property Measurement System (PPMS), resistance and Hall measurement was measured by Van der Pauw configurations with ultrasonic Al bonded contacts.

6.3 Transport properties of diverse crystalline and amorphous ABO_3/STO interfaces

Figure 6.1a and **6.1b** show the schematic images of the crystalline and amorphous LAO/STO interfaces, respectively. The distinct difference between these two interfaces is the absence of the long-range order in the amorphous interfaces. The prerequisite for the polar catastrophe is the alternative stacking of positive and negative charge sheets of the polar layer such that a 2DEG-P can be formed when the build-up potential is larger than the bandgap of STO. Clearly amorphous interface does not satisfy that condition. Experimentally, crystalline and amorphous heterojunctions show very similar topography in AFM images. As shown in **figure 6.1c** and **6.1d**, both surfaces show atomic terraces which resemble the surface of the treated STO substrate surface. Nonetheless, the crystallinity can be detected by RHEED pattern during the deposition. RHEED patterns before and after deposition of crystalline and amorphous LAO/STO heterojunctions are shown in **insets of figure 6.1c and 6.1d**. After deposition, a streaky pattern is observed in crystalline LAO deposition while a faint uniform background in amorphous film. The diffuse scattering dominates over coherent scattering due to lack of lattice periodicity at the amorphous LAO film surface so that there is no observable line or dot pattern.

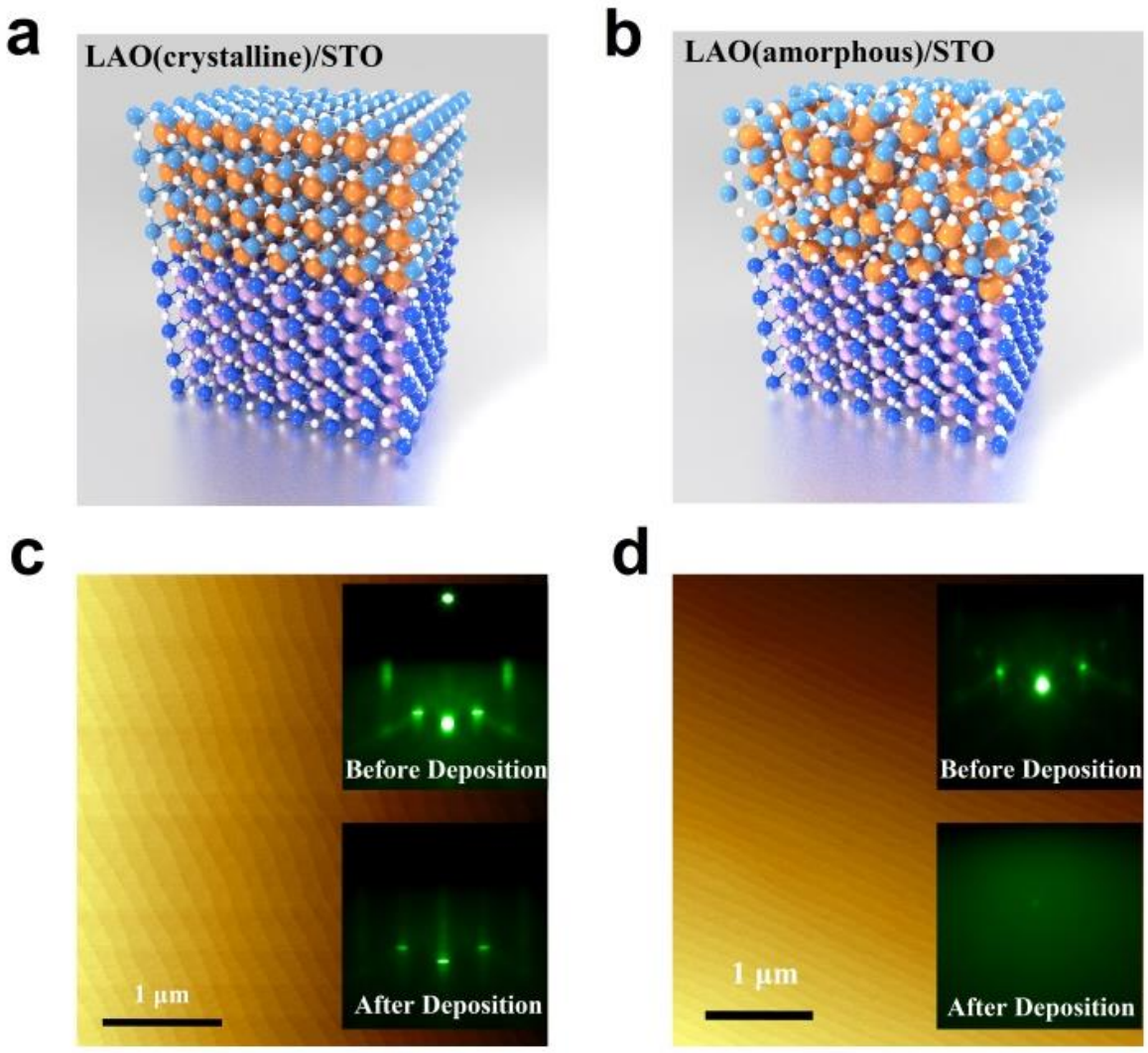

Figure 6.1 Schematic images of (a) crystalline and (b) amorphous LAO/STO heterojunction. AFM images of topography of (a) crystalline and (b) amorphous LAO/STO heterojunctions, respectively. Inset of (c) and (d), RHEED patterns of LAO/STO before and after LAO deposition.

Sheet resistance versus temperature of $NdGaO_3$ (NGO), $PrAlO_3$ (PAO), $NdAlO_3$ (NAO) and LAO on STO is summarized in **figure 6.2a-e**, respectively. It is found that all 4 uc oxygen annealed crystalline interfaces show metallic behavior in the whole temperature regime from 300 to 2 K. However variations are seen in amorphous interfaces. Primarily, amorphous heterostructure seems to be strongly affected by B-site element, i.e. $AAlO_3$ (aluminate) based interface is more conductive than $AGaO_3$ (gallate) based interface. Amorphous NGO/STO interface shows no

measurable conductivity even when the thickness of NGO is up to 5 nm. In addition, we have observed a transition from semiconducting to metallic behavior in amorphous PAO/STO heterojunction with increasing PAO thickness from 2.4 to 2.8 nm (**figure 6.2d**), which illustrates how resistivity behavior is affected across the Mott limit by increasing amount of oxygen vacancies. This B-site element dependent conductivity of polar/non-polar interface strongly suggests that the elemental chemical redox reaction model is dominating in the amorphous case. It is consistent with the fact that aluminum oxygen affinity is much stronger than that of gallium [162].

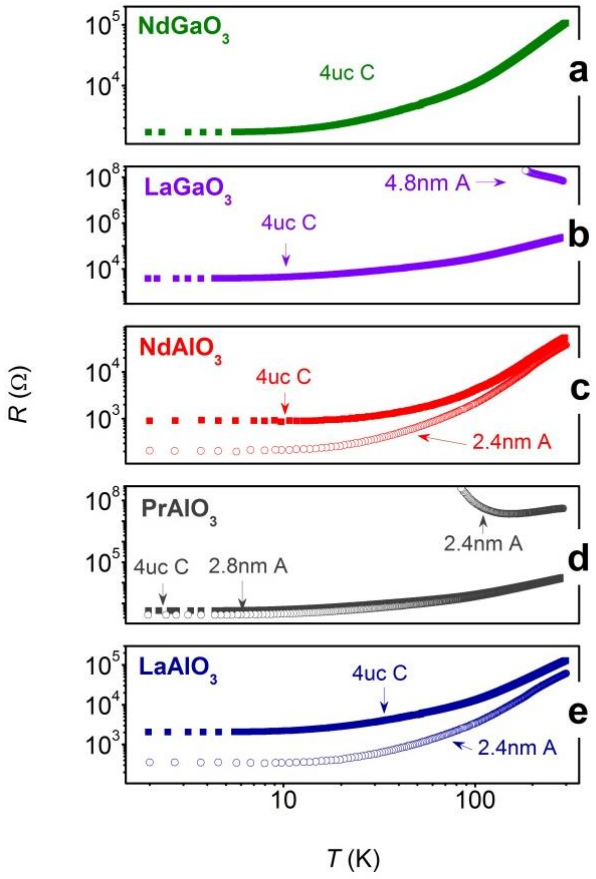

Figure 6.2 Temperature dependent sheet resistance for crystalline and amorphous ABO_3/STO with different thicknesses of ABO_3- (a) $NdGaO_3$, (b) $LaGaO_3$, (c) $NdAlO_3$, (d) $PrAlO_3$ and (e) $LaAlO_3$. "4 uc C" means 4 uc (~ 1.6 nm) of polar ABO_3 layer in crystalline form, and "2.4 nm A" refers to 2.4 nm of polar layer in amorphous form.

The other difference between crystalline and amorphous ABO_3/STO is on critical thickness for metal insulator transition. **Figure 6.3a-e** shows the room temperature conductivity versus ABO_3 layer thickness in both amorphous and crystalline interfaces. In crystalline interfaces, all interfaces show a sharp metal insulator transition occurring at 4 uc where 4 orders ($10^{-9}\ \Omega^{-1}$ to $10^{-5}\ \Omega^{-1}$) of conductance change was observed at room temperature by adding only one unit cell from 3 uc consistent with earlier results [157]. Although aluminate and gallate introduce diverse interfacial strain and local chemical environment, the polar nature of the overlayer dominates the creation of 2DEG-P process. In contrast, the critical thickness for the conducting amorphous ABO_3/STO is more dependent on the oxygen affinity of B-site cation besides experimental conditions (e.g. oxygen pressure). As can be seen in **figure 6.3a-e** and summarized in **6.3f**, critical thicknesses of amorphous $AAlO_3$/STO interfaces are between 2.4 to 2.8 nm, much smaller than $AGaO_3$/STO interfaces (≥ 5 nm).

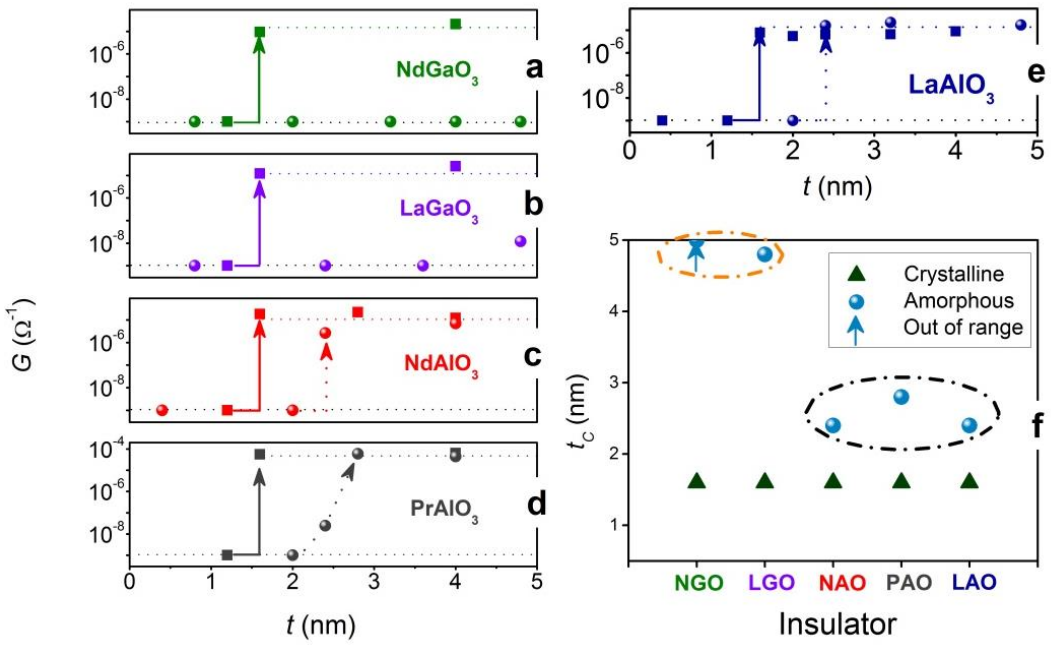

Figure 6.3 Thickness dependent conductance of crystalline (solid squares) and amorphous (solid spheres) ABO_3/STO where ABO_3 includes (a) $NdGaO_3$, (b) $LaGaO_3$, (c) $NdAlO_3$, (d) $PrAlO_3$ and

(e) $LaAlO_3$. Crystalline ABO_3/STO show universal critical thickness of 4uc while critical thickness of amorphous ABO_3/STO is dependent on B-site atoms, as shown in (f). The solid arrow represents the metal insulator transition for crystalline interfaces while dashed arrow for amorphous interfaces transition. Dash lines are given as guides to the eye.

The difference in oxygen vacancy creation between aluminate and gallate polar oxide also affects the transport properties of crystalline interfaces. In **figure 6.4a**, carrier density is more temperature sensitive in 4 uc as deposited crystalline LAO/STO interface than the counterpart NGO/STO interface; similar to previous report [163]. Moreover, oxygen annealing has less effect in temperature dependent carrier density curve of NGO/STO interface. This direct evidence confirms that the oxygen vacancy content in 4 uc NGO/STO interface is much less compared to LAO/STO interface. The other noticeable trend is that carrier mobility in NGO/STO interface is higher than that in LAO/STO interface (see **figure 6.4b**) as NGO/STO has less strain compared with LAO/STO (1.1 % versus 3.0 % in LAO/STO). The key point here is that by using a less oxygen affinity B cation the 2DEG in the crystalline case is dominantly from polar contribution which will enhance the reproducibility of devices as they will be less affected by oxygen pressure during processing steps.

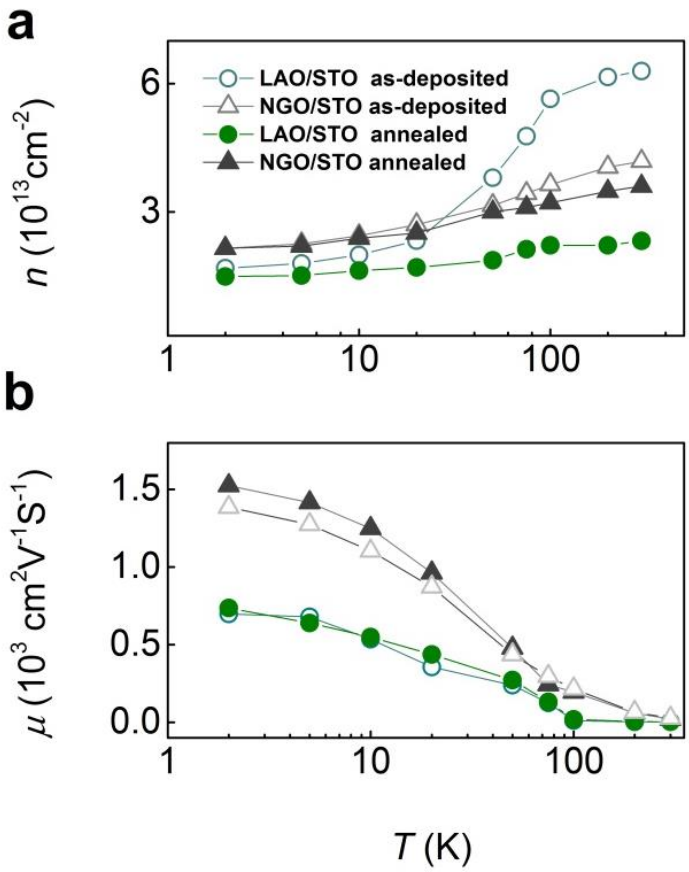

Figure 6.4 (a) Carrier density and (b) carrier mobility versus temperature curves for 4 uc LAO/STO and NGO/STO interface before and after oxygen annealing, respectively.

6.4 Critical crystallinity for 2DEG-P at LAO/STO interface

To find the critical crystallinity for a stable 2DEG-P, we did a systematic study on LAO/STO interfaces prepared at different substrate temperatures from 25 to 850 ℃. The thickness of LAO was kept at 4 nm (10 uc). As shown in **figure 6.5a**, all the as-deposited samples (light blue squares) are conducting with conductance ~2×10^{-5} Ω^{-1} at room temperature and show metallic behavior without significant difference. After oxygen annealing at 500 ℃ with 0.5 bar of oxygen flow, samples (dark red solid spheres) prepared at 500 ℃ and below become highly insulating while samples prepared at 515 ℃ and above are still conducting with about seven fold increase of sheet resistance (see **figure 6.5b**). After oxygen annealing, 2DEG-V is removed, 2DEG-P is the only

responsible mechanism for the metallic behavior. As mentioned before, high crystallinity is crucial for 2DEG-P. The critical temperature of 515 ℃ is most likely the crystallization temperature of LAO film.

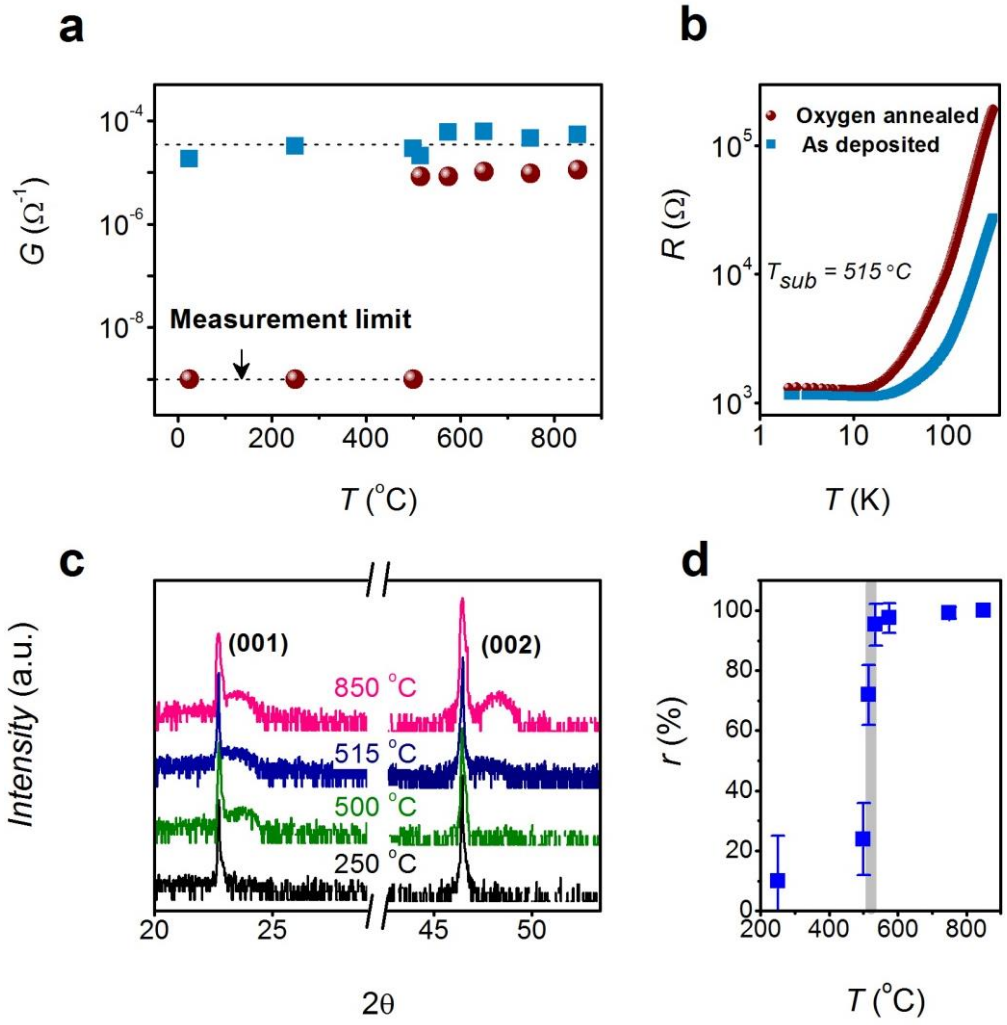

Figure 6.5 (a) Deposition temperature dependence of room temperature conductance of as deposited (blue squares) and oxygen annealed (Brown spheres) LAO/STO interfaces with LAO thickness of 4 nm (10 uc). (b): Temperature dependence of resistance of as deposited and oxygen annealed LAO/STO prepared at 515 °C. (c) X-ray diffraction (XRD) spectra of LAO/STO heterojunction with fabrication temperature of 250, 500, 515and 850 °C. (d) Growth temperature dependence of normalized crystallinity, r, defined as area ratio of (002) LAO to STO XRD peak normalized to area ratio at growth temperature of 850 °C. The solid line in (d) is given as guide to the eye.

This is confirmed by the XRD spectra in **figure 6.5c** where no distinct LAO XRD peak is seen when the substrate temperature is below 250 C. LAO peaks starts to appear when the substrate temperature is above 500 ℃ and saturate at 600 ℃ and above. Due to the difficulty of quantifying crystallinity precisely, we use the area ratio of LAO (200) peak to substrate STO (200) peak as a figure of merit. The area ratio is normalized to the area ratio at 850 ℃. **Figure 6.5d** shows the area ratio, r in percentage, dependence on the substrate temperature. A sharp increase occurs at ~500 ℃. Within a narrow window from 500 to 575 ℃, the crystallinity increases from 20 ±15 % to nearly 100 % rapidly, which qualitatively describes the crystallization near the crystallization temperature. The minimum temperature for stable 2DEG-P of 515 ℃ corresponds to the area ratio of ~ 70 ±10%, which defines the critical crystallinity for 2DEG-P formation in LAO/STO system. The incompletely crystalized LAO film can be divided into crystalline and amorphous region. Crystalline regions induce electron transfer and form localized conductive islands while area under amorphous region is insulating. When the conductive regions reach the 2D percolation threshold, a macroscopic conducting network is established which shows global conductivity. This picture is evidenced by the fact that carrier density of 2DEG-P is lower at low growth temperatures [164]. This is analogues to our previous result that ~65 % surface coverage of 4^{th} uc of LAO is the threshold value for MIT in crystalline LAO/STO interface [165]. Fortuitously, the minimum growth temperature of 515 ℃ is just adequate to avoid silicide formation (e.g. $TiSi_2$ and $SiSr_2$ formation at STO/Si interface at 600 -700 ℃ [161] and 650 -700 ℃ [166, 167], respectively.) which accounts for structural quality degradation of epitaxial STO on Si. As a result, 2DEG-P properties at ABO_3/STO interface are ready for integration with silicon considering that a number of groups have reported on high quality epitaxial STO growth on Si [168-172].

6.5 Summary

In summary, through systematic comparison between transport properties for a series of ABO_3/STO, we have shown that the relative contribution of 2DEG-P and 2DEG-V to the transport can be tailored by varying the B cation. In addition, critical substrate temperature of 515 ℃ marks the onset of 2DEG-P formation at the LAO/STO interface which corresponds to a crystallinity of $70 \pm 10\%$. These results offer alternate experimental evidences for the requirement of an ordered polar layer for the polar catastrophe model at a crystalline interface and the oxygen redox model at an amorphous interface. Further, the work sheds light on the role of key process parameters (temperature and oxygen pressure during growth) for the possible integration of oxide heterojunction based devices on silicon.

Chapter 7 Imaging and Control of Ferromagnetism in $LaMnO_3/SrTiO_3$ Heterostructures

Abstract

Atomically sharp oxide heterostructures often exhibit unusual physical properties that are absent in the constituent bulk materials. The interplay between electrostatic boundary conditions, strain and dimensionality in ultrathin epitaxial films can result in monolayer-scale transitions in electronic properties. Here we report an atomically sharp transition to a ferromagnetic phase when polar antiferromagnetic $LaMnO_3$ (001) films are grown on $SrTiO_3$ substrates. For a thickness of five unit cells or less, the films are antiferromagnetic, but for six unit cells or more, the $LaMnO_3$ film becomes ferromagnetic over its entire area, which is visualized by scanning superconducting quantum interference device microscopy. The transition is explained in terms of electronic reconstruction originating from the polar nature of the $LaMnO_3$ (001) films. Our results demonstrate how new emergent functionalities can be visualized and engineered in oxide films that are only a few atomic layers thick.

7.1 Surface and structural properties of LMO films

Modern thin film deposition techniques enable the synthesis of complex oxide thin films with unit cell (uc) level control over the thickness. Remarkably sharp phase transitions have been discovered in several systems upon increasing film thickness [48, 97, 173-176]. The most prominent example is the 2-dimensional electron gas (2DEG) formed between insulating thin films of $LaAlO_3$ and insulating TiO_2-terminated $SrTiO_3$ (STO) substrates, which occurs at a critical $LaAlO_3$ thickness of 4 uc [48]. Here we want to explore whether the similar magnetic phase transition could occur.

For this purpose, LMO (001) films with a thickness varying from 1 uc to 24 uc were grown using pulsed laser deposition (λ=248 nm) monitored by reflection high energy electron diffraction (RHEED), on TiO_2-terminated (001)-oriented STO substrates, in a 10^{-2} mbar oxygen pressure. All samples were cooled to room temperature under the same oxygen pressure. LMO shows layer-by-layer growth mode evidenced by RHEED oscillation up to 25 uc (see **figure 7.1a**). AFM images (**figure 7.1b and c**) show LMO thin films are atomically smooth with atomic terraces seen much like the treated STO substrates. All the films were found to be insulating and several examples are shown in **figure 7.1d**.

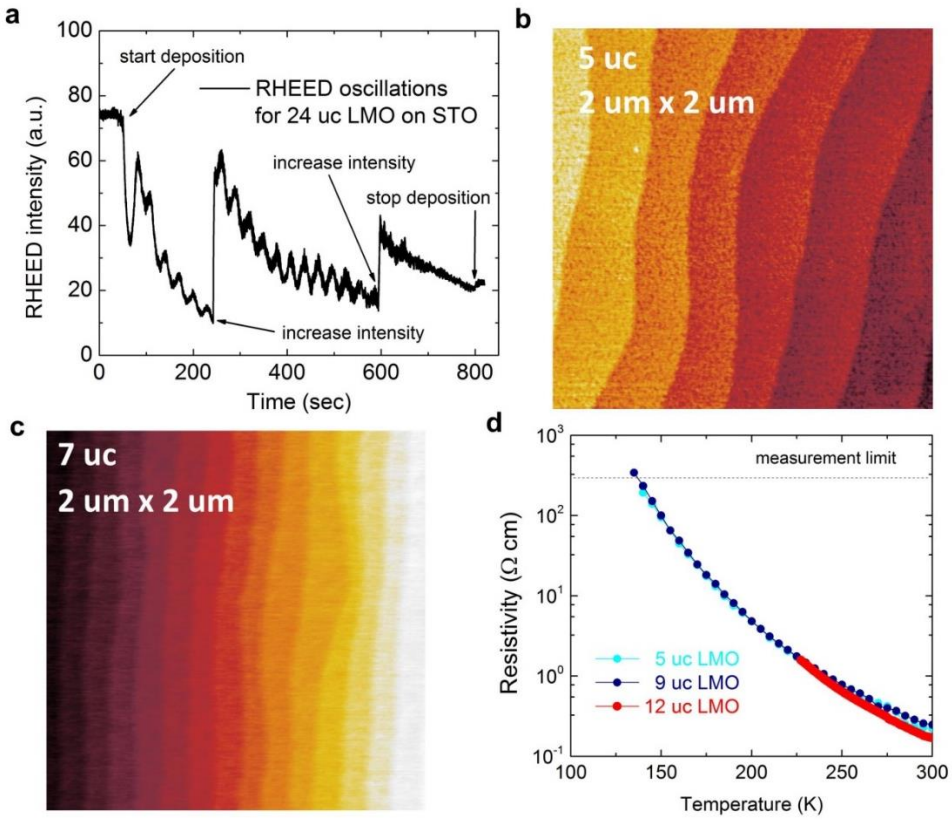

Figure 7.1 Basic characterizations of LMO films. (a) Representative RHEED oscillations obtained during the growth for a 24 uc LMO film on STO. (b,c) Surface morphology (2×2 μm^2) of LMO films with thicknesses of 5 uc (b) and 7 uc (c) measured by atomic force microscopy. Clear atomic terraces are visible. (d) Resistivity of 5 uc, 9 uc and 12 uc LMO on STO as a function of

temperature. All LMO films exhibit insulating behaviors in a temperature range from 2 K to 300 K.

LMO films are coherently strained up to 20 uc, as verified by X-ray diffraction (reciprocal space mapping and θ-2θ scan in **figure 7.2**). The in-plane lattice constants *a* and *b* of LMO film were determined to be the same as that of the STO substrate, confirming coherent growth. Moreover, the (103), (013), (-103), and (0-13) LMO thin film peak positions along out-of-plane direction, Qz, were determined to be the same proving that the LMO unit cell is tetragonal with a = b = 0.3905 nm < c.

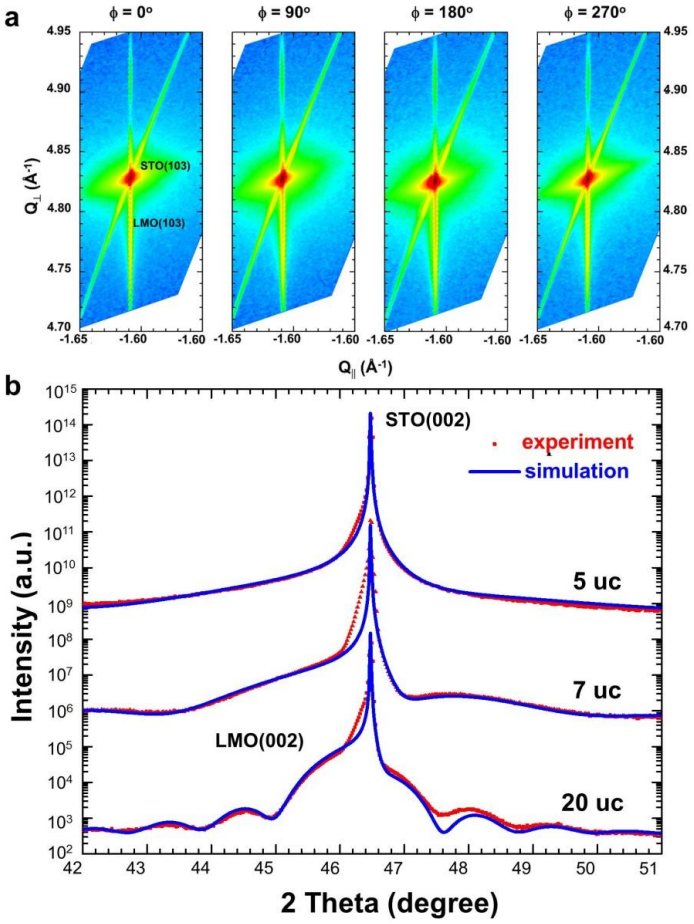

Figure 7.2 X-ray diffraction data of LMO/STO(001) films. (a) reciprocal lattice map around (103) Bragg reflection of 20 uc thick film, indicating coherently strained tetragonal $LaMnO_3$ unit cell with $a = b < c$ and (b) measured and simulated X-ray diffraction profiles around LMO/STO(002) Bragg peaks. Simulation revealed the following out-of-plane LMO lattice parameters: 0.392 nm

for 5 uc, 0.393 nm for 7 uc, 0.394 nm for 20 uc thick films. The in-plane lattice parameter is same as that of the substrate, a_{STO} = 0.3905 nm. Here we used Q = (4π sinθ)/λ, where θ is the Bragg angle and λ = 0.15406 nm.

Bulk magnetic moments were measured by vibrating sample magnetometer with superconducting quantum interference device (VSM-SQUID). The magnetic moments along different orientations shown were measured on samples with smaller areas of 4 mm^2. In order to measure both in-plane and out-of-plane magnetization on the same sample, the sample had to be cut to fit the measurement chamber of the vibrating sample magnetometer. Then magnetic moments along different orientations as a function of temperature were measured using the same measurement procedure. In order to quantitatively compare the magnetic moments, the magnetic moments were normalized to a 5 × 5 mm^2 area. Local magnetic domains were imaged by scanning-SQUID microscopy, with a SQUID pick up loop scanning across the sample surface. Compared from bulk measurement, it can visualize the magnetic domains and also eliminate possible artificial signal from substrates.

7.2 Abrupt magnetic phase transition at 6 uc LMO thickness

The distribution of local magnetic stray field emanating from the LMO films was imaged by scanning superconducting quantum interference device (SQUID) microscopy, abbreviated to SSM, in zero applied field at 4.2 K. The essential part of the SSM is the square pickup loop with an inner size of ~ 3 × 5 μm^2 (**figure 7.3a**). During the measurement, the loop was scanned ~ 2 μm above the sample surface at a contact angle of approximately 10 º. The SSM records the variation of magnetic flux threading the pickup loop and the flux is converted to magnetic field by dividing by the effective pickup area of ~ 15 μm^2. The typical flux-sensitivity of the SSM is around 14 $\mu\Phi_0 Hz^{-1/2}$, where $\Phi_0 = 2\times10^{-15}$ Tm^2 is the flux quantum and the bandwidth is 1000 Hz. Since our SSM sensor has a 10 ºinclination, the measured magnetic stray field component, denoted as B_z, is almost

perpendicular the sample surface. The SSM images are *x*-*y* maps of the magnetic field-values (which are converted to a color scale). The practical sensitivity during measurements set by external noise sources is estimated to be about 30 nT.

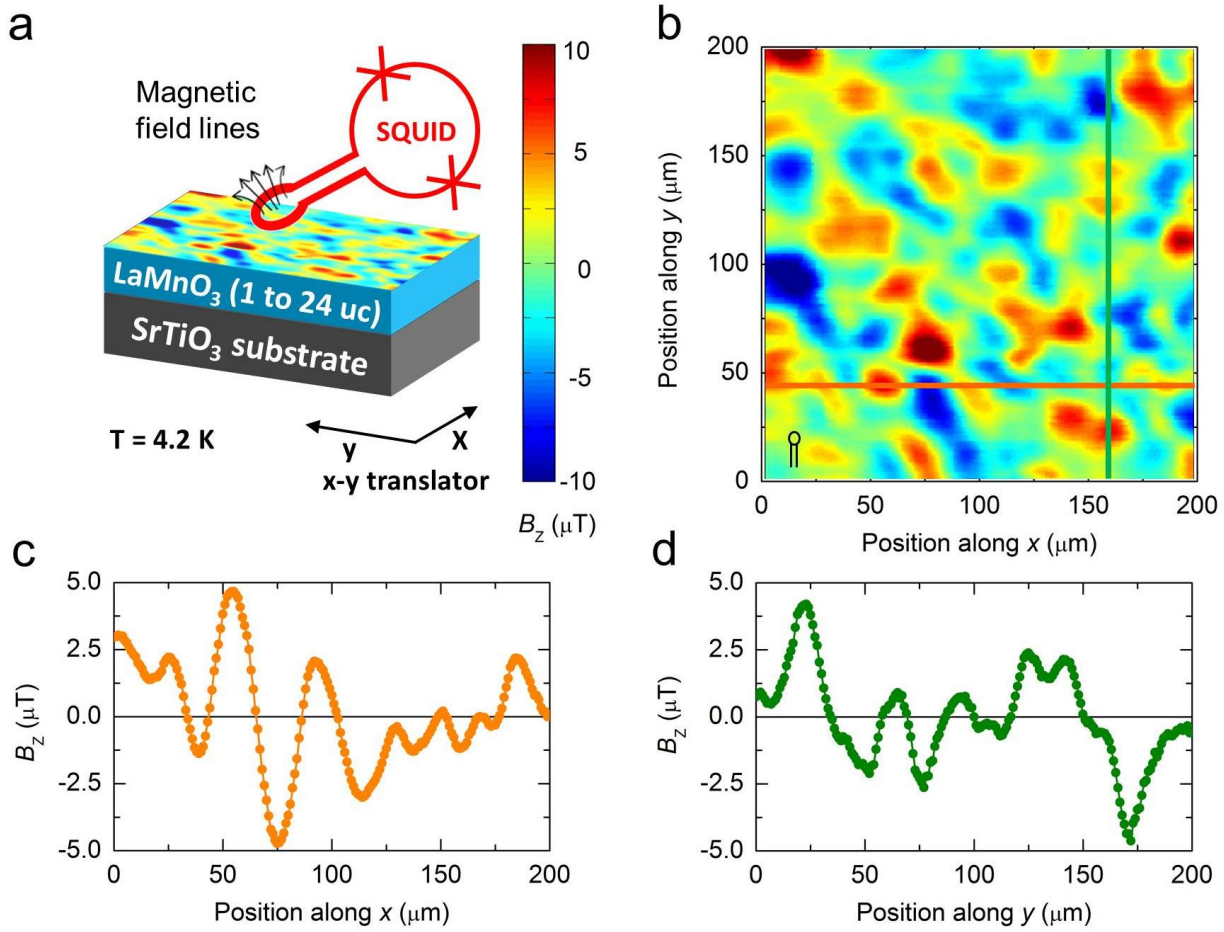

Figure 7.3 Scanning SQUID Microscopy on a 6 uc LMO film on a STO substrate. (a) Schematic drawing of the microscopy technique with sketch of the pickup loop (red). (b) Image of the inhomogeneous stray field distribution of a 6 uc LMO film at 4.2 K. The red-yellow peaks in the two-dimensional color map indicate regions where the magnetic stray field exits the sample, and the blue peaks indicate regions where the magnetic stray field enters into the sample. The scan direction is always horizontally from left to right. A sketch (black) in the bottom-left corner of (b) indicates the size of the pickup loop. (c, d), *x*- (c) and *y*-direction (d) magnetic profiles for the corresponding lines in (b).

Figure 7.3b shows a typical scan of a 200 × 200 μm^2 area of a 6 uc LMO film grown on STO, with a pixel size of 1 × 1 μm^2. The cooling and measurement were both performed in zero applied

field. An irregular pattern of regions with opposite magnetic field orientation was found, presenting a direct image of magnetic field emanating from ferromagnetic domains in the LMO. In **figure 7.3c and 7.3d**, the local magnitude variations along two orthogonal directions are presented.

Figure 7.4 shows that a monolayer-sharp transition to ferromagnetism occurs at a critical thickness of 6 uc. **Figures 7.4 a-d** indicate that the characteristic domain size evolution with thickness above the critical value. The SSM signals for films with a thickness smaller than the critical value (**figure 7.4e-f**) are uniformly much weaker and cannot be resolved; they are two orders of magnitude smaller than the typical root-mean-square (RMS) values of the thicker films. The images for films below the critical thickness are shown on a color scale of one order more sensitivity than that used for the ferromagnetic films. The critical thickness for ferromagnetism was confirmed by SSM measurements on another set of samples fabricated in a different growth chamber. Since a uniform and controllable ferromagnetic state is necessary for device application, the observed critical thickness for ferromagnetism is of particular significance. Huijben *et al.*[173] and Xia *et al*. [174] have reported a critical thickness for ferromagnetism in Sr doped LMO and $SrRuO_3$ thin films using bulk sensitive techniques. However, due to the lack of domain structure information, characteristics and origin of the transition remain unclear. Using the SSM, Kalisky *et al.*[175] performed a comprehensive imaging study of magnetic structures in the interface between $LaAlO_3$ and STO below and above the critical thickness for ferromagnetism at the interface, and they observed magnetic patches above the critical thickness. However, there has been no previous report of an abrupt magnetic transition in which direct imaging confirms that the whole film switches to a ferromagnetic state.

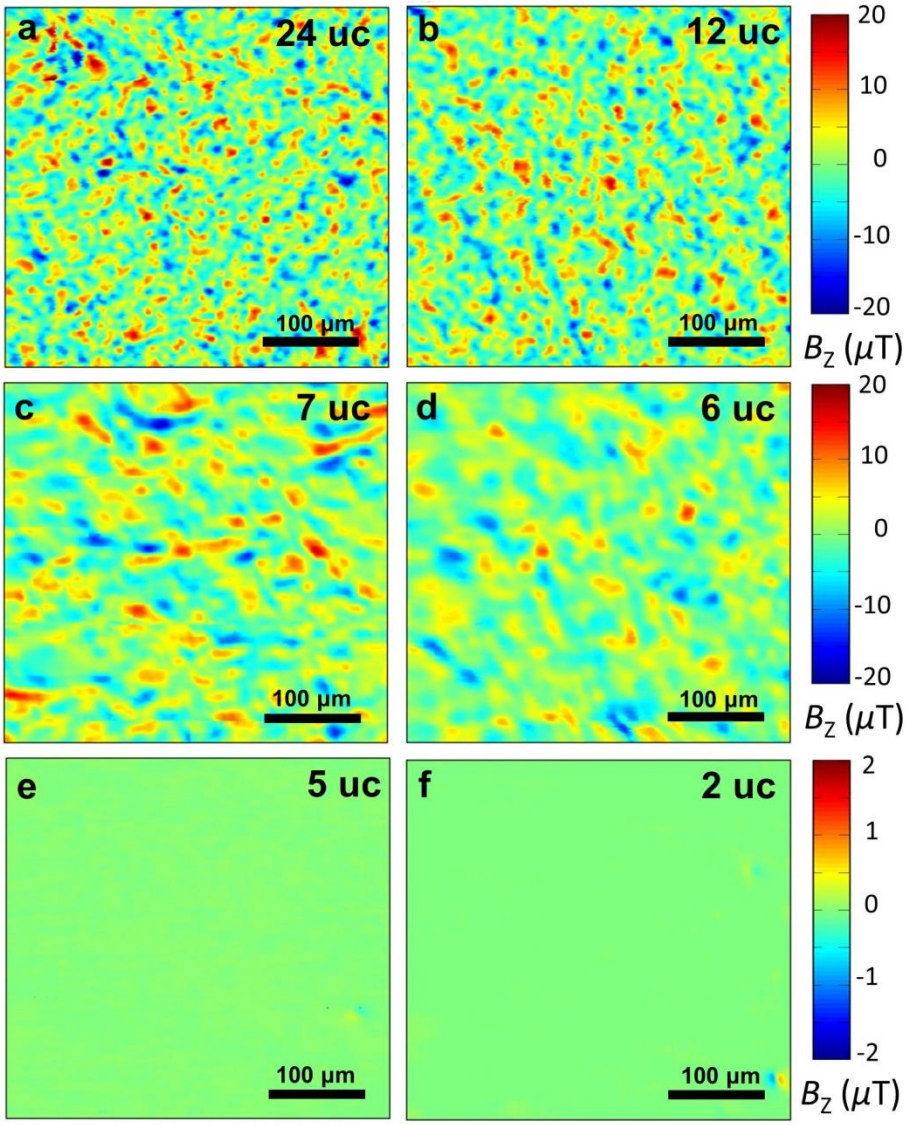

Figure 7.4 Critical thickness for ferromagnetism in insulating LMO (001) films grown on STO substrates. (a-d) Images of magnetic field emanating from LMO films with a thickness of (a) 24 uc, (b) 12 uc, (c) 7 uc and (d) 6 uc, respectively. (e, f) Absence of magnetic field for 5 uc (e) and 2 uc (f) LMO. The scale of color bars for 5 uc and 2 uc LMO are one order smaller than those of the other images.

To find out whether the ferromagnetism is indeed solely dependent on the LMO thickness, we fabricated and measured a sample that consisted partly of a 5 uc-thick and partly of a 7 uc-thick LMO film. The sample was prepared by first growing the 5 uc LMO film, and then covering half of the surface with a shadow mask while 2 extra uc of LMO were grown on the exposed surface. As seen from **figure 7.5a**, the 5 uc area exhibits no SSM signal within the noise level and the 7 uc

area reveals an inhomogeneous magnetic field distribution comparable to the regular 7 uc LMO films (see **figure 7.4c**). To give a semi-quantitative evaluation of the magnetization strength of LMO with different thicknesses, we calculated the root-mean-square (RMS) value from each SSM image. **Figure 7.5b** compares RMS values of the SSM signal for films with different thicknesses. As seen, the difference in magnetic field value of films with thicknesses below and above the critical thickness is about two orders. This experiment demonstrates the ability to modify the magnetic properties of this oxide compound by the controllable addition of 0.8 nm of the same material.

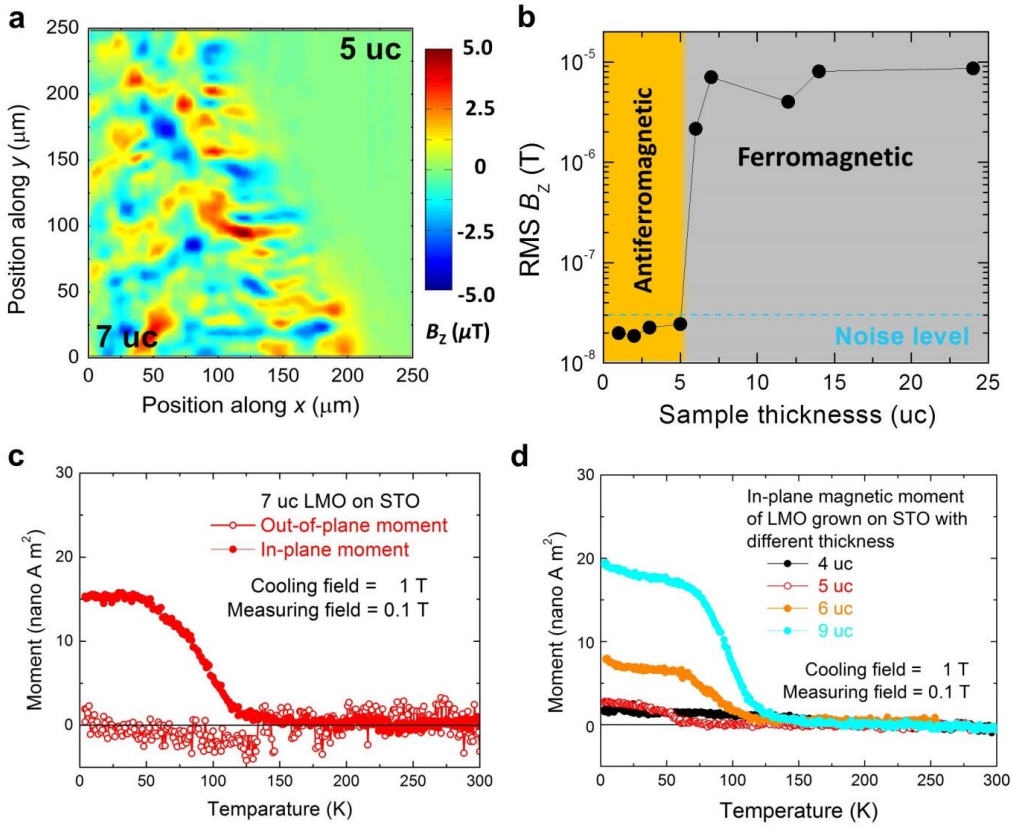

Figure 7.5 Abrupt appearance of in-plane ferromagnetism. (a) The upper-right area is the area where 5 uc LMO was grown and the bottom-left area is covered by 7 uc LMO. (b) RMS values of magnetic field for films with different thicknesses. (c) In-plane and out-of-plane magnetic moments of 7 uc LMO grown on STO. The magnetic moment of 7 uc of LMO is found to lie in-plane. (d) Magnetic moment of 4 uc, 5 uc, 6 uc and 9 uc LMO films grown on STO as a function of temperature.

The magnetization orientation of the ferromagnetic LMO films was determined by measuring the magnetization of a 7 uc LMO film grown on STO along different orientations using a VSM-SQUID. During the measurement, the sample is first cooled in a 1 Tesla magnetic field and the moment is measured during warm up in 0.1 Tesla. **Figure 7.5c** shows the temperature dependent magnetic moments of a 7 uc LMO film along two different orientations, revealing the in-plane nature of the magnetization. Therefore, the magnetic field pattern imaged by SSM is due to in-plane ferromagnetism. Magnetic moment as a function of temperature was also measured for LMO films with different thicknesses using the same procedure. As shown in **figure 7.5d**, 4 uc and 5 uc LMO films show no clear sign of a magnetic moment, indicating an antiferromagnetic or a nonmagnetic state. Since these thinner films show no sign of either ferromagnetism or Curie-law paramagnetism in bulk magnetic measurements, yet strong magnetic moments on the Mn sites are still expected to be present, it is highly probable that the thin LMO films are antiferromagnetic, similar to the bulk. Furthermore, the absence of an uncompensated magnetic moment in LMO films with an odd number of unit cells less than 6 uc, for example 5uc, suggests antiferromagnetic order within (001) planes, rather than the planar antiferromagnetism that is found in the bulk.

For confirmation the critical thickness for the transition, more bulk magnetic properties were carried out by VSM-SQUID. **Figure 7.6a** shows a comparison of the magnetic moments of a STO substrate and a 5 uc LMO film grown on a STO substrate. The "STO substrate" stands for a blank STO substrate, which went through the temperature and pressure process of film deposition, but skipped film deposition. The signals solely from the STO substrate and from the 5 uc LMO film (below the critical thickness for ferromagnetism) grown on STO are both close to 3×10^{-9} Am^2 (or

3 nAm^2). This clearly shows that the additional magnetic moment from the 5 uc LMO film is less than 1 x 10^{-9} Am^2.

A small hysteretic signal is also measured in the blank substrate (see **figure 7.6b**). There are three possible sources, namely an artifact due to residual magnetic field while switching the superconducting magnet in the vibrating sample magnetometer, contaminations during sample transfer from the deposition chamber to the magnetometer and/or contamination from the back side of the substrate. The residual field source is explained in the instrument note [177] and the contamination issue is discussed in the literature, e.g. silver paint [178].

As shown in **figure 7.6c**, the addition of a 6th uc of LMO gives rise to an increase in magnetic moment to values larger than 10 × 10^{-9} Am^2. Therefore, the magnetic transition at the critical thickness measured by the vibrating sample magnetometer is at least one order of magnitude. **Figure 7.6d** shows the thickness dependence of the saturation moment of LMO measured at 10 K. As can be seen, the saturation moment has an average value of ~1.6 μB/Mn.

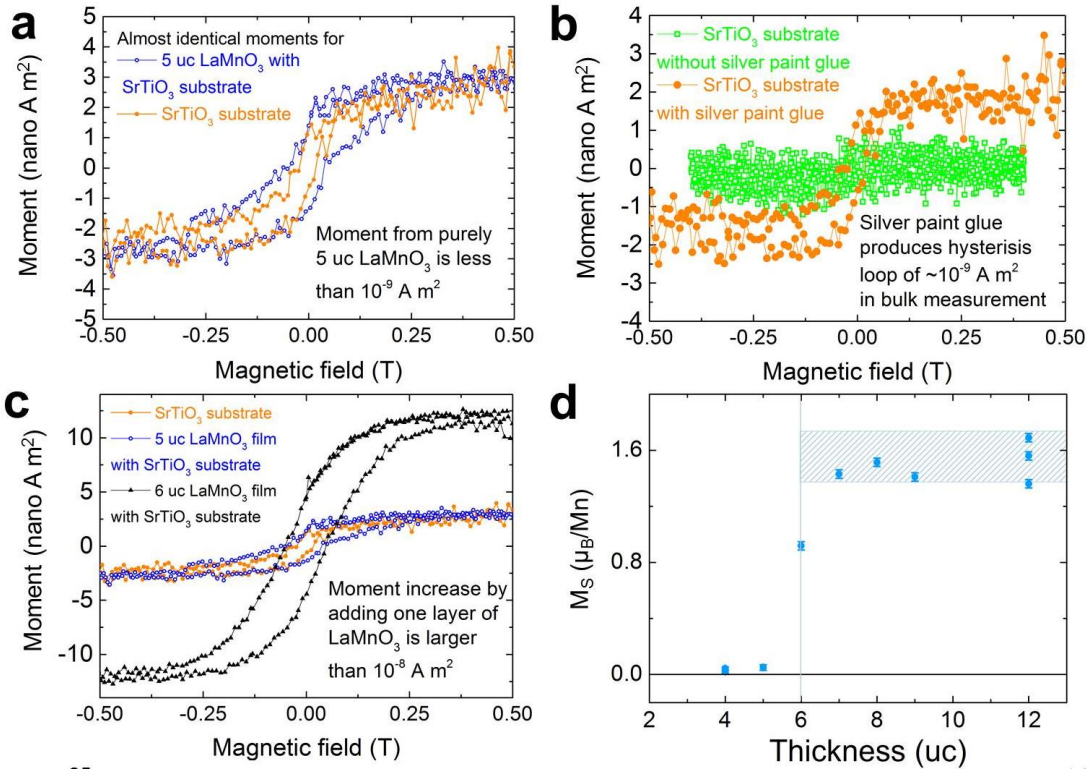

Figure 7.6 Bulk magnetic properties of the LMO films. (a) Almost identical in-plane magnetization curves for STO substrate and 5 uc LMO grown on STO. The moment from 5 uc LMO is less than 10^{-9} Am^2. (b) Comparison of vibrating sample magnetometer data on $SrTiO_3$ with and without silver paint. (c) M(H) hysteresis loops for 6 uc LMO grown on STO, 5 uc LMO on STO and solely STO substrate. The moment increase by adding one layer of LMO is about 10×10^{-9} Am^2. (d) Thickness dependence on the saturation magnetic moment at 10 K of LMO/STO heterojunctions.

7.3 Origins of the magnetic transition

Because of the abruptness of the phase transition and the similarity in polar properties of LMO (001) and LAO (001) films, it is relevant to consider possible electronic reconstruction, which has been proposed as the mechanism for the abrupt insulator-to-metal transition in the well-studied LAO/STO case [65]. LMO contains alternatively charged $(LaO)^{1+}$ and $(MnO_2)^{1-}$ layers resulting in an internal electric field E_0. A simple first order estimate for this field is $E_o = e/2A\varepsilon_o\varepsilon_r$; where e is the electronic charge, A is the unit cell area, ε_o is the permittivity of vacuum and ε_r is the dielectric

constant of LMO. Taking $\varepsilon_r \sim 70$ at low temperature [179], the value of E_0 is 0.85 eV/nm and it shears both the valence and conduction bands (see **figure 7.7a**). The band gap (E_g) in bulk LMO (about 1.3 eV [180]) is smaller than that in bulk STO (3.2 eV), and therefore charge transfer to eliminate the polar discontinuity occurs entirely within the polar LMO film. This is quite unlike LAO/STO where the larger band gap of LAO (5.6 eV) ensures that the electrons are transferred to the STO side of the interface. At a certain thickness $t_c = E_g/E_o \approx 4$ uc (1.53 nm), the valence band maximum of the LMO reaches the conduction band minimum at the LMO/STO interface, initiating electron transfer from the top to the bottom of the LMO film. Such transfer then decreases the electric field in LMO. The transferred charge as a function of thickness is zero below t_c, and increases asymptotically with increasing thickness to $0.5e$ [181]. The electron transfer therefore makes the interface region of LMO electron-doped and the top surface region of LMO hole-doped. This is analogous to the electronic phase separation in bulk manganites [182, 183], which in our case is stabilized by an intrinsic electric field of the polar LMO film. The doping of LMO tilts the exchange interaction between Mn ions from superexchange to double exchange and leads to ferromagnetism when a sufficient number of electrons are available. Our density-functional calculations predict that both electron and hole doping of LMO increases the relative energy difference between the antiferromagnetic and ferromagnetic ground states, in agreement with the experimentally reported bulk phase diagram of LMO [95, 182, 183]. Thus, it is confirmed that electronic reconstruction will favour ferromagnetism above a certain critical thickness of LMO. We note that, contrary to the LAO/STO system, where the interface becomes metallic above the critical thickness, our films remain insulating. This is due to the difference in band gap between LAO and LMO. The large band gap of LAO leads to electron transfer to STO, whereas in the LMO/STO case the electronic reconstruction results in the self-doping of LMO. The self-doping

picture is also consistent with a previously reported unaltered Ti^{4+} valence state in $La_{1-x}Sr_xMnO_3$/STO heterojunctions [95].

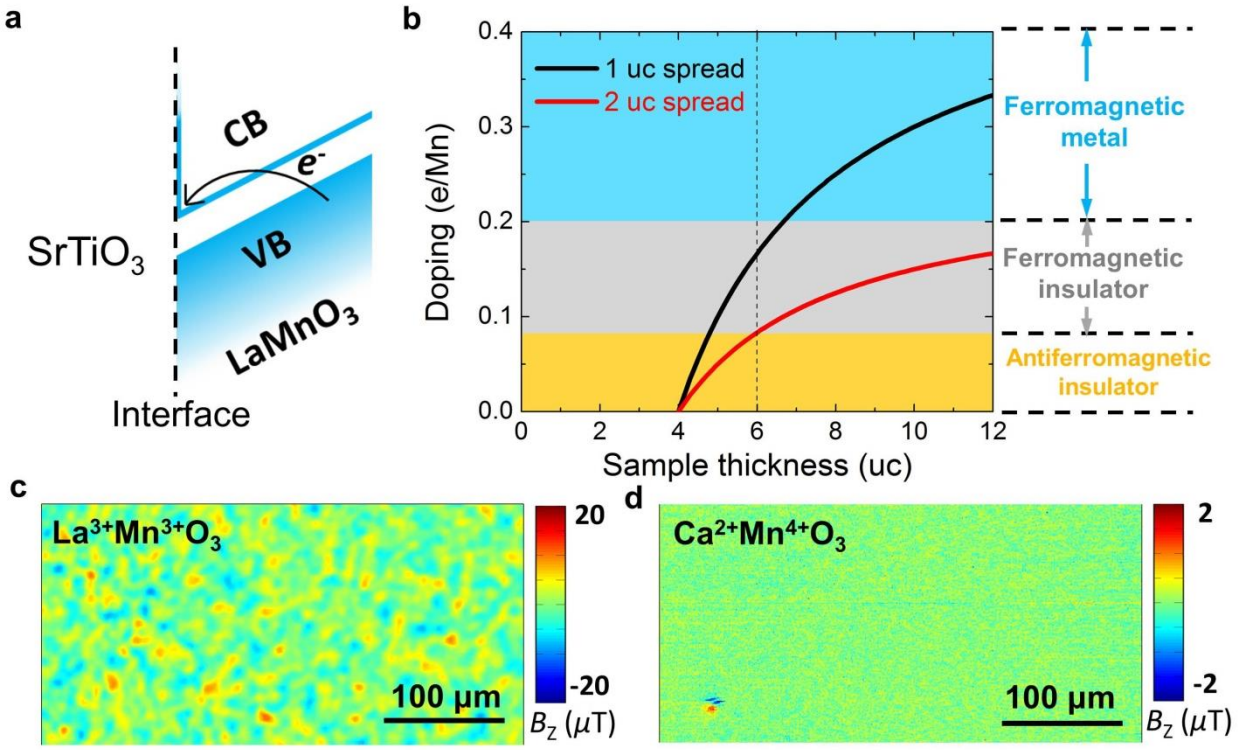

Figure 7.7 Analysis of the origin of ferromagnetism in LMO. (a) Band diagram of electronic reconstruction for LMO (001) film grown on an STO substrate. (b) Amount of charge on the Mn site transferred from surface to interfacial layers as a function of LMO thickness. The black curve corresponds to the doping level where all the charge is projected onto just one uc and the red curve corresponds to the doping level when the charge is spread over 2 uc. The three doping regimes corresponding to the ferromagnetic conducting state (blue area), the ferromagnetic insulating state (grey area) and the antiferromagnetic insulating state (orange area) are adapted from literature for doped bulk LMO. (c) SSM image of 12 uc $La^{3+}Mn^{3+}O_3$ showing ferromagnetic behavior. (d) SSM image of 12 uc $Ca^{2+}Mn^{4+}O_3$ shows no sign of ferromagnetic behavior.

The exact thickness at which the ferromagnetism occurs depends on the spread of the charge. **Figure 7.7b** shows an estimated doping charge per Mn atom when all the charge is projected onto just one uc (black curve) and when the charge is spread over two uc (red curve). We see that in the latter case the bulk phase diagram predicts a phase transition from the insulating antiferromagnetic phase to the insulating ferromagnetic phase when the LMO thickness exceeds 6 uc, which is

consistent with our experimental observations. The assumption of the charge spread over 2 uc agrees with results of first-principles calculations [184] and experimental observations [95] that indicate screening of the interface charge in doped LMO.

In order to verify the feasibility of this electronic reconstruction mechanism, we compared the behavior of 12 uc LMO and $CaMnO_3$ films, since the $Ca^{2+}Mn^{4+}O_3$ (001) film is non-polar. These films were grown on TiO_2-terminated conducting 0.1 wt% Nb-doped STO (Nb:STO) substrates and were covered by 2 uc $LaAlO_3$ under the same growth conditions. The 2 uc $LaAlO_3$ capping layer was used to reveal the effect of surface symmetry breaking, and the conducting Nb:STO substrate was used to investigate interface band-bending. By comparing SSM images between $LaAlO_3$ capped LMO grown on Nb:STO (**figure 7.7c**) and LMO grown on STO (**figure 7.4b**), we conclude that neither the surface symmetry breaking nor band-bending effects contribute to the critical magnetic behavior. Furthermore, as shown in **figure 7.7c and 7.7d**, only the LMO films show the magnetic field patterns, while the non-polar $CaMnO_3$ films show no signature of ferromagnetism. Thus, both our theoretical analysis and experimental data suggest that electronic reconstruction driven by the polar nature of LMO (001) film is a feasible explanation for the abrupt transition to ferromagnetic order in LMO thin films.

7.4 Summary

Summarizing, we have imaged the distribution of the magnetic stray field emanating from insulating LMO films grown on STO substrates. An atomically sharp antiferromagnetic-to-ferromagnetic transition was created and imaged when the LMO film thickness was increased to 6 uc. This critical thickness for uniform ferromagnetism is explained in terms of electronic interface reconstruction, involving electron transfer from the top of the LMO film to the bottom.

Our results demonstrate how emergent functionality, in this case ferromagnetism, can be visualized and engineered at the atomic level.

Chapter 8 Ultrathin $BaTiO_3$ Based Ferroelectric Tunnel Junctions through Interface Engineering

Abstract

In modern electronic devices, 25-55% of the energy is consumed by memory. Current advanced magnetic memories are switched by spin-transfer torque where high current density is required. The ability to change states using voltage in ferroelectric tunnel junctions (FTJs) offers a route for lowering the switching energy of memories. Enhanced Tunneling electroresistance in FTJ can be achieved by asymmetric electrodes or introducing metal-insulator-transition interlayers. However, up to now, the role of each interface in a FTJ is not clearly illustrated. Also, compatibility with integrated circuits (e.g. resistance matching, fatigue) has not been explored adequately. Here we report an incisive study of FTJ performance with varying asymmetry of the electrode/ferroelectric interfaces. Our results prove that band offsets at each interface in the FTJs control the TER ratio. It is found that the off state resistance (R_{Off}) increases much more rapidly with the number of interfaces compared to the on state resistance (R_{On}) leading to large On/Off ratios with increasing number of interfaces. Surprisingly high TER (~ 400%) can be achieved even at $BaTiO_3$ layer thicknesses down to two unit cells (~ 0.8 nm). These results are extremely promising for future low energy memories.

8.1 Role of interfaces in FTJs

As illustrated in chapter 2, a tunnel junction consists of a series of heterojunctions. Each layer has a different electronic band structure. When a heterojunction forms, band bending and depletion layer forms, the extent of band bending and depletion region greatly influence the actual tunnel barrier height and width in addition to the main ferroelectric barrier. For example, TER ratio in

FTJ with structure of Pt/BTO/Nb:$SrTiO_3$ is significantly affected by Nb doping concentration [116]. Yin *et al.*[117] reported a device with the metal-insulator manganite $La_{0.5}Ca_{0.5}MnO_3$ as interlayer in $La_{0.7}Sr_{0.3}MnO_3$/BTO/$La_{0.5}Ca_{0.5}MnO_3$/$La_{0.7}Sr_{0.3}MnO_3$ junction which leads about two orders of magnitude of enhancement of the on/off ratio (R_{off}/R_{on}). However, a comprehensive understanding of the role of band offsets at heterojunctions on the performance of a FTJ is still lacking. Here, we did a systematic study on FTJs from simple to complex device structures aiming to elucidate the role of band offset at each heterojunction within the FTJs. Further, the effect of device size and ferroelectric layer (BTO) thickness were investigated.

8.2 Experimental

FTJs with structures of Pt/BTO (t)/Nb:$SrTiO_3$ (J1-t), Pt/$La_{1-x}Sr_xMnO_3$/BTO/Nb:$SrTiO_3$ (J2-x) and Pt/$La_{0.67}Sr_{0.33}MnO_3$/$La_{1-x}Sr_xMnO_3$/BTO/Nb:$SrTiO_3$ (J3-x) with Sr concentration x ranging from 0.2 to 0.7, were fabricated by pulsed laser deposition (PLD) on (001) oriented Nb:$SrTiO_3$ (NSTO, 0.5 wt % Nb doping) (see **figure 8.1** for schematic structures). In J1-t, t represents the number of uc of BTO layer. BTO (for all FTJs) and $La_{1-x}Sr_xMnO_3$ (for J2-x and J3-x) were deposited on Nb:STO substrates at 750 ℃ with an oxygen partial pressure of 1 mTorr with laser fluence of 1.5 J/cm^2. The growth process was monitored in-situ by reflection high energy electron diffraction (RHEED), which showed a layer-by-layer growth mode. **Figure 8.2a and 8.2b** show examples of a RHEED intensity oscillations for the $BaTiO_3$ (BTO) and $La_{1-x}Sr_xMnO_3$ ($L_{1-x}S_xMO$) with x= 0.2, 0.5 and 0.7 growth process. Streaky RHEED patterns observed after deposition of $L_{1-x}S_xMO$ layer also confirms the growth mode. Thicknesses of the BTO and $La_{1-x}Sr_xMnO_3$ ($L_{1-x}S_xMO$) (x=0.2, 0.33, 0.5, 0.7) intermediate layer are 7 uc and 6 uc, respectively, unless otherwise stated. After BTO (for all FTJs) and $L_{1-x}S_xMO$ (for J2-x and J3-x) depositioin, samples were cooled to room temperature at an oxygen pressure of 500 mTorr. For J3-x, additional 20 nm layer of

$La_{0.67}Sr_{0.33}MnO_3$ was deposited through a shadow mask via PLD on top of $L_{1-x}S_xMO$ layer at 750 ℃ and oxygen pressure of 200 mTorr, followed by same cooling conditions. 50 nm Pt was deposited by magnetron sputtering with different electrode sizes by a photolithography process using an amorphous AlN mask.

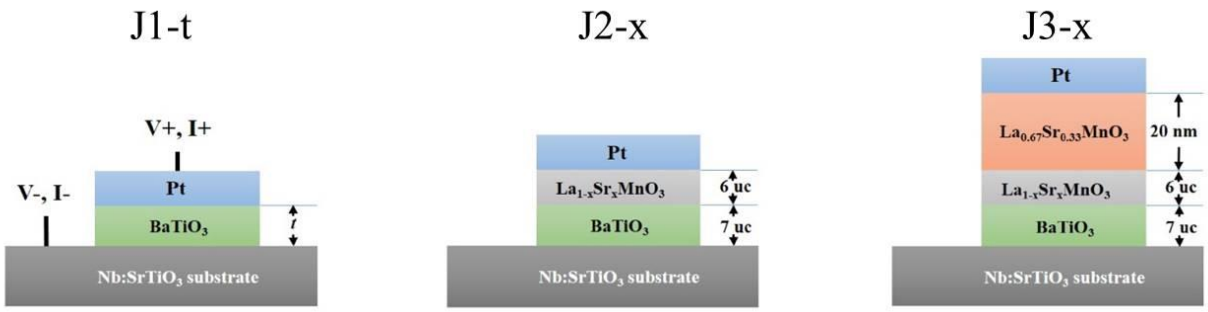

Figure 8.1 Device structures for J1-t, J2-x and J3-x FTJs.

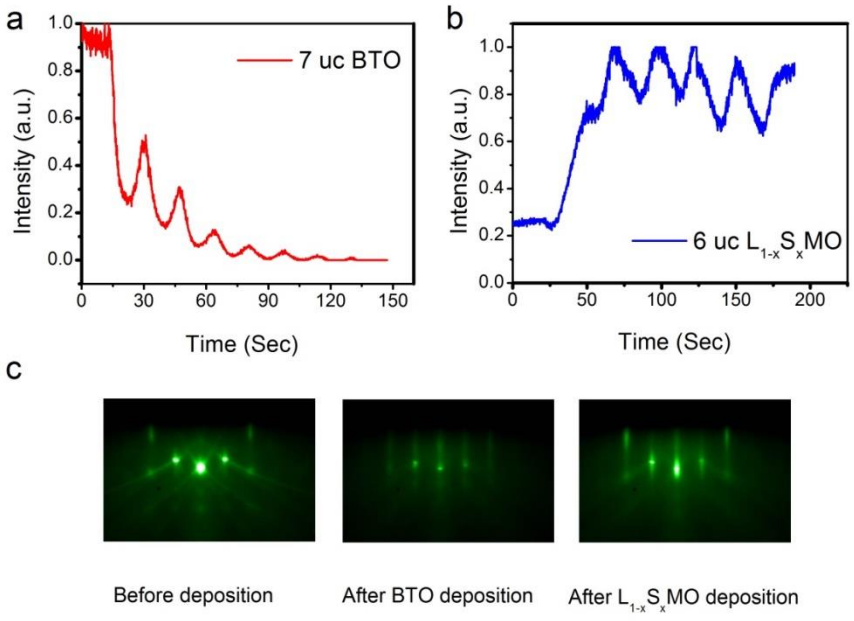

Figure 8.2 Epitaxial growth of the FTJ structures. RHEED Intensity oscillation reveals layer-by-layer growth of 7uc BTO layer in (a) and 6 uc L1-xSxMO in (b). The corresponding RHEED patterns shown in (c) describe the different stages of FTJ fabrication.

A commercial Piezoresponse Force Microscopy (MFP-3D, Asylum Research, US) was used to characterize the local response of the $BaTiO_3$ samples under ambient conditions. During the measurement, an A.C. bias is delivered to the sample surface via a conductive probe (AC240TM, Olympus, Japan) coated with Pt/Ir. The amplitude and phase images represent the strength of the piezoresponse and the polarization orientation (domain pattern) respectively. Polarization switching was observed from the PFM phase image when rescanning the same area.

Electrical measurements were performed by a two-probe method on the junction resistance using a Quantum Design Physical Properties Measurement System (PPMS) integrated with a Keithley 6430 SourceMeter and a 2002 Multimeter. The pulse duration for the write and read operation for all FTJs is 1 ms. There are two primary measurement modes fot the charaterization of FTJs. The first is R-V loop measurement, where reading voltage is fixed at a small voltage (100 mV in our measurements) after the writing voltage (varied writing voltage from 0 to 3 V), the resistance value will be recored. The R-V loop aims to measure the saturation and coercive voltage of the FTJ. The other mode is I-V curve measurements, which normally is done after the stabliztion of saturation state. A write voltage (slightly larger than the saturation voltage, ~ 2 V) complete write the on or off state for a certain FTJ, then sweep a small voltage and measure the tunnel current. I-V curves are very essential to explcitly studies the tunnelling charateristics of the device and determine the tunneling mechanism which has been discussed more detailed in later section.

8.3 Primary properties of BTO and FTJs

First of all, we examined the surface and ferroelectric properties of BTO thin films grown on NSTO. Atomic force microscopy (AFM) of 7 uc BTO film shows atomic terraces (**figure 8.3a**), which is consistent with the layer-by-layer growth mode. **Figure 8.3b** shows ~180 ° phase

difference by piezoresponse force microscopy (PFM) of 7 uc BTO poled by ±5 V. It proves that switchable polarization is present in 7 uc (~ 2.8 nm) BTO thin film. Phase and amplitude bias hysteresis is also observed and shown later (**figure 8.5**) to compare the resistance switching behavior for FTJs.

Secondly, structural qualities are characterized by high-resolution transmission electron microscope (HRTEM) by cross-section imaging. **Figure 8.3c** shows the TEM image of J3-0.5 without a Pt electrode. It shows abrupt atomic interfaces in the different layers and hence demonstrates coherent growth of all oxide layers with controlled thicknesses (consistent with the number of oscillations in **figure 8.2a and 8.2b**).

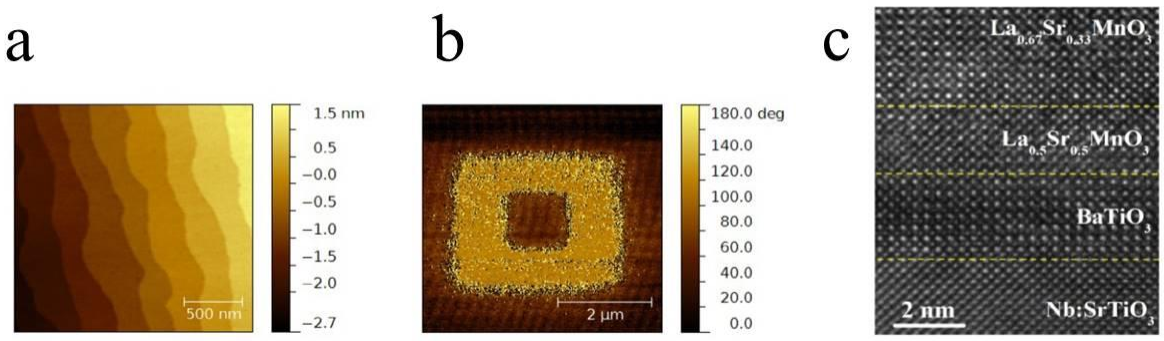

Figure 8.3 Device Structure and Ferroelectric thin film properties (a) AFM image of the 7 uc BTO thin film showing atomic terraces. (b) PFM phase contrast image of 7 uc BTO thin films with poling voltage: the bright area is poled by 5 V and the dark area by -5 V. (c) High resolution TEM image of cross section of the all oxide FTJ of $La_{0.67}Sr_{0.33}MnO_3/L_{0.5}S_{0.5}MO/BTO/NSTO$.

8.3 Memory and switching properties of different structured FTJs

All structured FTJ devices show memory and switching properties. **Figure 8.4** summarizes the major characteristics of J3-0.5 at 10 K. **Figure 8.4a** shows hysteresis loop of the tunneling resistance versus the writing voltage (R-V loop) across the junction at 10 K, which is very similar to the polarization-electric field hysteresis loop with a TER ratio of ~10^3. The microscopic picture

of charge distribution of on/off states is shown in **insets of figure 8.4a**. When the polarization is pointing up, electrons accumulate in $L_{0.5}S_{0.5}MO$ to balance the bound charge adjacent to BTO interface while holes accumulate on the NSTO side, leading to a higher resistive state, the off-state. For the on-state, holes accumulate at $L_{0.5}S_{0.5}MO$ and electrons accumulate in NSTO after reversal of the BTO polarization. Cyclic testing and data retention properties are shown in **figure 8.4b-c**. No obvious degradation on the device TER ratio was seen in a test of up to 500 write/read cycles.

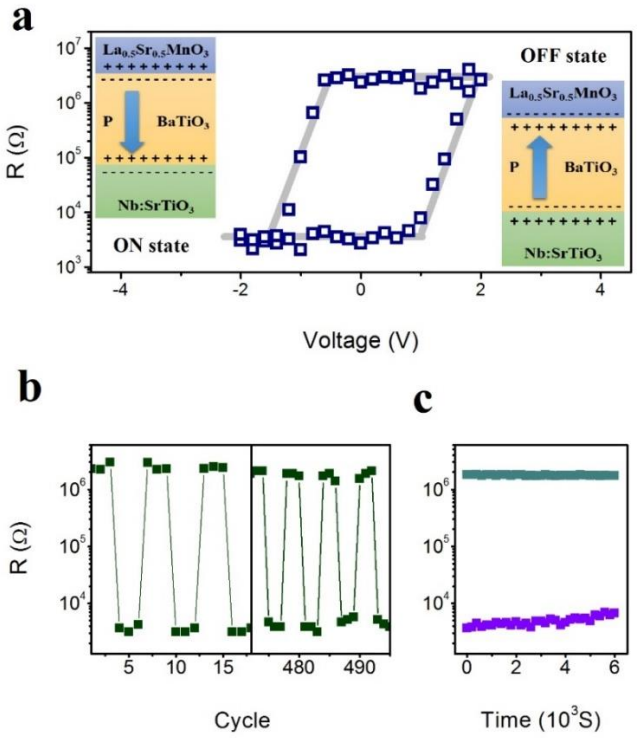

Figure 8.4 Device performance of FTJ with structure of $Pt/L_{0.67}S_{0.33}MO/L_{0.5}S_{0.5}MO/BTO/NSTO$ at 10 K. (a) Resistance voltage hysteresis loop of FTJ. Inset of (a), the schematic representation of charge distribution of the on and off states with respect to the polarization direction. (b) On/Off writing and reading cycles up to 500 cycles. **c**, data retention of FTJs up to 6000 seconds. The pulse duration for the write and read operation is 1 ms.

FTJ resistive switching is caused by the polarization switching of the ferroelectric spacer layer. **Figure 8.5** shows the comparison beteween the J1-7 R-V hysteresis loop from electrical measurement and the phase voltage hysteresis and amplitude loop of 7 uc BTO thin film grown on NSTO substrate from PFM measurement at room temperature. Qualitativelty, the shape of both R-V loop and phase-voltage loop looks very similar. Quantatively, The former (**figure 8.5a**) shows a coercive and saturation voltage of 1.5 and 1.8 V, respectivly; which are amostly identical to the coerive and saturation voltage of the latter (**figure 8.5b**). The consistency of the above two switching hysteresis loop proves that ferroelectric switching of the 7 uc BTO is the origin of the resistance swtiching observed in FTJs (J1-7). Similar R-V loops observed in other FTJs are also originated by the polarization switching of the BTO layers.

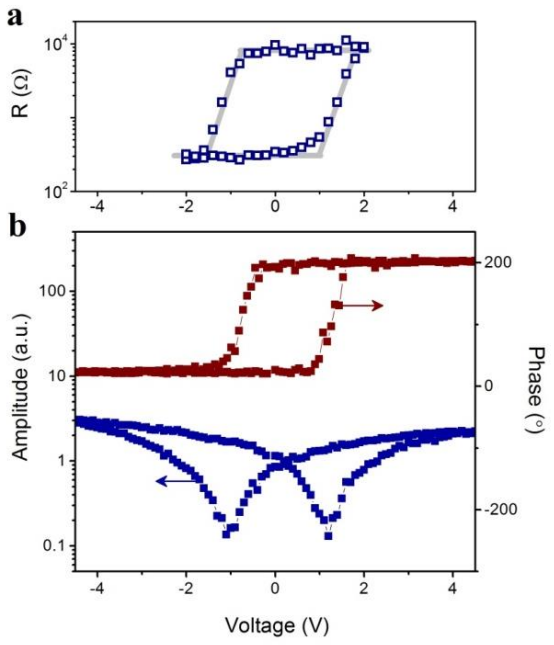

Figure 8.5 Comparison between (a) R-V loop of J1-7 and (b) phase-voltage hysteresis loop of 7 uc BTO thin film from PFM measurement at 300 K. Amplitude-voltage butterfly loop of 7 uc BTO film is also persented in (b).

The TER ratio and the R_{On} and R_{Off} differ a lot in various structured FTJs. R-V loops of J1-7, J2-0.7 and J3-0.7 (**figure 8.6a**) demonstrate that the TER ratio is improved significantly with the insertion of the intermediate layer of $L_{0.3}S_{0.7}MO$ and the electrode modifier layer of $L_{0.67}S_{0.33}MO$. While TER ratios improve significantly, the basic switching properties remain unaltered. As shown in **figure 8.6b**, saturation and coercive voltages of all FTJs are 1.8 and 1.5 V, respectively. Hence the primary switching in FTJs is completely dominated by the BTO layer, and is *unaffected* by the intermediate or electrode layers. Almost the entire voltage drop is across the BTO.

In **figure 8.6c**, R_{On} and R_{Off} are summarized for three different types of FTJs, including the Sr concentration effect in the intermediate layer. With addition of an intermediate layer, both R_{On} and R_{Off} increase, however the R_{Off} increases more. As a result, the TER ratio increases by about one order of magnitude. With introduction of the additional $L_{0.67}S_{0.33}MO$ layer, the TER ratio is enhanced by another order of magnitude. In summary, the more layers that are integrated in the FTJ, the higher the TER ratio.

In J2-x, even though R_{On} and R_{Off} depend exponentially on the Sr concentration, their increase is small when compared to the effect of increasing the number of interfaces. The same Sr concentration dependence trend applies for J3-x. One exception is J3-0.33, where $L_{1-x}S_xMO$/ $L_{0.67}S_{0.33}MO$ the interface creates a homojunction, thereby the TER ratio is much smaller than that of x = 0.2, 0.5 and 0.7.

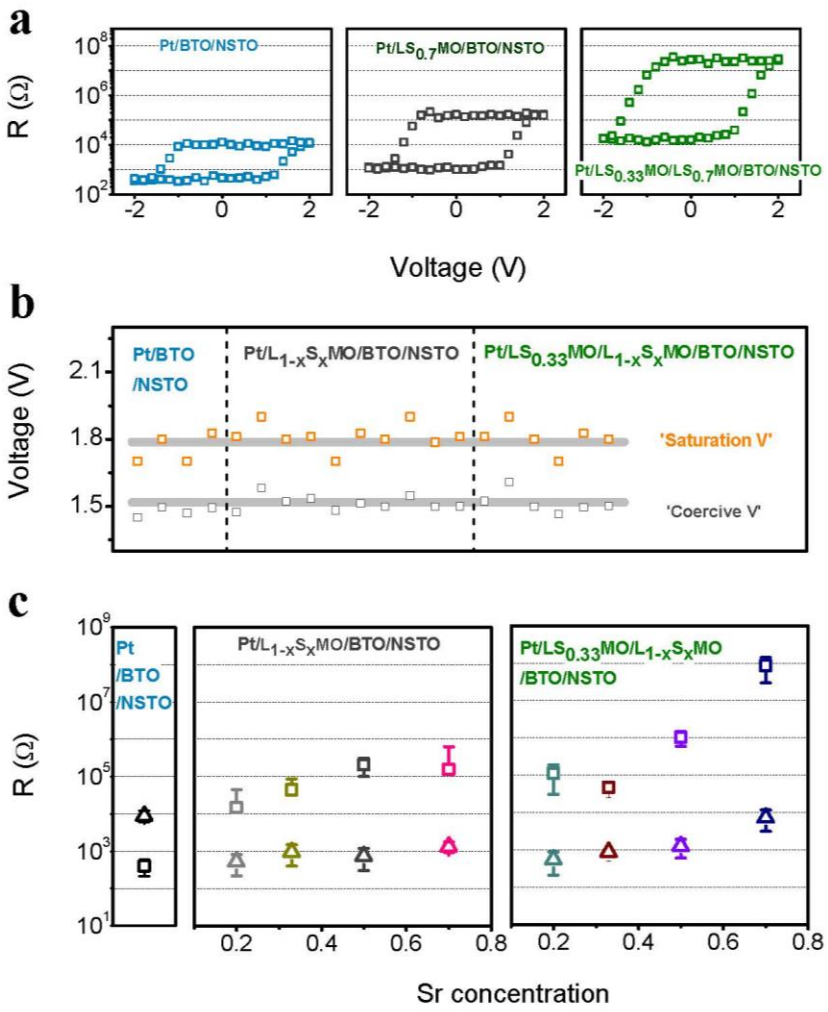

Figure 8.6 Performance at 10 K of FTJs with different structures. (a) Resistance voltage hysteresis loops for FTJ structures of Pt/BTO/NSTO, Pt/$L_{0.3}S_{0.7}$MO /BTO/NSTO and Pt/ $L_{0.67}S_{0.33}$MO/$L_{0.3}S_{0.7}$MO/BTO/NSTO. (b) The saturation and coercive voltages of all three types of FTJs with 7 uc BTO. In J2 and J3 FTJs, Sr concentration (x=0.2, 0.33, 0.5 and 0.7) in intermediate $L_{1-x}S_xMO$ does not affect both voltages. (c) R_{On} and R_{Off} of FTJs of Pt/BTO/NSTO (J1), Pt/$L_{1-x}S_xMO$ (Sr=0.2, 0.33, 0.5, and 0.7)/BTO/NSTO (J2) and Pt/$La_{0.67}Sr_{0.33}MnO_3$/$L_{1-x}S_xMO$ (Sr=0.2, 0.33, 0.5 and 0.7) /BTO/NSTO (J3). R_{on} and R_{off} show dependence on Sr concentration in J2 and J3.

8.4 Band offset effect in FTJ performances via theoretical simulation

To understand the different performances among FTJs, the I-V of all FTJs are fitted by theoretical tunnel currents across a trapezoidal barrier potential profile [109] (see **figure 8.7**).

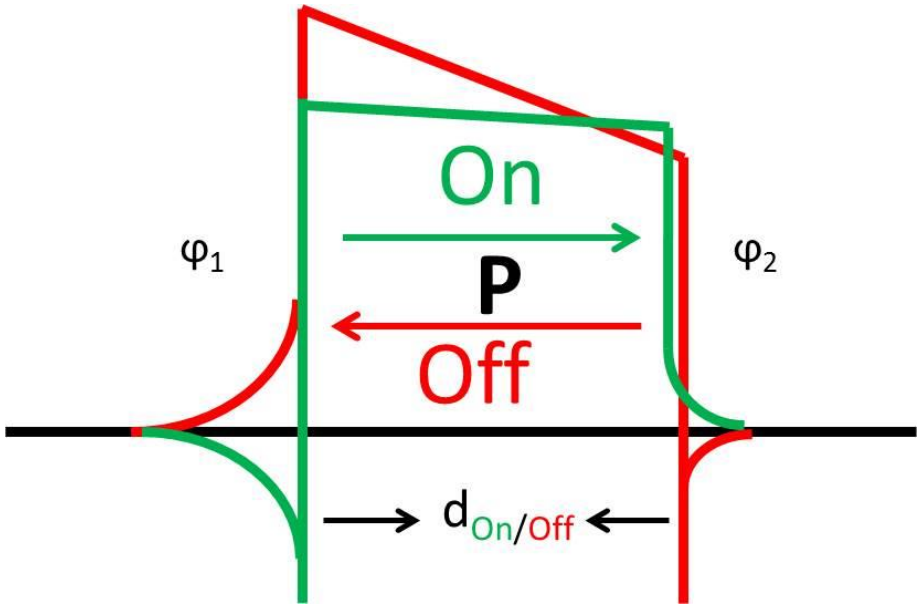

Figure 8.7 Schematic representation of trapezoidal barrier potential profile with barrier heights (denoted as φ_1 and φ_2) and width defined as d. Red color profiles represents off state and green profile represents the on state. Both barrier heights and width are different for on and off states.

J2 and J3 I-V curves can be fitted by the Brinkerman's model with asymmetrical tunnel barriers with equation [109] of

$$J \cong -\frac{4em}{9\pi^2\hbar^3}\frac{exp\left\{\alpha(V)\left[\left(\varphi_2-\frac{eV}{2}\right)^{3/2}-\left(\varphi_1+\frac{eV}{2}\right)^{3/2}\right]\right\}}{\alpha^2(V)\left[\left(\varphi_2-\frac{eV}{2}\right)^{1/2}-\left(\varphi_1+\frac{eV}{2}\right)^{1/2}\right]} \times \sinh\left\{\frac{3}{2}\alpha(V)\left[\left(\varphi_2-\frac{eV}{2}\right)^{1/2}-\left(\varphi_1+\frac{eV}{2}\right)^{1/2}\right]\frac{eV}{2}\right\}$$

eq 8.1

where $\alpha(V) = 4t(2m)^{1/2}/[3\hbar(\varphi_1 + eV - \varphi_2)]$, m is the effective electron mass, assumed to be the elementray electron mass for the sake of simplicy, φ_1 and φ_2 are the potential barrier height at the $L_{1-x}S_xMO$ (Pt) /BTO and BTO/NSTO interfaces, repectively. Tunnel barrier width is denoted as t, and e and $\hbar$ are the electron charge and reduced Plank constant, respectively.

Figure 8.8 shows the examples of fitting of the both on and off states of J2-0.7, J3-0.2 and J2-0.5. Fitted barrier height and width have been tabulated in **table 8.1**. The fitted barrier heights generally

are consistent with previously fitting results with BTO as the tunnel barrier heights [109, 185]. The new feature we have included are that the tunneling width are fitted as a variable for on and off states due to the effect of the space charge region createad by the semiconductor electrode NSTO. The fitted barrier heights (on-state and off-state φ_1 monotonic depedence on Sr concentration in J3) show that the barrier shape asymmetry increases more when Sr deviates more from x=0.33. It has been reported that the chemical potential (~ Fermi level) of $L_{1-x}S_xMO$ is monotonically dependent on Sr concentration [186]. With one electrode fixed as the $L_{0.67}S_{0.33}MO$ in J3, the observed correlation between the barrier asymmetry with Sr concentration provides strong evidence that *band offsets at the interfaces within the tunnel junctions are the crucial parameter*.

For J1 and J2 devices (except J2-0.7), I-V curves shows almost Ohmic transport properties under a small bias as illustrated as **figure 8.9**, which is the result of a trapezoidal barrier potential approaches to a rectangular barrier potential, i.e. $\varphi_1 - \varphi_2 \ll (\varphi_1 + \varphi_2)/2$. This has been evident from as in J3-0.2 for the on state, $\varphi_1 - \varphi_2 = 0.14$ eV much smaller than the average potential height of 0.64 eV. For J2 and J1, due to decreased asymmetry, more rectangular potential profile are expected. In this case, I-V curves can be described as [109]

$J \approx \frac{e^2}{h}\frac{1}{2\pi t}\frac{\sqrt{2m\bar{\varphi}}}{\hbar} exp\left(-2\frac{\sqrt{2m\bar{\varphi}}}{\hbar}t\right)V$, where $\bar{\varphi} = \frac{\varphi_1+\varphi_2}{2}$, and other parameters are previously defined. The lower asymmetry in barrier potential shape in J1 and J2 is consistent with the observed smaller TER ratio.

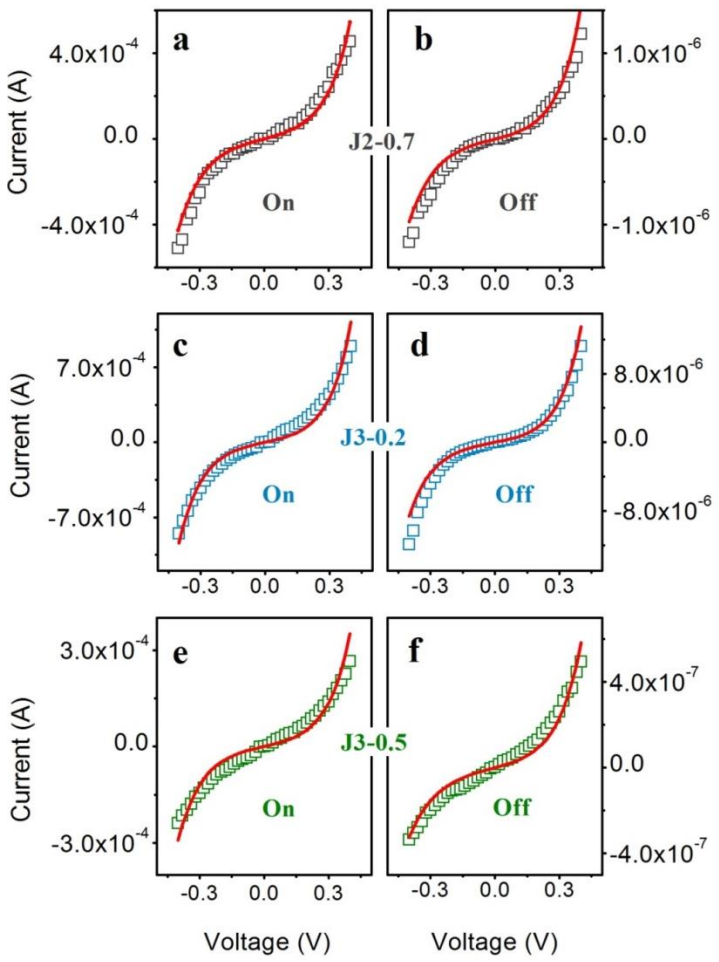

Figure 8.8 I-V curves fitting by Brinkerman's model over a trapezoidal barrier potential profile for J2-0.7, J3-0.2 and J3-0.5 FTJs for both on and off states at 10 K and junction area of 10^4 μm^2. Open squares are the experimental data points and the read solid curves are the optimized fitted curve.

Table 8.1 Tunnel barrier heights and widths fitted by Brinkerman's Model for J2-0.7, J3-0.2, J3-0.5 and J3-0.7 FTJs I-V curves at 10 K.

Junction			**OFF**				**ON**	
	t (nm)	φ_1 (eV)	φ_2 (eV)	Adjusted r^2	t (nm)	φ_1 (eV)	φ_2 (eV)	Adjusted r^2
J2-0.7	3.01	1.22	0.55	0.94	2.79	0.90	0.63	0.95
J3-0.2	2.99	1.00	0.54	0.95	2.79	0.71	0.57	0.97
J3-0.5	2.95	1.44	0.54	0.97	2.83	0.80	0.62	0.95
J3-0.7	3.05	1.72	0.69	0.96	2.78	0.90	0.81	0.95

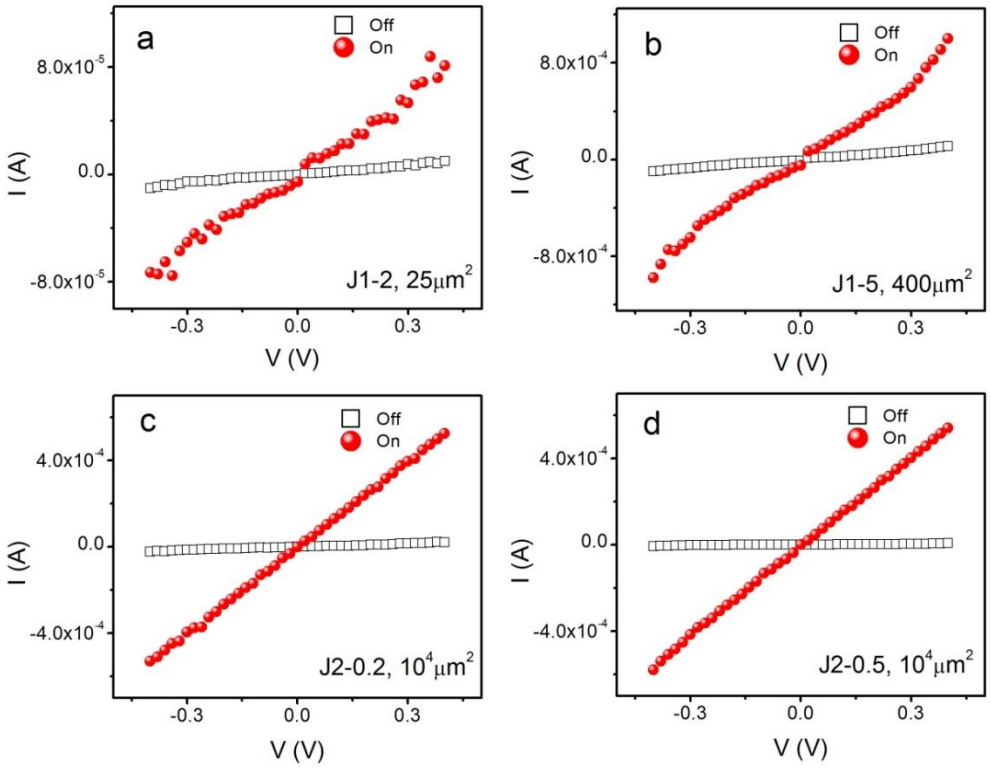

Figure 8.9 Sample I-V curves of Junction J1 and J2 devices at 10 K shows Ohmic transport behavior under a small bias.

8.5 BTO thickness and device size effect

Comparison of characteristics between different structured FTJs, shows TER ratio increases significantly with the number of interfaces. However, the other trend is also observed that both R_{On} and R_{Off} increase significantly. In short, insertion of additional layers increases the TER ratio at the expense of increased junction resistance.

From a practical point of view, the TER ratio required for memory purposes depends upon its statistical variation in the device performance. As seen in **figure 8.10**, there is a distribution of the resistance both in on and off states. The minimum requirement is that the two resistance distribution ranges do not overlap. A huge TER, like ~10^3, far exceeds the requirement. For example, a commercial MTJ device only shows TMR of about 100 %.

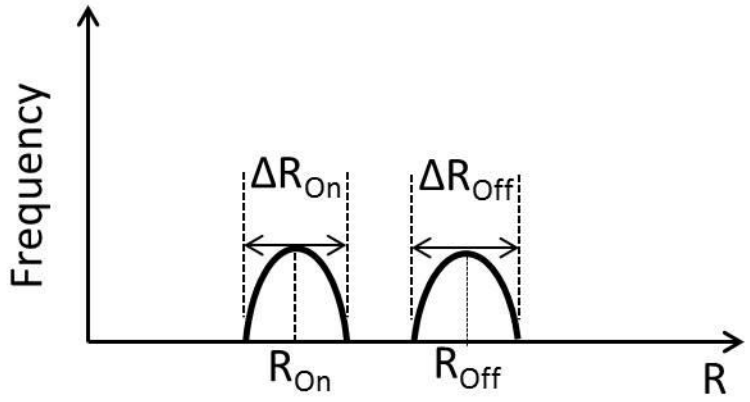

Figure 8.10 A simple histogram of resistance for memory devices.

On the other hand, the resistance area product (RA) is extremely important for integration with CMOS electronics in a 1 transistor-1 FTJ memory cell, which is the most probable architecture. The value of $R_{On}A$ of the simplest FTJ, J1-7, is 5 MΩ μm^2, much larger than the value of 10 Ω μm^2 required for matching the impedance of the transistor, which is typically the order of kΩ.

Considering the fact that TER exceeding the requirement and $R_{on}A$ not matching the requirements, a natural approach is to make a trade off by lowering TER to reach an acceptable value of $R_{on}A$. Hence we reduced the BTO thickness in J1 to realize the compromise, also the device size effect were also studied.

Figure 8.11a shows the optical and schematic image of J1 with top electrode area defined by AlN assisted photolithography. The BTO thickness t ranges from1 to 7 uc and the square top electrode length d is 5, 10, 20 or 50 μm. For the 50 μm electrode, J1-7 shows a good R-V loop at room temperature, but J1-2 does not. However, when d is reduced from 50 to 5 μm, the R-V loop at room temperature is restored for J1-2 (**figure 8.11b**). This effect can be attributed to a lower probability of finding a defect center in an FTJ with a smaller size. The less rectangular R-V loop in J1-2 compared to J1-7 is most likely due to the fact that 2 uc is very close to the intrinsic limit for stable ferroelectricity in BTO [99, 187] at room temperature. J1-2 shows similar R-V to that of J1-7 strongly support that our 2 uc BTO is ferroelectric at room temperature, which exclude other possible effects showing the R-V loop. To the best of our knowledge, this is the *first* report on 2 uc BTO with large TER (~ 400%) observed in FTJs. J1-1 showed no switching behavior down to an electrode size of 5 μm; studies of smaller device dimensions and direct ferroelectricity measurement on 1 uc BTO films will be conducted in the future.

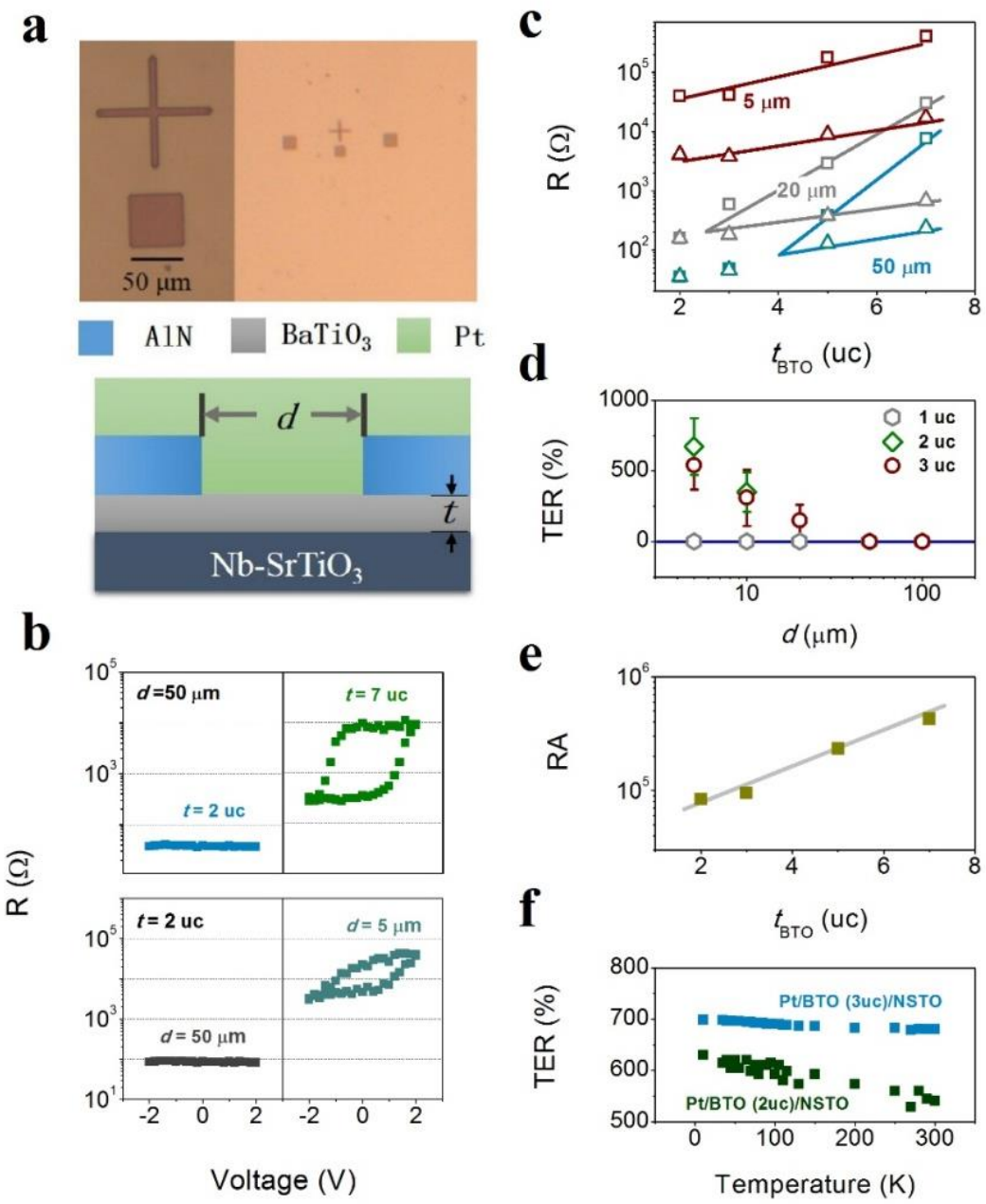

Figure 8.11 Electrode size and ferroelectric layer thickness on Pt/BTO/NSTO (J1-t) structured FTJ performance at T=300 K. (a) optical image on the FTJ with defined top electrode size and schematic image of the cross section of a FTJ device. (b) J1-7 shows normal switching properties but not in J1-2 at a fix electrode size of d=50 μm and FTJ with 2 uc BTO shows normal switching behavior with electrode size of d=5 μm but not with electrode size of 50 μm. (c) On and off state resistance of FTJ with BTO thickness ranged from 2 to 7 uc with different electrode sizes. (d) TER ratio of FTJs with 1, 2 and 3 uc BTO thickness dependence on the electrode size ranged from d=5 to 50 μm. (e) On state RA value dependence on the BTO thickness for all functional FTJs. (f) Weak temperature dependence of TER ratio are observed in J1-2 and J1-3.

Figure 8.11c shows R_{On} and R_{Off} of J1-t with t= 2, 3, 5 and 7 at room temperature. R_{On} and R_{Off} dependence on BTO thickness can be fitted by

$$R_{(On/Off)} = R_{0(On/Off)} \exp(\alpha_{(On/Off)} t), \qquad \text{eq 8.2}$$

where $R_{0(On/Off)}$ is the pre-factor and $\alpha_{(On/Off)}$ is the coefficient which is determined by the barrier height. When the R_{On} curve intersects with the fitted R_{Off} curve (i.e. diminished TER), it defines the lower bound of BTO thickness for a fixed electrode size. **Figure 8.11c and d** effectively map out window of the functional FTJ in terms of BTO thickness and device size for our processing conditions.

R_{On} for FTJ with a certain BTO thickness scales inversely with the junction area, so $R_{On}A$ primarily depends on BTO thickness and the resistance of the bottom electrode. $R_{On}A$ values of all functional FTJs shows an exponential dependence on the BTO thickness (**figure 8.11e**). TER ratio of J1-t decreases slightly with increasing temperature (shown in **figure 8.11f**) which is rather different from that of J2 and J3 (shown in **figure 8.12**). A large TER value (~400 %) is maintained at room temperature in J1-2 devices with at least 50% reproducibility (see **figure 8.13**). With the evidence of weak temperature dependence and exponential relationship, we could conclude that direct tunneling is the primary conduction mechanism for J1. For J2 and J3 devices, thermally activated defects in $L_{1-x}S_xMO$ layers are most likely the origin of strong temperature dependence of TER ratio, which is also reported by Yin *et al*.[117]

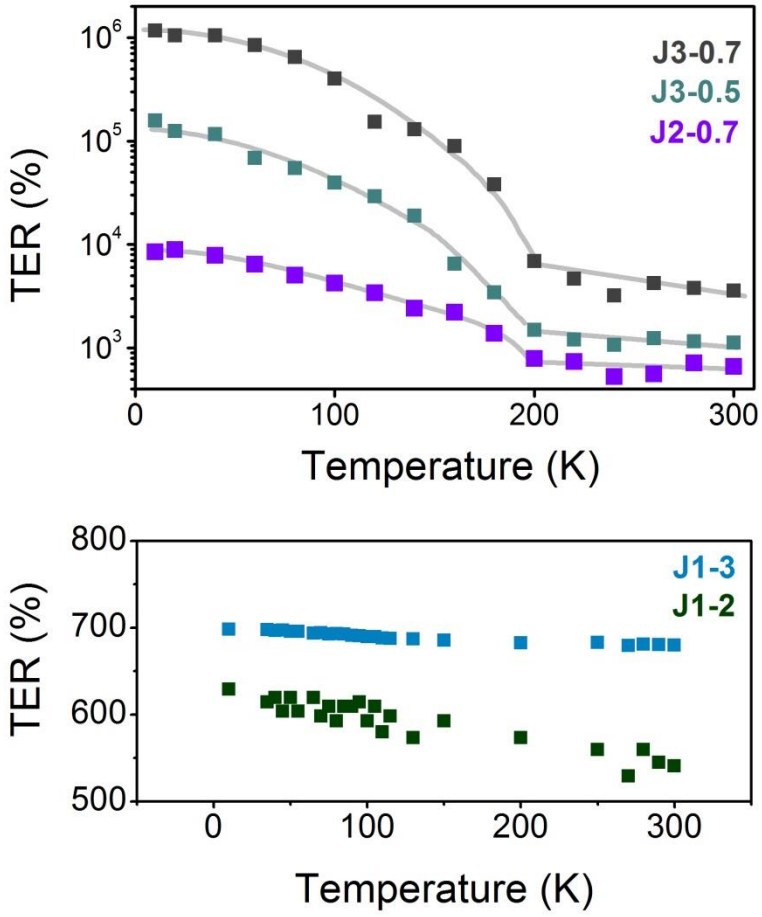

Figure 8.12 Temperature dependent on/off ratio of different types of FTJs. J2 and J3 FTJs show a similar decreasing trend with a transition tempertaure at ~ 200 K, while J1 devices TERs are much less temperature dependent.

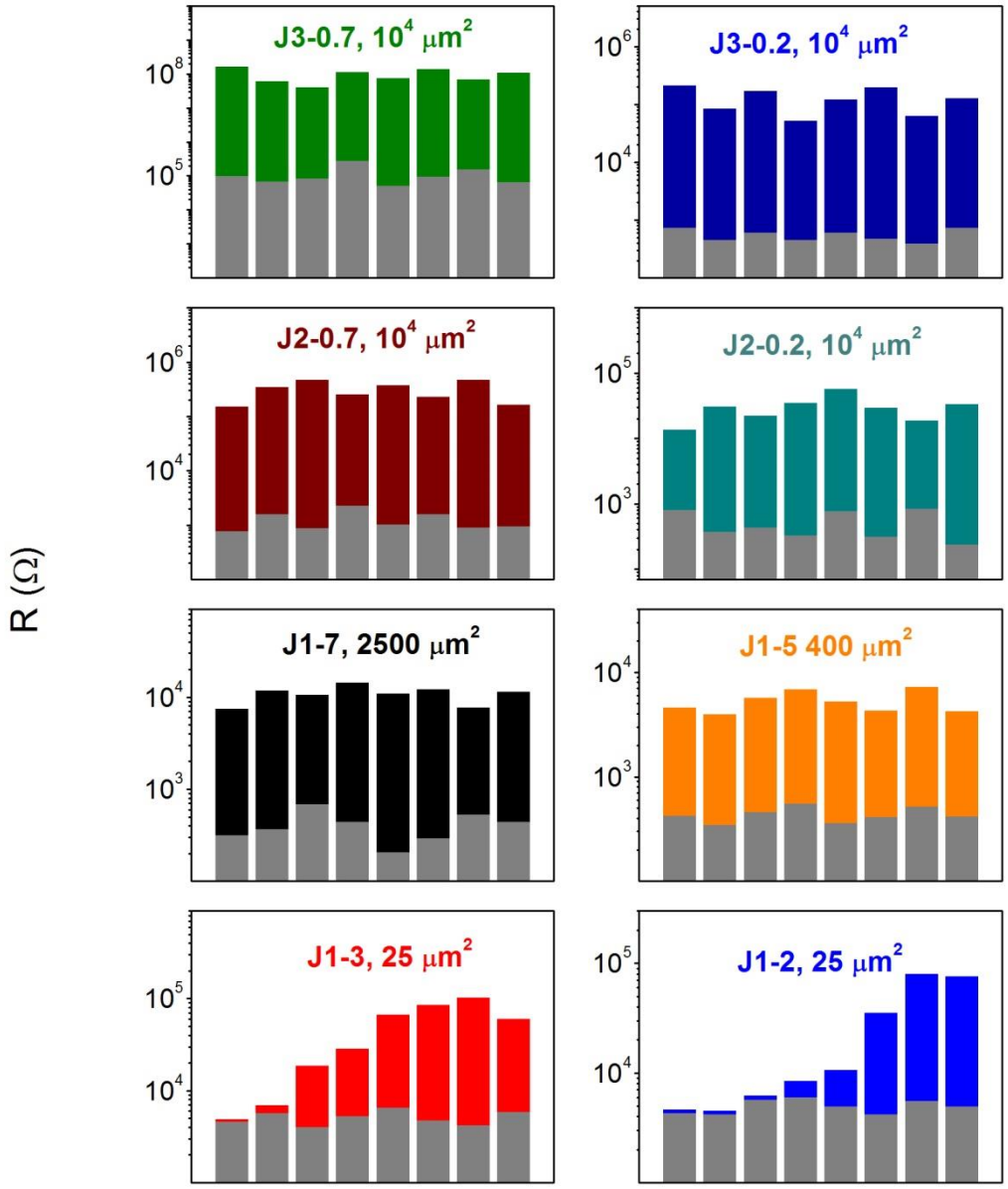

Figure 8.13 On and off state resistance for multiple FTJs, with device area specified. Device performance are more reproducible for BTO thickness equal or larger than 5 uc. However, even for BTO thickness of 2 uc, over 50 % of the FTJs show good switching properties . J2 and J3 are charaterized at 10 K and J1 is charaterized at 300 K.

A lower bound of $R_{on}A$ value of 100 $k\Omega\mu m^2$ is obtained in J1-2 of device area of 25 μm^2 with TER ratio of 400%. Compared to a CoFeB/MgO/CoFeB MTJ with a 1 nm MgO barrier, the TER ratio is better than the TMR ratio but the RA value is much worse (10 $\Omega\mu m^2$ for MTJ device). The problem lies in the poor conductivity of the bottom electrode. The NSTO resistivity is 3 orders of magnitude larger than that of CoFeB (5×10^{-2} versus 5×10^{-5} Ωcm). For further device improvement, more conductive electrodes are needed to lower the RA. However, the large TER realized in these devices utilizes the band bending created at the bottom semiconducting electrode interface. By increasing the metallicity of this electrode TER ratio is likely to be reduced. Ultimately a compromise has to be reached.

8.6 Summary

In summary, introduction of additional heterojunctions in a FTJ is a reliable way to improve the TER ratio of FTJ without changing its primary switching properties. The effect is attributed to the band offset at the heterojunctions within a FTJ device which changes both the barrier width and height for the electron tunneling process. However, the TER enhancement due to incorporation of intermediate layers increases the R_{On} and R_{Off} dramatically, which is bad for impedance matching for nonvolatile memory applications. To solve this problem, BTO thickness is reduced down to two monolayers and TER of 400 % at room temperature in FTJs with a BTO barrier which is only 2 uc (0.8 nm thick) is achieved. The room temperature functional FTJ with such a thin thickness points the way for practical FTJs and it can be competitive with magnetic tunnel junctions. The trade-off between TER and RA value for FTJs would be continuously pursued in future studies.

Chapter 9 Future work

Oxide interfaces, due to the strong correlation between charge, orbital and spin degree of freedom, exhibit multiple interesting phenomena in a single system. We have shown that interface phenomena induced by polar catastrophe not only induced interface conductivity but also interface magnetism. Furthermore, polarization catastrophe and symmetry breaking superlattices are shown to be effective to tune the orbital occupancy to a great extent [188]. Besides polar discontinuity/catastrophe, band offsets are very important to control the TER in an FTJ. There are plenty of future directions to be pursued for better understanding of the oxide interfaces phenomena and possible integration with silicon. I will list a few of them below:

1. Spectroscopic (i.g. X-ray absorption spectroscopy, X-ray magnetic dichroism and x-ray linear dichroism) study of LMO/STO interfaces to gain more insights in to the magnetic transition process and linkage to the orbital occupancy information.
2. Encouraged by the 2 uc FTJ performance at room temperature, it is worthy to test the performance for FTJ with $BaTiO_3$ down to 1 uc, with device reduced to sub 100 nm. Furthermore, the stabilization of the ferroelectricity at such thickness also needs more study.
3. To perform a systematic comparison of the switching behavior between an FTJ and normal resistive switching because normal resistive switching is also expected in an FTJ when the ferroelectric barrier is regarded as a common dielectric barrier. From this study, we can identify processes which are primarily ferroelectric polarization controlled which will be crucial for future device design.

There is a lot more to explore!

REFERENCES

1. Schlom, D.G., et al., *A Thin Film Approach to Engineering Functionality into Oxides.* Journal of the American Ceramic Society, 2008. **91**(8): p. 2429-2454.
2. Norton, D.P., *Synthesis and properties of epitaxial electronic oxide thin-film materials.* Materials Science and Engineering: R: Reports, 2004. **43**(5–6): p. 139-247.
3. Minami, T., *Present status of transparent conducting oxide thin-film development for Indium-Tin-Oxide (ITO) substitutes.* Thin Solid Films, 2008. **516**(17): p. 5822-5828.
4. Ozgur, U., et al., *A comprehensive review of ZnO materials and devices.* Journal of Applied Physics, 2005. **98**(4): p. 041301-103.
5. Ozgur, U., D. Hofstetter, and H. Morkoc, *ZnO Devices and Applications: A Review of Current Status and Future Prospects.* Proceedings of the IEEE, 2010. **98**(7): p. 1255-1268.
6. Yuasa, S., et al., *Giant room-temperature magnetoresistance in single-crystal Fe/MgO/Fe magnetic tunnel junctions.* Nat Mater, 2004. **3**(12): p. 868-871.
7. Ni, M., et al., *A review and recent developments in photocatalytic water-splitting using for hydrogen production.* Renewable and Sustainable Energy Reviews, 2007. **11**(3): p. 401-425.
8. Thiruvenkatachari, R., S. Vigneswaran, and I. Moon, *A review on UV/TiO_2 photocatalytic oxidation process (Journal Review).* Korean Journal of Chemical Engineering, 2008. **25**(1): p. 64-72.
9. Kokubo, T., H.-M. Kim, and M. Kawashita, *Novel bioactive materials with different mechanical properties.* Biomaterials, 2003. **24**(13): p. 2161-2175.
10. Bass, J.D., et al., *Stability of Mesoporous Oxide and Mixed Metal Oxide Materials under Biologically Relevant Conditions.* Chemistry of Materials, 2007. **19**(17): p. 4349-4356.
11. Roop Kumar, R. and M. Wang, *Functionally graded bioactive coatings of hydroxyapatite/titanium oxide composite system.* Materials Letters, 2002. **55**(3): p. 133-137.
12. Sugimoto, W., et al., *Molybdenum Oxide/Carbon Composite Electrodes as Electrochemical Supercapacitors.* Electrochemical and Solid-State Letters, 2001. **4**(9): p. A145-A147.
13. Sakamoto, J.S. and B. Dunn, *Vanadium Oxide-Carbon Nanotube Composite Electrodes for Use in Secondary Lithium Batteries.* Journal of The Electrochemical Society, 2002. **149**(1): p. A26-A30.
14. Chang, J.-K., C.-T. Lin, and W.-T. Tsai, *Manganese oxide/carbon composite electrodes for electrochemical capacitors.* Electrochemistry Communications, 2004. **6**(7): p. 666-671.
15. Grätzel, M., *Dye-sensitized solar cells.* Journal of Photochemistry and Photobiology C: Photochemistry Reviews, 2003. **4**(2): p. 145-153.
16. Li, B., et al., *Review of recent progress in solid-state dye-sensitized solar cells.* Solar Energy Materials and Solar Cells, 2006. **90**(5): p. 549-573.
17. Hwang, H.Y., et al., *Emergent phenomena at oxide interfaces.* Nat Mater, 2012. **11**(2): p. 103-113.
18. Dong, S., et al., *Magnetism, conductivity, and orbital order in $(LaMnO_3)_{2n}/(SrMnO_3)_n$ superlattices.* Physical Review B, 2008. **78**(20): p. 201102.

19. Tsukazaki, A., et al., *Quantum Hall Effect in Polar Oxide Heterostructures.* Science, 2007. **315**(5817): p. 1388-1391.
20. van Wees, B.J., et al., *Quantized conductance of point contacts in a two-dimensional electron gas.* Physical Review Letters, 1988. **60**(9): p. 848-850.
21. Chakhalian, J., et al., *Orbital Reconstruction and Covalent Bonding at an Oxide Interface.* Science, 2007. **318**(5853): p. 1114-1117.
22. Gozar, A., et al., *High-temperature interface superconductivity between metallic and insulating copper oxides.* Nature, 2008. **455**(7214): p. 782-785.
23. Tsymbal, E.Y., et al., *Ferroelectric and multiferroic tunnel junctions.* MRS Bulletin 2011. **37**(02): p. 138-143.
24. Garcia, V., et al., *Ferroelectric Control of Spin Polarization.* Science, 2010. **327**(5969): p. 1106-1110.
25. Yin, Y.W., et al., *Coexistence of tunneling magnetoresistance and electroresistance at room temperature in $La_{0.7}Sr_{0.3}MnO_3$/(Ba, Sr)TiO_3/$La_{0.7}Sr_{0.3}MnO_3$ multiferroic tunnel junctions.* Journal of Applied Physics, 2011. **109**(7): p. 07D915-3.
26. Ohtomo, A. and H.Y. Hwang, *A high-mobility electron gas at the $LaAlO_3$/$SrTiO_3$ heterointerface.* Nature, 2004. **427**(6973): p. 423-426.
27. N.A., *The interface is still the device.* Nat Mater, 2012. **11**(2): p. 91-91.
28. Kroemer, H., *Polar-on-nonpolar epitaxy.* Journal of Crystal Growth, 1987. **81**(1–4): p. 193-204.
29. Harrison, W.A., et al., *Polar heterojunction interfaces.* Physical Review B, 1978. **18**(8): p. 4402-4410.
30. Kawasaki, M., et al., *Atomic Control of the $SrTiO_3$ Crystal Surface.* Science, 1994. **266**(5190): p. 1540-1542.
31. Ohnishi, T., et al., *A-site layer terminated perovskite substrate: $NdGaO_3$.* Applied Physics Letters, 1999. **74**(17): p. 2531-2533.
32. Bae, H.-j., et al., *Surface treatment for forming unit-cell steps on the (001) $KTaO_3$ substrate surface.* Applied Surface Science, 2005. **241**(3–4): p. 271-278.
33. Fujimoto, M., et al., *Microstructure and Electrical Properties of Sodium-Diffused and Potassium-Diffused $SrTiO_3$ Barrier-Layer Capacitors Exhibiting Varistor Behavior.* Journal of the American Ceramic Society, 1985. **68**(11): p. C-300-C-303.
34. Gerblinger, J. and H. Meixner, *Fast oxygen sensors based on sputtered strontium titanate.* Sensors and Actuators B: Chemical, 1991. **4**(1–2): p. 99-102.
35. Kawai, M., S. Watanabe, and T. Hanada, *Molecular beam epitaxy of $Bi_2Sr_2CuO_x$ and $Bi_2Sr_2Ca_{0.85}Sr_{0.15}Cu_2O_x$ ultra thin films at 300 ℃.* Journal of Crystal Growth, 1991. **112**(4): p. 745-752.
36. Lytle, F.W., *X-Ray Diffractometry of Low-Temperature Phase Transformations in Strontium Titanate.* Journal of Applied Physics, 1964. **35**(7): p. 2212-2215.
37. Tosatti, E. and R. Martoňák, *Rotational melting in displacive quantum paraelectrics.* Solid State Communications, 1994. **92**(1–2): p. 167-180.
38. Mishra, S.K. and D. Pandey, *Low temperature x-ray diffraction study of the phase transitions in $Sr_{1-x}Ca_xTiO_3$ (x = 0.02,0.04): Evidence for ferrielectric ordering.* Applied Physics Letters, 2009. **95**(23): p. 232910-3.
39. Baer, W.S., *Free-Carrier Absorption in Reduced $SrTiO_3$.* Physical Review, 1966. **144**(2): p. 734-738.

40. Wild, R.L., E.M. Rockar, and J.C. Smith, *Thermochromism and Electrical Conductivity in Doped $SrTiO_3$.* Physical Review B, 1973. **8**(8): p. 3828-3835.
41. Yamada, H. and G.R. Miller, *Point defects in reduced strontium titanate.* Journal of Solid State Chemistry, 1973. **6**(1): p. 169-177.
42. Lee, C., J. Destry, and J.L. Brebner, *Optical absorption and transport in semiconducting $SrTiO_3$.* Physical Review B, 1975. **11**(6): p. 2299-2310.
43. Kan, D., et al., *Blue-light emission at room temperature from Ar^+-irradiated $SrTiO_3$.* Nat Mater, 2005. **4**(11): p. 816-819.
44. Moschizuki, S., F. Fujishiro, and S. Minami, *Photoluminescence and reversible photo-induced spectral change of $SrTiO_3$.* Journal of Physics: Condensed Matter, 2005. **17**.
45. Lotnyk, A., S. Senz, and D. Hesse, *Epitaxial growth of TiO_2 thin films on $SrTiO_3$, $LaAlO_3$ and yttria-stabilized zirconia substrates by electron beam evaporation.* Thin Solid Films, 2007. **515**(7–8): p. 3439-3447.
46. Chrosch, J. and E.K.H. Salje, *Temperature dependence of the domain wall width in $LaAlO_3$.* Journal of Applied Physics, 1999. **85**(2): p. 722-727.
47. Hayward, S.A., S.A.T. Redfern, and E.K.H. Salje, *Order parameter saturation in $LaAlO_3$.* Journal of Physics: Condensed Matter, 2002. **14**.
48. Thiel, S., et al., *Tunable Quasi-Two-Dimensional Electron Gases in Oxide Heterostructures.* Science, 2006. **313**(5795): p. 1942-1945.
49. Reyren, N., et al., *Superconducting Interfaces Between Insulating Oxides.* Science, 2007. **317**(5842): p. 1196-1199.
50. Caviglia, A.D., et al., *Electric field control of the $LaAlO_3/SrTiO_3$ interface ground state.* Nature, 2008. **456**(7222): p. 624-627.
51. Brinkman, A., et al., *Magnetic effects at the interface between non-magnetic oxides.* Nat Mater, 2007. **6**(7): p. 493-496.
52. Ariando, et al., *Electronic phase separation at the $LaAlO_3/SrTiO_3$ interface.* Nature Communications, 2010. **2**.
53. Dikin, D.A., et al., *Coexistence of Superconductivity and Ferromagnetism in Two Dimensions.* Physical Review Letters, 2011. **107**(5): p. 056802.
54. Li, L., et al., *Coexistence of magnetic order and two-dimensional superconductivity at $LaAlO_3/SrTiO_3$ interfaces.* Nat Phys, 2011. **7**(10): p. 762-766.
55. Bert, J.A., et al., *Direct imaging of the coexistence of ferromagnetism and superconductivity at the $LaAlO_3/SrTiO_3$ interface.* Nat Phys, 2011. **7**(10): p. 767-771.
56. Jany, R., et al., *Diodes with breakdown voltages enhanced by the metal-insulator transition of $LaAlO_3$--$SrTiO_3$ interfaces.* Applied Physics Letters, 2010. **96**(18): p. 183504-3.
57. Cen, C., et al., *Oxide Nanoelectronics on Demand.* Science, 2009. **323**(5917): p. 1026-1030.
58. Cen, C., et al., *Nanoscale control of an interfacial metal-insulator transition at room temperature.* Nat Mater, 2008. **7**(4): p. 298-302.
59. Cheng, G., et al., *Sketched oxide single-electron transistor.* Nat Nano, 2011. **6**(6): p. 343-347.
60. Irvin, P., et al., *Rewritable nanoscale oxide photodetector.* Nat Photon, 2010. **4**(12): p. 849-852.
61. Irvin, P., et al., *Anomalous High Mobility in $LaAlO_3/SrTiO_3$ Nanowires.* Nano Letters, 2013. **13**(2): p. 364-368.

62. Schneider, C.W., et al., *Microlithography of electron gases formed at interfaces in oxide heterostructures.* Applied Physics Letters, 2006. **89**(12): p. 122101-3.
63. Park, J.W., et al., *Creation of a two-dimensional electron gas at an oxide interface on silicon.* Nat Commun, 2010. **1**: p. 94.
64. Schlom, D.G. and J. Mannhart, *Oxide electronics: Interface takes charge over Si.* Nat Mater, 2011. **10**(3): p. 168-169.
65. Nakagawa, N., H.Y. Hwang, and D.A. Muller, *Why some interfaces cannot be sharp.* Nat Mater, 2006. **5**(3): p. 204-209.
66. Popović, Z.S., S. Satpathy, and R.M. Martin, *Origin of the Two-Dimensional Electron Gas Carrier Density at the $LaAlO_3$ on $SrTiO_3$ Interface.* Physical Review Letters, 2008. **101**(25): p. 256801.
67. Pentcheva, R. and W.E. Pickett, *Avoiding the Polarization Catastrophe in $LaAlO_3$ Overlayers on $SrTiO_3$ (001) through Polar Distortion.* Physical Review Letters, 2009. **102**(10): p. 107602.
68. Annadi, A., et al., *Electronic correlation and strain effects at the interfaces between polar and nonpolar complex oxides.* Physical Review B, 2012. **86**(8): p. 085450.
69. Perna, P., et al., *Conducting interfaces between band insulating oxides: The $LaGaO_3/SrTiO_3$ heterostructure.* Applied Physics Letters, 2010. **97**(15): p. 152111-3.
70. Li, D.F., Y. Wang, and J.Y. Dai, *Tunable electronic transport properties of $DyScO_3/SrTiO_3$ polar heterointerface.* Applied Physics Letters, 2011. **98**(12): p. 122108.
71. Hotta, Y., T. Susaki, and H.Y. Hwang, *Polar Discontinuity Doping of the $LaVO_3$ /$SrTiO_3$ Interface.* Physical Review Letters, 2007. **99**(23): p. 236805.
72. Reinle-Schmitt, M.L., et al., *Tunable conductivity threshold at polar oxide interfaces.* Nat Commun, 2012. **3**: p. 932.
73. Segal, Y., et al., *X-ray photoemission studies of the metal-insulator transition in $LaAlO_3/SrTiO_3$ structures grown by molecular beam epitaxy.* Physical Review B, 2009. **80**(24): p. 241107.
74. Colby, R., et al., *Cation intermixing and electronic deviations at the insulating $LaCrO_3$ /$SrTiO_3$ (001) interface.* Physical Review B, 2013. **88**(15): p. 155325.
75. Willmott, P.R., et al., *Structural Basis for the Conducting Interface between $LaAlO_3$ and $SrTiO_3$.* Physical Review Letters, 2007. **99**(15): p. 155502.
76. Liu, Z.Q., et al., *Atomically flat interface between a single-terminated $LaAlO_3$ substrate and $SrTiO_3$ thin film is insulating.* AIP Advances, 2012. **2**(1): p. 012147-5.
77. Kalabukhov, A., et al., *Effect of oxygen vacancies in the $SrTiO_3$ substrate on the electrical properties of the $LaAlO_3$ ／$SrTiO_3$ interface.* Physical Review B, 2007. **75**(12): p. 121404.
78. Siemons, W., et al., *Origin of Charge Density at $LaAlO_3$ on $SrTiO_3$ Heterointerfaces: Possibility of Intrinsic Doping.* Physical Review Letters, 2007. **98**(19): p. 196802.
79. Herranz, G., et al., *High Mobility in $LaAlO_3/SrTiO_3$ Heterostructures: Origin, Dimensionality, and Perspectives.* Physical Review Letters, 2007. **98**(21): p. 216803.
80. Eckstein, J.N., *Oxide interfaces: Watch out for the lack of oxygen.* Nat Mater, 2007. **6**(7): p. 473-474.
81. Liu, Z.Q., et al., *Metal-Insulator Transition in $SrTiO_{3-x}$ Thin Films Induced by Frozen-Out Carriers.* Physical Review Letters, 2011. **107**(14): p. 146802.
82. Kim, C.H., et al., *Strontium-Doped Perovskites Rival Platinum Catalysts for Treating NO_x in Simulated Diesel Exhaust.* Science, 2010. **327**(5973): p. 1624-1627.

83. Suntivich, J., et al., *Design principles for oxygen-reduction activity on perovskite oxide catalysts for fuel cells and metal–air batteries.* Nat Chem, 2011. **3**(7): p. 546-550.
84. Gibert, M., et al., *Exchange bias in $LaNiO_3$–$LaMnO_3$ superlattices.* Nat Mater, 2012. **11**(3): p. 195-198.
85. Monkman, E.J., et al., *Quantum many-body interactions in digital oxide superlattices.* Nat Mater, 2012. **11**(10): p. 855-859.
86. Sawada, H., et al., *Jahn-Teller distortion and magnetic structures in $LaMnO_3$.* Physical Review B, 1997. **56**(19): p. 12154-12160.
87. Goodenough, J.B., *Theory of the Role of Covalence in the Perovskite-Type Manganites $LaMnO_3$.* Physical Review, 1955. **100**(2): p. 564-573.
88. Matsumoto, G., *Study of $(La_{1-x}Ca_x)MnO3$. I. Magnetic Structure of $LaMnO_3$.* Journal of the Physical Society of Japan, 1970. **29**(3): p. 606-615.
89. Coey, J.M.D., M. Viret, and S. von Molnár, *Mixed-valence manganites.* Advances in Physics, 1999. **48**(2): p. 167-293.
90. Skumryev, V., et al., *Weak ferromagnetism in LaMnO3.* The European Physical Journal B - Condensed Matter and Complex Systems, 1999. **11**(3): p. 401-406.
91. Gupta, A., et al., *Growth and giant magnetoresistance properties of La‐deficient $La_xMnO_{3-\delta}$ $(0.67 \leqslant x \leqslant 1)$ films.* Applied Physics Letters, 1995. **67**(23): p. 3494-3496.
92. Shah, A.B., et al., *Probing Interfacial Electronic Structures in Atomic Layer $LaMnO_3$ and $SrTiO_3$ Superlattices.* Advanced Materials, 2010. **22**(10): p. 1156-1160.
93. Garcia-Barriocanal, J., et al., *"Charge Leakage" at $LaMnO_3$/$SrTiO_3$ Interfaces.* Advanced Materials, 2010. **22**(5): p. 627-632.
94. Qiao, L., et al., *$LaCrO_3$ heteroepitaxy on $SrTiO_3(001)$ by molecular beam epitaxy.* Applied Physics Letters, 2011. **99**(6): p. 061904.
95. Mundy, J.A., et al., *Visualizing the interfacial evolution from charge compensation to metallic screening across the manganite metal–insulator transition.* Nat Commun, 2014. **5**.
96. Bibes, M., *Nanoferronics is a winning combination.* Nat Mater, 2012. **11**(5): p. 354-357.
97. Junquera, J. and P. Ghosez, *Critical thickness for ferroelectricity in perovskite ultrathin films.* Nature, 2003. **422**(6931): p. 506-509.
98. Ghosez, P. and K.M. Rabe, *Microscopic model of ferroelectricity in stress-free $PbTiO_3$ ultrathin films.* Applied Physics Letters, 2000. **76**(19): p. 2767-2769.
99. Sai, N., A.M. Kolpak, and A.M. Rappe, *Ferroelectricity in ultrathin perovskite films.* Physical Review B, 2005. **72**(2): p. 020101.
100. Bune, A.V., et al., *Two-dimensional ferroelectric films.* Nature, 1998. **391**(6670): p. 874-877.
101. Tenne, D.A., et al., *Probing Nanoscale Ferroelectricity by Ultraviolet Raman Spectroscopy.* Science, 2006. **313**(5793): p. 1614-1616.
102. Garcia, V. and M. Bibes, *Ferroelectric tunnel junctions for information storage and processing.* Nat Commun, 2014. **5**.
103. Tsymbal, E.Y., et al., *Ferroelectric and multiferroic tunnel junctions.* MRS Bulletin, 2012. **37**(02): p. 138-143.
104. Esaki, L., R.B. Laibowitz, and P.J. Stiles, *Polar switch* IBM Tech. Discl.Bull., 1971. **13**: p. 2161-2162.
105. Rodríguez Contreras, J., et al., *Resistive switching in metal–ferroelectric–metal junctions.* Applied Physics Letters, 2003. **83**(22): p. 4595-4597.

106. Tsymbal, E.Y. and H. Kohlstedt, *Tunneling Across a Ferroelectric.* Science, 2006. **313**(5784): p. 181-183.
107. Li, Z., et al., *An Epitaxial Ferroelectric Tunnel Junction on Silicon.* Advanced Materials, 2014. **26**(42): p. 7158-7159.
108. Chanthbouala, A., et al., *Solid-state memories based on ferroelectric tunnel junctions.* Nat Nano, 2012. **7**(2): p. 101-104.
109. Gruverman, A., et al., *Tunneling Electroresistance Effect in Ferroelectric Tunnel Junctions at the Nanoscale.* Nano Letters, 2009. **9**(10): p. 3539-3543.
110. Garcia, V., et al., *Giant tunnel electroresistance for non-destructive readout of ferroelectric states.* Nature, 2009. **460**(7251): p. 81-84.
111. Pantel, D., et al., *Reversible electrical switching of spin polarization in multiferroic tunnel junctions.* Nat Mater, 2012. **11**(4): p. 289-293.
112. Hambe, M., et al., *Crossing an Interface: Ferroelectric Control of Tunnel Currents in Magnetic Complex Oxide Heterostructures.* Advanced Functional Materials, 2010. **20**(15): p. 2436-2441.
113. Liu, Y.K., et al., *Coexistence of four resistance states and exchange bias in $La_{0.6}Sr_{0.4}MnO_3/BiFeO_3/La_{0.6}Sr_{0.4}MnO_3$ multiferroic tunnel junction.* Applied Physics Letters, 2014. **104**(4): p. 043507.
114. Gajek, M., et al., *Tunnel junctions with multiferroic barriers.* Nat Mater, 2007. **6**(4): p. 296-302.
115. Kohlstedt, H., et al., *Theoretical current-voltage characteristics of ferroelectric tunnel junctions.* Physical Review B, 2005. **72**(12): p. 125341.
116. Wen, Z., et al., *Ferroelectric-field-effect-enhanced electroresistance in metal/ferroelectric/semiconductor tunnel junctions.* Nat Mater, 2013. **12**(7): p. 617-621.
117. Yin, Y.W., et al., *Enhanced tunnelling electroresistance effect due to a ferroelectrically induced phase transition at a magnetic complex oxide interface.* Nat Mater, 2013. **12**(5): p. 397-402.
118. Koster, G., et al., *Quasi-ideal strontium titanate crystal surfaces through formation of strontium hydroxide.* Applied Physics Letters, 1998. **73**(20): p. 2920-2922.
119. Ngai, J.H., et al., *Achieving A-Site Termination on $La_{0.18}Sr_{0.82}Al_{0.59}Ta_{0.41}O_3$ Substrates.* Advanced Materials, 2010. **22**(26-27): p. 2945-2948.
120. Kleibeuker, J.E., et al., *Structure of singly terminated polar $DyScO_3$ (110) surfaces.* Physical Review B, 2012. **85**(16): p. 165413.
121. Dijkkamp, D., et al., *Preparation of Y‐Ba‐Cu oxide superconductor thin films using pulsed laser evaporation from high Tc bulk material.* Applied Physics Letters, 1987. **51**(8): p. 619-621.
122. Rosenfeld, G., B. Poelsema, and G. Comsa, *Chapter 3 Epitaxial growth modes far from equilibrium*, in *The Chemical Physics of Solid Surfaces*, D.A. King and D.P. Woodruff, Editors. 1997, Elsevier. p. 66-101.
123. Williams, D. and C.B. Carter, *Kikuchi Diffraction*, in *Transmission Electron Microscopy*. 2009, Springer US. p. 311-322.
124. Coey, J.M.D., *Magnetism and Magnetic Materials*. 2010: Cambridge University Press.
125. Shibuya, K., et al., *Metallic conductivity at the $CaHfO_3/SrTiO_3$ interface.* Applied Physics Letters, 2007. **91**(23): p. 232106-3.
126. Chen, Y., et al., *Metallic and Insulating Interfaces of Amorphous $SrTiO_3$-Based Oxide Heterostructures.* Nano Letters, 2011. **11**(9): p. 3774-3778.

127. Lee, S.W., et al., *Creation and Control of Two-Dimensional Electron Gas Using Al-Based Amorphous Oxides/$SrTiO_3$ Heterostructures Grown by Atomic Layer Deposition.* Nano Letters, 2012. **12**(9): p. 4775-4783.
128. Delahaye, J. and T. Grenet, *Metallicity of the $SrTiO_3$ surface induced by room temperature evaporation of alumina.* Journal of Physics D: Applied Physics, 2012. **45**: p. 315301.
129. Chen, Y.Z., et al., *Room Temperature Formation of High-Mobility Two-Dimensional Electron Gases at Crystalline Complex Oxide Interfaces.* Advanced Materials, 2014. **26**(9): p. 1462-1467.
130. Chen, J.Q., et al., *Defect dynamics and spectral observation of twinning in single crystalline $LaAlO_3$ under subbandgap excitation.* Applied Physics Letters, 2011. **98**(4): p. 041904-3.
131. Huijben, M., et al., *Electronically coupled complementary interfaces between perovskite band insulators.* Nat Mater, 2006. **5**(7): p. 556-560.
132. Campbell, C.T., *Ultrathin metal films and particles on oxide surfaces: structural, electronic and chemisorptive properties.* Surface Science Reports, 1997. **27**(1–3): p. 1-111.
133. Calvani, P., et al., *Observation of a midinfrared band in $SrTiO_{3-y}$.* Physical Review B, 1993. **47**(14): p. 8917-8922.
134. Na-Phattalung, S., et al., *First-principles study of native defects in anatase TiO_2.* Physical Review B, 2006. **73**(12): p. 125205.
135. Gariglio, S., et al., *Superconductivity at the $LaAlO_3/SrTiO_3$ interface.* Journal of Physics: Condensed Matter, 2009. **21**: p. 164213.
136. Huang, B.-C., et al., *Mapping Band Alignment across Complex Oxide Heterointerfaces.* Physical Review Letters, 2012. **109**(24): p. 246807.
137. Bark, C.W., et al., *Tailoring a two-dimensional electron gas at the $LaAlO_3/SrTiO_3$ (001) interface by epitaxial strain.* Proceedings of the National Academy of Sciences, 2011. **108**(12): p. 4720-4724.
138. Xie, Y., et al., *Control of electronic conduction at an oxide heterointerface using surface polar adsorbates.* Nat Commun, 2011. **2**: p. 494.
139. Au, K., et al., *Polar Liquid Molecule Induced Transport Property Modulation at $LaAlO_3/SrTiO_3$ Heterointerface.* Advanced Materials, 2012. **24**(19): p. 2598-2602.
140. Warusawithana, M.P., et al., *LaAlO3 stoichiometry is key to electron liquid formation at LaAlO3/SrTiO3 interfaces.* Nat Commun, 2013. **4**: p. 2351.
141. Breckenfeld, E., et al., *Effect of Growth Induced (Non)Stoichiometry on Interfacial Conductance in $LaAlO_3/SrTiO_3$.* Physical Review Letters, 2013. **110**(19): p. 196804.
142. Lee, J.S., et al., *Gate-controlled metal–insulator transition in the $LaAlO_3/SrTiO_3$ system with sub-critical $LaAlO_3$ thickness.* physica status solidi (RRL) – Rapid Research Letters, 2012. **6**(12): p. 472-474.
143. Stauffer, D. and A. Aharony, *Introduction To Percolation Theory*. Revised 2nd Edition ed. 2003: Taylor & Francis. 16-17.
144. Basletic, M., et al., *Mapping the spatial distribution of charge carriers in $LaAlO_3/SrTiO_3$ heterostructures.* Nat Mater, 2008. **7**(8): p. 621-625.
145. Bell, C., et al., *Thickness dependence of the mobility at the $LaAlO_3/SrTiO_3$ interface.* Applied Physics Letters, 2009. **94**(22): p. 222111.
146. Warusawithana, M.P., et al., *$LaAlO_3$ stoichiometry is key to electron liquid formation at $LaAlO_3/SrTiO_3$ interfaces.* Nat Commun, 2013. **4**.

147. Sato, H.K., et al., *Stoichiometry control of the electronic properties of the $LaAlO_3/SrTiO_3$ heterointerface.* Applied Physics Letters, 2013. **102**(25): p. 251602.
148. Breckenfeld, E., et al., *Effect of Growth Induced (Non)Stoichiometry on Interfacial Conductance in $LaAlO_3/SrTiO_3$.* Physical Review Letters, 2013. **110**(19): p. 196804.
149. Ben Shalom, M., et al., *Anisotropic magnetotransport at the $LaAlO_3/SrTiO_3$ interface.* Physical Review B, 2009. **80**(14): p. 140403.
150. Wang, X., et al., *Magnetoresistance of two-dimensional and three-dimensional electron gas in $LaAlO_3/SrTiO_3$ heterostructures: Influence of magnetic ordering, interface scattering, and dimensionality.* Physical Review B, 2011. **84**(7): p. 075312.
151. Lee, M., et al., *Electrolyte Gate-Controlled Kondo Effect in $LaAlO_3/SrTiO_3$* Physical Review Letters, 2011. **107**(25): p. 256601.
152. Zhou, K.-J., et al., *Localized and delocalized Ti 3d carriers in $LaAlO_3/SrTiO_3$ superlattices revealed by resonant inelastic x-ray scattering.* Physical Review B, 2011. **83**(20): p. 201402.
153. Sing, M., et al., *Profiling the Interface Electron Gas of $LaAlO_3/SrTiO_3$ Heterostructures with Hard X-Ray Photoelectron Spectroscopy.* Physical Review Letters, 2009. **102**(17): p. 176805.
154. Cancellieri, C., et al., *Interface Fermi States of $LaAlO_3/SrTiO_3$ and Related Heterostructures.* Physical Review Letters, 2013. **110**(13): p. 137601.
155. Lee, J.S., et al., *Titanium dxy ferromagnetism at the $LaAlO_3/SrTiO_3$ interface.* Nat Mater, 2013. **12**(8): p. 703-706.
156. Pavlenko, N., et al., *Magnetic and superconducting phases at the $LaAlO_3/SrTiO_3$ interface: The role of interfacial Ti 3d electrons.* Physical Review B, 2012. **85**(2): p. 020407.
157. Hotta, Y., T. Susaki, and H.Y. Hwang, *Polar Discontinuity Doping of the $LaVO_3/SrTiO_3$ Interface.* Physical Review Letters, 2007. **99**(23): p. 236805.
158. Perna, P., et al., *Conducting interfaces between band insulating oxides: The $LaGaO_3/SrTiO_3$ heterostructure.* Applied Physics Letters, 2010. **97**(15): p. 152111-3.
159. Liu, Z.Q., et al., *Origin of the Two-Dimensional Electron Gas at $LaAlO_3/SrTiO_3$ Interfaces: The Role of Oxygen Vacancies and Electronic Reconstruction.* Physical Review X, 2013. **3**(2): p. 021010.
160. Mathew, S., et al., *Tuning the Interface Conductivity of $LaAlO_3/SrTiO_3$ Using Ion Beams: Implications for Patterning.* ACS Nano, 2013. **7**(12): p. 10572-10581.
161. Lih J. Chen, *Silicide Technology for Integrated Circuits*. 2004: Institution of Engineering and Technology.
162. Yun-Zhong, C., et al., *High-mobility two-dimensional electron gases at oxide interfaces: Origin and opportunities.* Chinese Physics B, 2013. **22**(11): p. 116803.
163. Li, C., et al., *The metallic interface between insulating $NdGaO_3$ and $SrTiO_3$ perovskites.* Applied Physics Letters, 2013. **103**(20): p. 201602.
164. Fête, A., et al., *Growth-induced electron mobility enhancement at the $LaAlO_3/SrTiO_3$ interface.* Applied Physics Letters, 2015. **106**(5): p. 051604.
165. Li, C.J., et al., *Nature of Electron Scattering in $LaAlO_3/SrTiO_3$ Interfaces Near the Critical Thickness.* Advanced Materials Interfaces, 2015. **2**(1): p. 1400437.
166. Itkin, V.P. and C.B. Alcock, *The Si-Sr (Silicon-Strontium) system.* Bulletin of Alloy Phase Diagrams, 1989. **10**(6): p. 630-634.
167. Miura, K., et al., *Growth evolution of Sr-silicide layers on Si(111) and Mg_2Si/Si(111) substrates.* Thin Solid Films, 2006. **508**(1–2): p. 74-77.

168. McKee, R.A., F.J. Walker, and M.F. Chisholm, *Crystalline Oxides on Silicon: The First Five Monolayers.* Physical Review Letters, 1998. **81**(14): p. 3014-3017.
169. Yu, Z., et al., *Properties of Epitaxial SrTiO3 Thin Films Grown on Silicon by Molecular Beam Epitaxy.* MRS Online Proceedings Library, 1999. **567**: p. null-null.
170. Jeon, S., et al., *Electrical characteristics of epitaxially grown $SrTiO_3$ on silicon for metal-insulator-semiconductor gate dielectric applications.* Electron Device Letters, IEEE, 2003. **24**(4): p. 218-220.
171. Hu, X., et al., *The interface of epitaxial $SrTiO_3$ on silicon: in situ and ex situ studies.* Applied Physics Letters, 2003. **82**(2): p. 203-205.
172. Warusawithana, M.P., et al., *A Ferroelectric Oxide Made Directly on Silicon.* Science, 2009. **324**(5925): p. 367-370.
173. Huijben, M., et al., *Critical thickness and orbital ordering in ultrathin $La_{0.7}Sr_{0.3}MnO_3$ films.* Physical Review B, 2008. **78**(9): p. 094413.
174. Xia, J., et al., *Critical thickness for itinerant ferromagnetism in ultrathin films of $SrRuO_3$.* Physical Review B, 2009. **79**(14): p. 140407.
175. Kalisky, B., et al., *Critical thickness for ferromagnetism in $LaAlO_3/SrTiO_3$ heterostructures.* Nat Commun, 2012. **3**: p. 922.
176. Saitoh, E., et al., *Observation of orbital waves as elementary excitations in a solid.* Nature, 2001. **410**(6825): p. 180-183.
177. NA, *Application Note 1070-207: Using PPMS Superconducting Magnets at Low Field.* 2009, Quantum Design.
178. Golmar, F., et al., *Extrinsic origin of ferromagnetism in single crystalline LaAlO3 substrates and oxide films.* Applied Physics Letters, 2008. **92**(26): p. 262503.
179. Mondal, P., et al., *Dielectric anomaly at T_N in $LaMn_3$ as a signature of coupling between spin and orbital degrees of freedom.* Physical Review B, 2007. **76**(17): p. 172403.
180. Chainani, A., M. Mathew, and D.D. Sarma, *Electron spectroscopic investigation of the semiconductor-metal transition in $La_{1-x}Sr_xMnO_3$.* Physical Review B, 1993. **47**(23): p. 15397-15403.
181. Son, W.-j., et al., *Density and spatial distribution of charge carriers in the intrinsic n-type $LaAlO_3$-$SrTiO_3$ interface.* Physical Review B, 2009. **79**(24): p. 245411.
182. Fujishiro, H., T. Fukase, and M. Ikebe, *Charge Ordering and Sound Velocity Anomaly in $La_{1-X}Sr_XMnO_3$ ($x \geqslant 0.5$).* Journal of the Physical Society of Japan, 1998. **67**(8): p. 2582-2585.
183. Dagotto, E., T. Hotta, and A. Moreo, *Colossal magnetoresistant materials: the key role of phase separation.* Physics Reports, 2001. **344**(1–3): p. 1-153.
184. Burton, J.D. and E.Y. Tsymbal, *Giant Tunneling Electroresistance Effect Driven by an Electrically Controlled Spin Valve at a Complex Oxide Interface.* Physical Review Letters, 2011. **106**(15): p. 157203.
185. Zenkevich, A., et al., *Electronic band alignment and electron transport in $Cr/BaTiO_3/Pt$ ferroelectric tunnel junctions.* Applied Physics Letters, 2013. **102**(6): p. 062907.
186. Ebata, K., et al., *Chemical potential shift and spectral-weight transfer in $Pr_{1-x}Sr_xMnO_3$.* Physical Review B, 2006. **74**(6): p. 064419.
187. Fong, D.D., et al., *Ferroelectricity in Ultrathin Perovskite Films.* Science, 2004. **304**(5677): p. 1650-1653.
188. Disa, A.S., et al., *Orbital Engineering in Symmetry-Breaking Polar Heterostructures.* Physical Review Letters, 2015. **114**(2): p. 026801.